

**University of Alberta**

**Patterns and Pathways of Hydrogenation of Asphaltene Model  
Compounds**

by

**Judah Michael Ben-Jesse Mierau**

A thesis submitted to the Faculty of Graduate Studies and Research  
in partial fulfillment of the requirements for the degree of

**Master of Science in Chemical Engineering**

**Department of Chemical and Materials Engineering**

© Judah Michael Ben-Jesse Mierau

Fall 2011  
Edmonton, Alberta

Permission is hereby granted to the University of Alberta Libraries to reproduce single copies of this thesis and to lend or sell such copies for private, scholarly or scientific research purposes only. Where the thesis is converted to, or otherwise made available in digital form, the University of Alberta will advise potential users of the thesis of these terms.

The author reserves all other publication and other rights in association with the copyright in the thesis and, except as herein before provided, neither the thesis nor any substantial portion thereof may be printed or otherwise reproduced in any material form whatsoever without the author's prior written permission.

## Abstract

Large polycyclic aromatic nitrogen containing asphaltene model compounds, with molecular weights from 535 to 702 g/mol, were catalytically hydrogenated and hydrodenitrogenated in the presence of a commercial NiMo/ $\gamma$ -Al<sub>2</sub>O<sub>3</sub> catalyst in a stainless steel batch reactor at 370 °C and 17.9 MPa total pressure for 1 h. The patterns and pathways of hydrogenation of two families of model compounds were investigated: alkyl-bridged pyrenes linked to a pyridine centre ring and substituted cholestane – benzoquinoline compounds. Analysis of reaction products by matrix assisted laser desorption ionization – mass spectrometry, high performance liquid chromatography, and gas chromatography demonstrated that for the pyrene/pyridine family there was a strong preference for hydrogenation of the bridged pyrene groups compared to the centre pyridinic ring. For the cholestane family, no cracking or hydrodenitrogenation reactions occurred. Results imply that hydrotreatment of similar large nitrogen asphaltene compounds are dominated by reactions other than hydrodenitrogenation.

## **Acknowledgements**

I would like to thank first and foremost Dr. Murray Gray for his support, patience and guidance he has shown me throughout this endeavour.

This project could not have occurred without the extensive help of both Kavithaa Logan and Tuyet Le. Kavithaa graciously trained me on most analytical instruments used in this study, for which I am grateful. Tuyet Le helped me troubleshoot and problem-solve many roadblocks in the experimental procedure.

I am grateful for the Integrated Nanosystems Research Facility, especially Nancy Zhang, for patiently training me how to use the MALDI – MS instrument. Her instruction on use of the instrument and how to interpret data was invaluable.

Lastly, I'd like to thank the Centre for Oilsands Innovation (COSI) at the University of Alberta for their support and use of equipment and facilities.

# Table of Contents

<b>CHAPTER 1: INTRODUCTION AND LITERATURE REVIEW</b>	<b>1</b>
<b>1.1 Introduction</b>	<b>1</b>
<b>1.2 Literature Review</b>	<b>2</b>
1.2.1 Composition and Structure of Vacuum Residua and Asphaltenes	2
1.2.2 Nitrogen Compounds in Petroleum	4
1.2.3 Hydrodenitrogenation	8
1.2.3.1 The Basic Mechanism of HDN	8
1.2.3.2 Pathways of HDN of Pyridine	9
1.2.3.3 Pathways, Mechanisms and Reactivity of HDN of Large Polycyclic Aromatic Nitrogen Compounds	11
1.2.3.3.1 Acridine	11
1.2.3.3.2 5,6- and 7,8-Benzoquinoline	14
1.2.3.3.3 Carbazole	18
1.2.3.4 Inhibition of HDN from the Presence of Other Compounds	20
1.2.3.5 The Effects of H <sub>2</sub> and H <sub>2</sub> S Partial Pressures on HDN	22
1.2.3.6 Catalysts for Hydrodenitrogenation	23
1.2.4 Process Technologies for Hydroconversion and Hydrotreatment	25
1.2.4.1 Hydroconversion	25
1.2.4.1.1 Fixed Bed	25
1.2.4.1.2 Catalytic Ebullated Bed	27
1.2.4.1.3 Slurry or Additive Based Processes	28
1.2.4.2 Hydrotreatment	29
1.2.5 Knowledge Gaps	31
<b>1.3 Objectives</b>	<b>32</b>
<b>1.4 References</b>	<b>33</b>
<b>CHAPTER 2: EXPERIMENTAL MATERIALS AND METHODS</b>	<b>40</b>
<b>2.1 Chemicals</b>	<b>40</b>
2.1.1 Model Compounds	40
2.1.2 Catalyst	41

<b>2.2</b>	<b>Experimental Equipment</b>	<b>44</b>
2.2.1	Micro Batch Reactor	44
2.2.2	Sand Bath	46
2.2.3	Glove Box	47
2.2.4	High Performance Liquid Chromatograph	48
2.2.5	Gas Chromatograph	50
2.2.6	Matrix-Assisted Laser Desorption Ionization – Mass Spectrometer	51
2.2.7	Fourier Transform Infrared Spectrometer	52
<b>2.3</b>	<b>Experimental Procedure</b>	<b>52</b>
2.3.1	Reactor Feed	52
2.3.2	Catalyst Presulfidation	53
2.3.3	Reactor Loading	54
2.3.4	Reactor Sealing and Hydrogen Pressurization	54
2.3.5	Reaction	56
2.3.6	Product Recovery	57
2.3.7	Sample Analysis	58
2.3.7.1	HPLC Analysis	59
2.3.7.2	GC Analysis	60
2.3.7.3	MALDI – MS Analysis	61
<b>2.4</b>	<b>References</b>	<b>63</b>
	<b>CHAPTER 3: RESULTS</b>	<b>64</b>
<b>3.1</b>	<b>Validation of Experimental Method</b>	<b>64</b>
3.1.1	Reactor Heat-up Curve	64
3.1.2	Repeatability of Results	66
3.1.2.1	Repeatability of HPLC Analysis	66
3.1.2.2	Repeatability of GC Analysis	68
3.1.2.3	Repeatability of MALDI – MS Analysis	69
3.1.3	Validation of Catalytic Activity	71
3.1.3.1	Catalytic Conversion of Control Compounds	71
3.1.3.2	Catalytic Activity without Hydrogen and without Catalyst	74
3.1.3.3	Thermal Cracking of Model Compound P-3,5-pyridine-P	75
<b>3.2</b>	<b>Model Compound Activity and Pathway Yields</b>	<b>80</b>
3.2.1	Steady State Activity in Sequential Batch Catalytic Reactions	80

3.2.2	Yield of Cracked Products	87
3.2.3	Yield of Hydrodenitrogenation and Hydrogenation Products	88
3.2.3.1	Verification and Categorization of Hydrodenitrogenation and Hydrogenation Products by MALDI – MS/MS	88
3.2.3.2	Selectivity Ratio of HDN and Hydrogenation Products by Modified Integrated Peak Area Spectra	91
3.2.3.3	Irreversible Adsorption of Nitrogen Compounds onto Catalyst Surface	97
<b>3.3</b>	<b>References</b>	<b>100</b>
 <b>CHAPTER 4: DISCUSSION AND CONCLUSIONS</b>		<b>101</b>
<b>4.1</b>	<b>Pyrene/Pyridine Family of Model Compounds</b>	<b>101</b>
<b>4.2</b>	<b>Cholestane Family of Model Compounds</b>	<b>108</b>
<b>4.3</b>	<b>Implications</b>	<b>110</b>
<b>4.4</b>	<b>Conclusions</b>	<b>111</b>
<b>4.5</b>	<b>References</b>	<b>113</b>
 <b>APPENDIX A: HPLC CHROMATOGRAMS AND CALCULATIONS</b>		<b>114</b>
<b>1</b>	<b>Calculations by Calibration Curve</b>	<b>114</b>
<b>2</b>	<b>HPLC Chromatograms</b>	<b>118</b>
 <b>APPENDIX B: GC CHROMATOGRAMS AND CALCULATIONS</b>		<b>126</b>
<b>1</b>	<b>Single Point Internal Standard Method Calculations</b>	<b>126</b>
<b>2</b>	<b>GC Chromatograms</b>	<b>129</b>
 <b>APPENDIX C: MALDI – MS ANALYSIS METHOD AND SPECTRA</b>		<b>137</b>
<b>1</b>	<b>MALDI – MS Analysis Method</b>	<b>137</b>
<b>Step 1</b>	<b>Possible Product Peak Identification</b>	<b>138</b>

<b>Step 2</b>	<b>Product Peak Verification by MALDI – MS/MS</b>	<b>138</b>
<b>Step 3</b>	<b>Isotope Identification</b>	<b>140</b>
<b>Step 4</b>	<b>Product Peak Area Integration and Summation</b>	<b>141</b>
<b>2</b>	<b>MALDI – MS Spectra</b>	<b>144</b>

## List of Tables

Table 1-1 Compound classes from the flash pyrolysis of C <sub>5</sub> Athabasca asphaltenes at 430 °C (Payzant et al., 1991; Strausz and Lown, 2003).....	4
Table 1-2 Distribution of nitrogen compounds (mol %) in three middle distillates (Mushrush et al., 1999).....	7
Table 1-3 Elemental composition and surface area of hydrodenitrogenation catalysts used in various studies.....	24
Table 1-4 Operating parameters for a typical fixed-bed process (Topsøe et al., 1996) .....	27
Table 1-5 Operating parameters for a typical catalytic ebullated bed process (Topsøe et al., 1996) .....	28
Table 1-6 List of various slurry hydroconversion processes .....	29
Table 1-7 Operating parameters for hydrotreating different feedstocks (Heinrich and Kasztelan, 2001).....	31
Table 2-1 List of the chemicals used .....	42
Table 2-2 List of model compounds investigated .....	43
Table 2-3 Mobile phase composition and flow profile for each sample analyzed .....	49
Table 2-4 The mobile phase flow rate controller program .....	49
Table 2-5 Instrument method by detector used for GC operation.....	51
Table 2-6 Experimental conditions and reaction times .....	57
Table 3-1 GC analysis of a series of replicate samples at identical concentration .....	69
Table 3-2 Conversion of quinoline at mild and normal conditions.....	72
Table 3-3 Conversion of phenanthrene at mild and normal conditions.....	73
Table 3-4 Pyrene conversion and apparent first order rate constant at normal conditions.....	74
Table 3-5 Conversions obtained in experiments without hydrogen and without catalyst .....	75
Table 3-6 The yield of cracked products after catalytic and thermal reactions of P-3,5-pyridine-P .....	76
Table 3-7 Reaction rate constant estimates and error of estimates .....	83
Table 3-8 Pathway conversions, yields and apparent reaction rate constant for asphaltene model compounds .....	86
Table 4-1 Comparison of overall reactivity by all pathways, the yield of HDN products (%) and heteroatomic centre ring basicity for the pyrene/pyridine family .....	106
Table A-2 Calibration curve linear regression equations and error .....	115
Table A-3 Calibration curve data for P-3-methyl-2,5-pyridine-P.....	116
Table B-1 List of data required for single point internal standard method calculations .....	128
Table C-2 List of integrated peak areas for identified reaction products for the pyrene/pyridine family.....	142

Table C-3 List of integrated peak areas for identified reaction products for the cholestane family  
..... 143

## List of Figures

<b>Figure 1-1</b> Representation of the molecular structure of an Athabasca asphaltene, reduced molecular weight MW = 2497 g/mol (Sheremata et al., 2004) .....	5
<b>Figure 1-2</b> Typical basic and non-basic nitrogen compounds found in gas oils (Shin et al., 2000) .....	6
<b>Figure 1-3</b> Schematic of the reaction network of the HDN of pyridine (Prins, 2001) .....	10
<b>Figure 1-4</b> Reaction network of the HDN of acridine (Nagai et al., 1986) .....	12
<b>Figure 1-5</b> Schematic of the HDN reaction network of acridine (Zawadski et al., 1982; Girgis and Gates, 1991). The numbers represent the pseudo-first-order rate constants in (g carrier oil)/(g <sub>cat</sub> ·s) at 367 °C, 13.7 MPa, and 0.5 wt % acridine in the feed. ....	13
<b>Figure 1-6</b> Schematic of the reaction network of HDN for 5,6-benzoquinoline with pseudo-first-order reaction rate constants in L/(g <sub>cat</sub> ·s) at 300 °C (Shabtai et al., 1989) .....	15
<b>Figure 1-7</b> Schematic of the reaction network of HDN for 7,8-benzoquinoline with the relative values of the pseudo-first-order reaction rate constants at 340 °C proposed by Moreau et al. (1988).....	18
<b>Figure 1-8</b> Schematic of the reaction network of the HDN of carbazole (Nagai et al., 1988).....	20
<b>Figure 1-9</b> Schematic diagram of a conventional fixed-bed residue hydroprocessing unit (Anon, 1998).....	26
<b>Figure 1-10</b> Schematic of a diesel hydrotreating unit (Mohamed et al., 2010).....	30
<b>Figure 2-1</b> Schematic of the micro batch reactor .....	45
<b>Figure 2-2</b> Image of the sand bath with supporting equipment.....	47
<b>Figure 2-3</b> Schematic of the hydrogen cylinder valve set-up.....	56
<b>Figure 3-1</b> Heat-up curve of a microreactor immersed in a sand bath at a set point of 350 °C ....	65
<b>Figure 3-2</b> HPLC calibration curve of model compound P-3-methyl-2,5-pyridine-P.....	67
<b>Figure 3-3</b> Repeatability of MALDI measurements as a function of cumulative reaction time for model compounds cholestane-phenyl and P-2,6-pyridine-P with standard error bars ( $n \geq 4$ ) .....	70
<b>Figure 3-4</b> HPLC chromatogram of P-3,5-pyridine-P products from catalytic reaction. Benzo[a]pyrene was added as an internal standard.....	78
<b>Figure 3-5</b> HPLC chromatogram of P-3,5-pyridine-P products from thermal cracking reaction. Benzo[a]pyrene was added as an internal standard. ....	78
<b>Figure 3-6</b> MALDI spectrum of the catalytic hydrogenation reaction products from model compound P-3,5-pyridine-P.....	79
<b>Figure 3-7</b> MALDI spectrum of reaction products from thermal cracking reaction of model compound P-3,5-pyridine-P.....	79
<b>Figure 3-8</b> Reaction rate constant of P-3-methyl-2,5-pyridine-P versus cumulative reaction time. The dashed line shows the pseudo-state rate constant.....	82

<b>Figure 3-9</b> Reaction rate constant of cholestane-phenyl versus cumulative reaction time. The dashed line shows the pseudo-state rate constant. ....	82
<b>Figure 3-10</b> Reaction rate constant of pyrene versus cumulative reaction time. The dashed line shows the pseudo-state rate constant. ....	83
<b>Figure 3-11</b> Reaction rate plot of P-2,6-pyridine-P versus cumulative reaction time .....	84
<b>Figure 3-12</b> MALDI-MS/MS spectrum of P-3-methyl-2,5-pyridine-P hydrogenation product peak $m/z = 554.28$ .....	90
<b>Figure 3-13</b> MALDI-MS/MS spectrum of P-2,6-pyridine-P hydrogenation product peak $m/z = 538.19$ .....	90
<b>Figure 3-14</b> MALDI-MS/MS spectrum of P-3,5-pyridine-P hydrogenation product peak $m/z = 544.22$ .....	91
<b>Figure 3-15</b> Modified integrated peak area spectrum of cholestane-phenyl- <i>n</i> -butyl .....	93
<b>Figure 3-16</b> Modified integrated peak area spectra of cholestane-phenyl .....	94
<b>Figure 3-17</b> Modified integrated peak area spectra of cholestane-bibenzyl .....	95
<b>Figure 3-18</b> Modified integrated peak area spectra of P-3,5-pyridine-P .....	95
<b>Figure 3-19</b> Modified integrated peak area spectra of P-3-methyl-2,5-pyridine-P .....	96
<b>Figure 3-20</b> Modified integrated peak area spectra of P-2,6-pyridine-P .....	96
<b>Figure 3-21</b> IR spectrum of cholestane-phenyl reaction product in tetralin solvent. The reference line indicates the wave number for amine vibration. ....	99
<b>Figure 3-22</b> IR spectrum of 1,2,3,4-tetrahydroquinoline in tetralin solvent. The reference line indicates the wave number for amine vibration. ....	99
<b>Figure 4-1</b> Schematic of the main products from each of the detected pathways of the catalytic reaction of pyrene-3,5-pyridine-pyrene, with the corresponding selectivity on a mass basis .....	102
<b>Figure 4-2</b> Schematic of the main products from each of the detected pathways of the catalytic reaction of pyrene-2,6-pyridine-pyrene, with the corresponding selectivity on a mass basis .....	103
<b>Figure 4-3</b> Schematic of the main products from each of the detected pathways of the catalytic reaction of pyrene-3-methyl-2,5-pyridine-pyrene, with the corresponding selectivity on a mass basis .....	104
<b>Figure 4-4</b> Schematic of the main product from the reaction pathway detected from of the catalytic reaction of the cholestane family of model compounds. In descending order: cholestane-phenyl, cholestane-bibenzyl and cholestane-phenyl- <i>n</i> -butyl. ....	109
<b>Figure A-1</b> HPLC calibration curve of P-3-methyl-2,5-pyridine-P .....	117
<b>Figure A-2</b> HPLC calibration curve of cholestane-phenyl .....	117
<b>Figure A-3</b> HPLC calibration curve of P-3,5-pyridine-P .....	118

<b>Figure A-4</b> Chromatogram of 2.40 mg/mL of P-3-methyl-2,5-pyridine-P in a feed mixture with 5.13 mg/mL of benzo[ <i>a</i> ]pyrene, undiluted .....	118
<b>Figure A-5</b> Chromatogram of P-3-methyl-2,5-pyridine-P 1 <sup>st</sup> product mixture with 3.45 mg/mL of benzo[ <i>a</i> ]pyrene, undiluted .....	119
<b>Figure A-6</b> Chromatogram of P-3-methyl-2,5-pyridine-P 2 <sup>nd</sup> product mixture with 1.40 mg/mL of benzo[ <i>a</i> ]pyrene, undiluted .....	119
<b>Figure A-7</b> Chromatogram of P-3-methyl-2,5-pyridine-P 3 <sup>rd</sup> product mixture with 2.23 mg/mL of benzo[ <i>a</i> ]pyrene, undiluted .....	119
<b>Figure A-8</b> Chromatogram of 2.39 mg/mL of P-2,6-pyridine-P in a feed mixture with 4.60 mg/mL of benzo[ <i>a</i> ]pyrene, undiluted.....	119
<b>Figure A-9</b> Chromatogram of P-2,6-pyridine-P 1 <sup>st</sup> product mixture with 1.63 mg/mL of benzo[ <i>a</i> ]pyrene, undiluted .....	120
<b>Figure A-10</b> Chromatogram of P-2,6-pyridine-P 2 <sup>nd</sup> product mixture with 4.31 mg/mL of benzo[ <i>a</i> ]pyrene, undiluted .....	120
<b>Figure A-11</b> Chromatogram of P-2,6-pyridine-P 3 <sup>rd</sup> product mixture with 2.66 mg/mL of benzo[ <i>a</i> ]pyrene, undiluted .....	120
<b>Figure A-12</b> Chromatogram of P-2,6-pyridine-P 4 <sup>th</sup> product mixture with 2.43 mg/mL of benzo[ <i>a</i> ]pyrene, undiluted .....	120
<b>Figure A-13</b> Chromatogram of 2.40 mg/mL of P-3,5-pyridine-P in a feed mixture with 1.10 mg/mL of benzo[ <i>a</i> ]pyrene, diluted 1:30 in methylene chloride .....	121
<b>Figure A-14</b> Chromatogram of P-3,5-pyridine-P 1 <sup>st</sup> product mixture with 1.16 mg/mL of benzo[ <i>a</i> ]pyrene, diluted 1:30 in methylene chloride.....	121
<b>Figure A-15</b> Chromatogram of 2.53 mg/mL of cholestane-phenyl- <i>n</i> -butyl in a feed mixture with 4.26 mg/mL of benzo[ <i>a</i> ]pyrene, undiluted .....	121
<b>Figure A-16</b> Chromatogram of cholestane-phenyl- <i>n</i> -butyl 1 <sup>st</sup> product mixture with 1.80 mg/mL of benzo[ <i>a</i> ]pyrene, undiluted .....	122
<b>Figure A-17</b> Chromatogram of cholestane-phenyl- <i>n</i> -butyl 2 <sup>nd</sup> product mixture, undiluted .....	122
<b>Figure A-18</b> Chromatogram of cholestane-phenyl- <i>n</i> -butyl 3 <sup>rd</sup> product mixture, undiluted .....	122
<b>Figure A-19</b> Chromatogram of 2.40 mg/mL of cholestane-phenyl in a feed mixture with 2.40 mg/mL of benzo[ <i>a</i> ]pyrene, diluted 1:30 in methylene chloride .....	123
<b>Figure A-20</b> Chromatogram of cholestane-phenyl 1 <sup>st</sup> reaction product with 0.80 mg/mL of benzo[ <i>a</i> ]pyrene (not shown), diluted 1:30 in methylene chloride .....	123
<b>Figure A-21</b> Chromatogram of cholestane-phenyl 2 <sup>nd</sup> reaction product with 1.00 mg/mL of benzo[ <i>a</i> ]pyrene, diluted 1:30 in methylene chloride.....	124
<b>Figure A-22</b> Chromatogram of cholestane-phenyl 3 <sup>rd</sup> reaction product with 1.43 mg/mL of benzo[ <i>a</i> ]pyrene, diluted 1:30 in methylene chloride.....	124

<b>Figure A-23</b> Chromatogram of 2.42 mg/mL of cholestane-bibenzyl in a feed mixture with 4.85 mg/mL of benzo[ <i>a</i> ]pyrene, undiluted.....	125
<b>Figure A-24</b> Chromatogram of cholestane-bibenzyl 1 <sup>st</sup> reaction product with 0.58 mg/mL of benzo[ <i>a</i> ]pyrene, undiluted .....	125
<b>Figure A-25</b> Chromatogram of cholestane-bibenzyl 2 <sup>nd</sup> reaction product, undiluted .....	125
<b>Figure A-26</b> Chromatogram of cholestane-bibenzyl 3 <sup>rd</sup> reaction product, undiluted.....	125
<b>Figure B-1</b> Chromatogram of 1 wt % phenanthrene feed (14.09 min) with 0.64 mg of 2,4,5,6-tetrachloro- <i>m</i> -xylene (12.54 min) .....	129
<b>Figure B-2</b> Chromatogram of 1 wt % phenanthrene reaction product at normal conditions with 0.30 mg of 2,4,5,6-tetrachloro- <i>m</i> -xylene .....	130
<b>Figure B-3</b> Chromatogram of 1 wt % phenanthrene reaction product at mild conditions with 0.79 mg of 2,4,5,6-tetrachloro- <i>m</i> -xylene.....	130
<b>Figure B-4</b> Chromatogram of w/o catalyst experiment reaction product at mild conditions with 0.70 mg of 2,4,5,6-tetrachloro- <i>m</i> -xylene, 1 wt % phenanthrene feed.....	131
<b>Figure B-5</b> Chromatogram of 1 wt % quinoline feed (8.00 min) with 0.37 mg of 2,4,5,6-tetrachloro- <i>m</i> -xylene (12.50 min) .....	131
<b>Figure B-6</b> Chromatogram of 1 wt % quinoline reaction product at mild conditions with 0.27 mg of 2,4,5,6-tetrachloro- <i>m</i> -xylene .....	132
<b>Figure B-7</b> Chromatogram of 1 wt % quinoline reaction product at normal conditions with 0.87 mg of 2,4,5,6-tetrachloro- <i>m</i> -xylene.....	132
<b>Figure B-8</b> Chromatogram of w/o hydrogen experiment reaction product at mild conditions with 1.06 mg of 2,4,5,6-tetrachloro- <i>m</i> -xylene, 1 wt % quinoline feed .....	133
<b>Figure B-9</b> Chromatogram of 2.58 mg/mL of pyrene (17.12 min) feed with 0.74 mg of 2,4,5,6-tetrachloro- <i>m</i> -xylene (12.54 min) .....	133
<b>Figure B-10</b> Chromatogram of 1 <sup>st</sup> pyrene reaction product with 0.89 mg of 2,4,5,6-tetrachloro- <i>m</i> -xylene.....	134
<b>Figure B-11</b> Chromatogram of 2 <sup>nd</sup> pyrene reaction product with 1.22 mg of 2,4,5,6-tetrachloro- <i>m</i> -xylene.....	134
<b>Figure B-12</b> Chromatogram of 3 <sup>rd</sup> pyrene reaction product with 0.58 mg of 2,4,5,6-tetrachloro- <i>m</i> -xylene.....	135
<b>Figure B-13</b> Chromatogram of P-3-methyl-2,5-pyridine-P reaction product with 0.80 mg of 2,4,5,6-tetrachloro- <i>m</i> -xylene.....	135
<b>Figure B-14</b> Chromatogram of P-2,6-pyridine-P reaction product with 0.34 mg of 2,4,5,6-tetrachloro- <i>m</i> -xylene.....	136
<b>Figure B-15</b> Chromatogram of P-3,5-pyridine-P reaction product with 0.43 mg of 2,4,5,6-tetrachloro- <i>m</i> -xylene.....	136
<b>Figure C-1</b> MALDI – MS feed spectrum overlaid the product spectra of P-3,5-pyridine-P.....	138

<b>Figure C-2</b> MALDI – MS/MS spectrum of parent compound P-2,6-pyridine-P .....	139
<b>Figure C-3</b> MALDI – MS/MS spectrum of precursor ion $m/z = 540.22$ , P-2,6-pyridine-P hydrogenation product .....	140
<b>Figure C-4</b> MALDI – MS spectrum of P-2,6-pyridine-P feed .....	144
<b>Figure C-5</b> MALDI – MS spectrum of P-2,6-pyridine-P reaction product .....	144
<b>Figure C-6</b> MALDI – MS spectrum of P-3,5-pyridine-P feed .....	145
<b>Figure C-7</b> MALDI – MS spectrum of P-3,5-pyridine-P reaction product .....	145
<b>Figure C-8</b> MALDI – MS spectrum of P-3-mehtyl-2,5-pyridine-P feed .....	146
<b>Figure C-9</b> MALDI – MS spectrum of P-3-mehtyl-2,5-pyridine-P reaction product .....	146
<b>Figure C-10</b> MALDI – MS spectrum of cholestane-phenyl feed .....	147
<b>Figure C-11</b> MALDI – MS spectrum of cholestane-phenyl reaction product .....	147
<b>Figure C-12</b> MALDI – MS spectrum of cholestane-phenyl- <i>n</i> -butyl feed .....	148
<b>Figure C-13</b> MALDI – MS spectrum of cholestane-phenyl- <i>n</i> -butyl reaction product .....	148
<b>Figure C-14</b> MALDI – MS spectrum of cholestane-bibenzyl feed .....	149
<b>Figure C-15</b> MALDI – MS spectrum of cholestane-bibenzyl reaction product .....	149

## Nomenclature

$A_a$	Analyte peak area
$A_{is}$	Internal standard peak area
$b$	Relative response factor
$C$	Concentration of feed (g/L)
$c_a$	Analyte concentration (mg/mL)
$c_{is}$	Internal standard concentration (mg/mL)
$k$	Reaction rate constants (L/(g <sub>cat</sub> · s))
$t$	Time (s)
$w_{cat}$	Catalyst to solvent ratio (g <sub>cat</sub> /L)
$X$	Conversion

# CHAPTER 1

---

## Introduction and Literature Review

### **1.1 Introduction**

The hydrogenation and hydrodenitrogenation of petroleum are significant chemical reactions occurring in modern industrial hydrotreating processes. Understanding of the chemistry and pathways of the reactions of nitrogen compounds in petroleum has been limited to relatively small, i.e. three carbon rings or less, molecular species such as quinoline and acridine (Girgis and Gates, 1991; Furimsky and Massoth, 2005). If further development and innovation in novel hydrotreating catalysts and processes is to continue, investigation is

required into the catalytic hydrogenation of nitrogen compounds in the heavier components of petroleum, especially the asphaltene fraction which is more resistant to nitrogen removal. Therefore, in this work, well-characterized synthetic nitrogen containing model compounds representative of asphaltene molecular structures, were catalytically hydrogenated over a commercial NiMo/ $\gamma$ -Al<sub>2</sub>O<sub>3</sub> catalyst under industrial hydrotreating conditions, i.e. 370 °C and 18 MPa of hydrogen for 1 h, in a stainless steel batch reactor. The objective of this study was to determine the patterns and pathways of hydrogenation of these asphaltene model compounds. This work is the first to explore the chemistry of large nitrogen compounds with molecular structures resembling hydrodenitrogenation – resistant asphaltene compounds, typical of heavier hydroprocessing feeds.

## **1.2 Literature Review**

Understanding of the chemistry and molecular behaviour of the heavier components of oil sands derived bitumen is a crucial step in overcoming the environmental and processing challenges facing the Canadian oil sands. In particular, the asphaltene fraction has been identified as a significant source of difficulty in recovery, refining, and upgrading of oil sands crudes. This challenge presented by the asphaltene fraction is due to its high heteroatom content, its lower stability and propensity to flocculate in product streams, and the large hydrogen requirement in hydroprocessing. Modelling the molecular behaviour of asphaltenes and similar compounds found in heavy vacuum residua would allow for further innovation and development of novel upgrading catalysts and technologies.

### **1.2.1 Composition and Structure of Vacuum Residua and Asphaltenes**

Petroleum crude oils are complex mixtures of more than tens of thousands of compounds (Hughey et al., 2002). Vacuum residua are the heaviest fractions of whole crude, and are typically defined as the high boiling fraction above 524 °C.

This fraction is differentiated from the rest of the crude oil by high concentrations of heteroatoms, i.e. S, O, N, V and Ni, lower hydrogen content, and larger component molecules ranging from 400 to >2000 Da. Vacuum residua can be further classified into maltenes and asphaltenes. Asphaltenes comprise all the material that is soluble in toluene and insoluble in an *n*-alkane, usually *n*-pentane or *n*-heptane; whereas, maltenes are the fraction soluble in the *n*-alkane. The asphaltene fraction is characterized by further enrichment of heteroatom content, the greatest hydrogen deficiency, high aromaticity and a high density of approximately 1200 kg/m<sup>3</sup> (Akbarzadeh et al., 2005). Qian et al. (2007) using field-desorption mass spectrometry suggested a mean molecular weight of 1238 Da. However, there is disagreement on what the average molecular weight of asphaltenes is. This disagreement is because evaluation of the average molecular weight of asphaltenes is hindered by aggregation of asphaltenes, which leads to severe bias in conventional methods such as vapour pressure osometry (Gray et al., 2011). Studies by Strausz et al. (1991; 2003) attempted to determine the main chemical structures present in the asphaltene fraction by both: flash pyrolysis to fragment the large component molecules with little reaction and rearrangement, and oxidation by ruthenium tetroxide to evaluate the nature of the *n*-alkane groups. Table 1-1 lists the yield for each compound class from flash pyrolysis of C<sub>5</sub> asphaltenes at 430 °C. From these data, asphaltenes and resins can be described as a copolymer of pendant groups from the compound classes in Table 1-1 connected by isoparaffin, sulfide, ester and ether bridges.

A representation of an asphaltene molecule hypothesized by the archipelago model of Sheremata et al. (2004) is illustrated in Figure 1-1, which emphasized linked molecular building blocks. An alternative continental model where 5 to 6 fused aromatic and saturated rings are decorated with alkyl side chains has been posited by Mullins et al. (2000), but has been challenged by a recently submitted paper by Gray et al. (2011) as inconsistent with observed behaviour and empirical data.

**Table 1-1** Compound classes from the flash pyrolysis of C<sub>5</sub> Athabasca asphaltenes at 430 °C (Payzant et al., 1991; Strausz and Lown, 2003)

<b>Class Fraction</b>	<b>Weight % of Initial Asphaltene</b>
<i>n</i> -alkanes	6.1
sulfides	0.7
thiophenes and thiophene benzologs	7.9
alkyl aromatics and alkyl naphthenes	8.5
Heteroaromatics	10.0
Other compounds	0.8
<b>Subtotal</b>	<b>34.0</b>
Coke	53.0
Light ends (by difference)	13.0

### 1.2.2 Nitrogen Compounds in Petroleum

Nitrogen is present in petroleum in numerous chemical species and differs greatly among each fraction and feedstock analyzed. Non-heterocyclic nitrogen, such as amines and nitriles, react readily during hydrotreatment and therefore are not an issue for nitrogen removal (Girgis and Gates, 1991). On the other hand, heterocyclic nitrogen compounds tend to have more difficulty undergoing nitrogen removal and are thus of greater interest. Heterocyclic nitrogen compounds are those compounds that contain a nitrogen heteroatom within a hydrocarbon ring structure, whether saturated or aromatic. These heterocyclic nitrogen compounds can be further classified into basic and non-basic nitrogen compounds, in the form of five- and six-membered rings, respectively (Furimsky and Massoth, 2005). Bej et al. (2001) observed that the conversion of non-basic nitrogen compounds were lower than basic nitrogen compounds, which suggests that nonbasic nitrogen compounds were more resistant to nitrogen removal. Shin et al. (2000) determined the typical nitrogen-ring structures found in hydrotreated gas oils and these are illustrated in Figure 1-2.

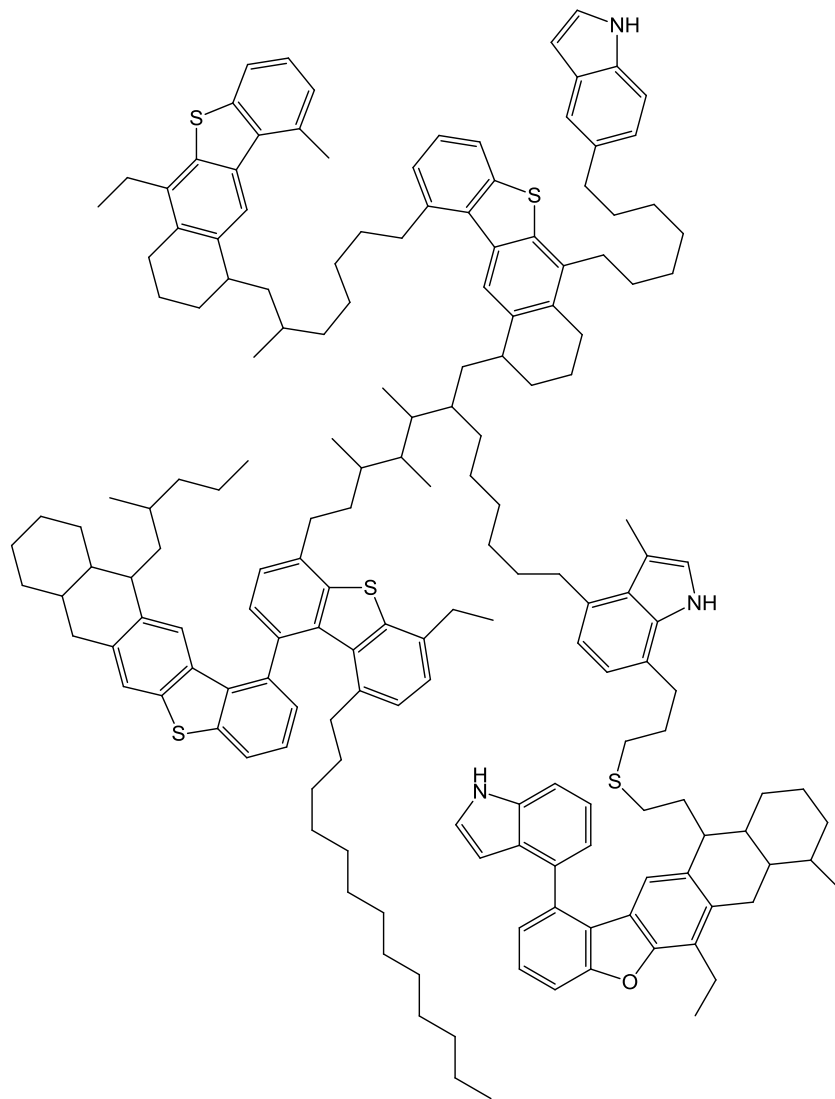
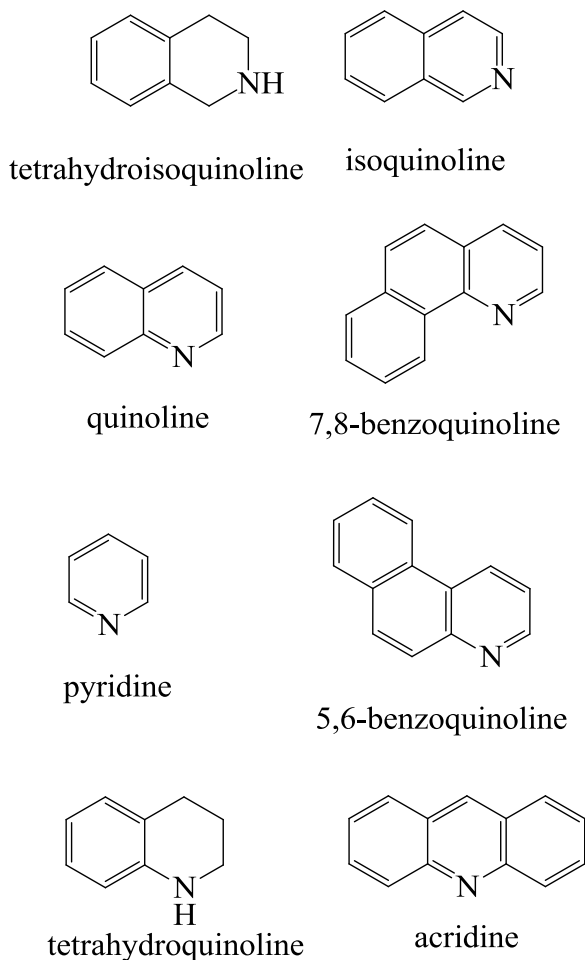


**Figure 1-1** Representation of the molecular structure of an Athabasca asphaltene, reduced molecular weight MW = 2497 g/mol (Sheremata et al., 2004)

The diversity and distribution of nitrogen compounds of various petroleum fractions is exemplified by Mushrush et al. (1999). They published the nitrogen compound distributions of three hydrotreated middle distillate fractions and are presented Table 1-2. The oil sands fraction sample contained the largest percentage of indoles and carbazoles. All three distillate fractions were found to have little unsubstituted pyridine, pyrrole, quinoline, tetrahydroquinoline, indole, and carbazole, indicating that alkyl-substituted derivatives of these species are

### Basic



### Non-Basic

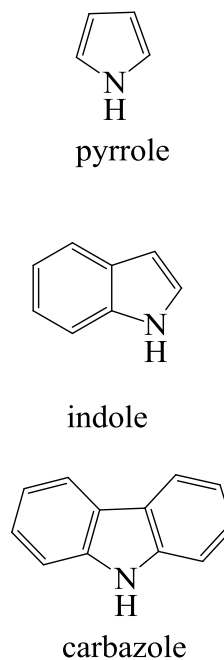


**Figure 1-2** Typical basic and non-basic nitrogen compounds found in gas oils (Shin et al., 2000)

resistant to nitrogen removal (Furimsky and Massoth, 2005). McKay et al. (1976) studied the nitrogen bases of high-boiling distillates which were characterized by a chromatographic-infrared method. The authors titrated a base fraction from the original distillate and then separated the base fraction into six analyzable subfractions. It was found that the nitrogen base fractions of four distillates approximately consisted of: 50 wt % pyridine benzologs, 25 wt % amides, and diaza compounds, and less than 5 wt % carbazoles. Where the remainder material

was distributed among the categories depended on the distillate analyzed. The pyridine benzologs structures identified in the subfractions consisted of pyridine with up to six substituent saturated or aromatic hydrocarbon rings (McKay et al., 1976).

**Table 1-2** Distribution of nitrogen compounds (mol %) in three middle distillates (Mushrush et al., 1999)

	<b>Shale</b>	<b>Petroleum</b>	<b>Oil sands</b>
Total Nitrogen (ppm)	2290	83	3050
Boiling range (°C)	150-390	220-384	190-390
Carbazoles	1.3	0.5	3.2
Indoles	3.7	18.1	39.2
Pyridines	73.5	64.3	13.3
Pyrroles	3.6	0.2	15.9
Quinolines	4.3	10.4	1.2
Tetrahydroquinolines	9.9	3.2	16.7

In two studies by Jokuty and Gray (1991; 1992) a retention chromatographic method was used to separate non-basic and basic nitrogen compounds into two fractions from a hydrotreated synthetic crude oil derived from Athabasca bitumen. The basic fraction was observed to be composed of alkylated: pyridines, quinolines, hydroquinolines, and hydrobenzoquinolines, whereas, the non-basic fraction was dominated by a series of alkyl-carbazoles with substituents ranging from 1 – 15 aliphatic carbon chains. Larger ring structures were also identified. Likewise, Dorbon et al. (1984) found a large abundance of alkyl-substituted carbazoles in coker gas oil. A similar investigation by Shin et al. (2000) agrees with the observations of the three previous studies. In this study, basic and nonbasic nitrogen compounds of hydrotreated gas oils were separated by acid extraction. The basic fraction was reported to consist of

quinolines, benzoquinolines and their derivatives; while, the nitrogen compounds observed in the non-basic fraction included mostly carbazole and its derivatives.

The information presented demonstrates a wide distribution of nitrogen compounds varying among different feedstock origins, fractions and processing. The basic and non-basic nitrogen compounds identified in hydrotreated gas oils suggest they are resistant to nitrogen removal. For basic nitrogen compounds these included alkylated pyridines, quinolines, benzoquinolines, hydroquinolines and hydrobenzoquinolines. The non-basic nitrogen compounds identified were dominated by carbazole and its alkyl-substituted derivatives.

### **1.2.3 Hydrodenitrogenation**

Hydrodenitrogenation (HDN) is nitrogen removal by hydrogenation to produce hydrocarbon products and ammonia, typically occurring simultaneously with hydrodesulfurization (HDS) and hydrodeoxygenation (HDO) during hydrotreatment, where feed oil is reacted at moderate temperature and high hydrogen pressure with a metal catalyst on an acidic support, e.g. NiMo/ $\gamma$ -Al<sub>2</sub>O<sub>3</sub>. Girgis and Gates (1991), Prins (2001) and Furimsky and Massoth (2005) all provide comprehensive reviews of HDN literature. Prins (2001) gives particular attention to detailed mechanisms of catalytic HDN. The basic mechanisms and pathways of HDN of aromatic heterocyclic nitrogen compounds will be explored.

#### **1.2.3.1 The Basic Mechanism of HDN**

Girgis and Gates (1991), Furimsky and Massoth (2005) and Prins (2001) all describe the basic mechanism of HDN during hydroprocessing conditions with a conventional catalyst, such as NiMo/ $\gamma$ -Al<sub>2</sub>O<sub>3</sub>. The essential reactions of HDN of heterocyclic aromatic hydrocarbons involve first the hydrogenation of the nitrogen containing ring (Girgis and Gates, 1991; Prins et al., 1997; Furimsky and Massoth, 2005). This can occur before or after hydrogenation of other aromatic rings in the structure of the hydrocarbon. Then, hydrogenolysis of the C – N bond

of the reaction intermediate, typically a saturated amine, can take place by  $\text{NH}_3$  elimination (Prins et al., 1997). Many authors agree that direct cleavage of a C – N bond in an aromatic ring does not occur under normal hydroprocessing conditions (Girgis and Gates, 1991; Prins, 2001; Furimsky and Massoth, 2005). The heteroatomic ring must first be hydrogenated to reduce the relatively large activation energy, due to the C – N bond strength, required for the hydrogenolysis of the nitrogen heteroatom. Prins (2001) describes the mechanism for subsequent hydrogenolysis of the aliphatic C – N bond by an elimination reaction or  $\text{NH}_2\text{--SH}$  substitution, followed by C – S hydrogenolysis on a Ni-Mo catalyst surface (Nelson and Levy, 1979). Since hydrogenation of the heteroatomic ring must occur before hydrogenolysis of the C – N bond of the reaction intermediate, the equilibrium of these two reactions can affect rates of overall HDN if hydrogenolysis of the C – N bond is significantly slower than hydrogenation of the heteroatomic ring (Girgis and Gates, 1991). Furimsky and Massoth (2005) note that hydrogenation of aromatic hydrocarbons and alkenes is part of the overall HDN mechanism, especially at high HDN conversions. Also, that the specific HDN mechanism differs from reactant to reactant and is affected by a myriad of other factors such as temperature, catalyst employed, residence time,  $\text{H}_2\text{S}/\text{H}_2$  ratio, etc.

### 1.2.3.2 Pathways of HDN of Pyridine

Prins (2001) proposed a schematic of the reaction network of the HDN of pyridine as shown in Figure 1-3. The hydrogenation of pyridine to piperidine (1) is inferred to occur on sulfur deficient sites of the catalyst surface from evidence that  $\text{H}_2\text{S}$  hinders the progression of that step. Both the ring opening (2) and C – N bond cleavage by hydrogenolysis (3) likely take place by elimination reactions and produce alkenes. Pentene, as a product of the elimination of pentylamine, has been observed, whereas, the bracketed 5-aminopentene from the elimination of piperidine (2) has not. There is however, observations from HDN experiments conducted at high  $\text{H}_2\text{S}$  pressure ( $P_{\text{H}_2} = 4\text{MPa}$ ,  $P_{\text{H}_2\text{S}} = 8\text{MPa}$ ) of products that

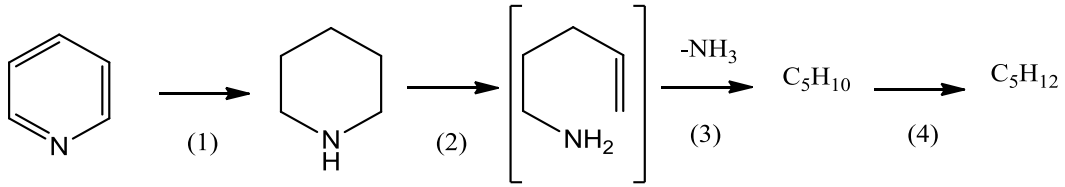


**Figure 1-3** Schematic of the reaction network of the HDN of pyridine (Prins, 2001)

strongly suggest the existence of 5-aminopentene and therefore, the accuracy of Figure 1-3 (Prins, 2001). Pyridine – piperidine (1) equilibrium is quickly obtained during typical hydrotreating conditions with either compound as the reactant, as indicated by evidence from Cocchetto and Satterfield (1976).

High hydrogen partial pressures are required to overcome the unfavourable equilibrium of hydrogenation of pyridine (Cocchetto and Satterfield, 1976). The rate of hydrogenation of pyridine to piperidine is as low as the ring opening of piperidine on Ni-Mo and Co-Mo catalysts at 300 °C and 3 MPa. Since, ring opening (2) is enhanced by H<sub>2</sub>S, while hydrogenation of pyridine to piperidine (1) is slowed, the H<sub>2</sub>S/H<sub>2</sub> ratio may promote or hinder the overall HDN of pyridine near these conditions (Prins, 2001). McIlvried (1971) performed experiments with piperidine, which determined that the HDN of piperidine followed pseudo-first order kinetics. These experiments showed the inhibition of HDN by piperidine and ammonia products, as indicated by a reduction in HDN rate with increasing piperidine feed concentration. The effect of alkyl substitution of the pyridine heteroatomic ring has been explored (Cerny, 1979). Cerny (1979) concluded that alkyl substitution of pyridine, especially at the 2- and 2,6-positions, likely result in steric effects that discourage HDN.

Disproportionation reactions have been inferred to take place from the observation of disproportionation products such as *n*-pentylpiperidine. Prins (2001) notes that at relatively high amine intermediate concentrations, piperidine and pentylamine react to produce *n*-pentyl-piperidine by-product (Jian and Prins,

1998). This by-product is then denitrated at high reactant conversions. Furimsky and Massoth (2005) suggest that disproportionation reactions producing *n*-pentylpiperidine, 2-*n*-pentylpiperidine and other observed uncommon products are a result of either reduced Ni(Co)Mo/Al<sub>2</sub>O<sub>3</sub> catalysts or lack of H<sub>2</sub>S donating species in the feed.

### **1.2.3.3 Pathways, Mechanisms and Reactivity of HDN of Large Polycyclic Aromatic Nitrogen Compounds**

Furimsky and Massoth (2005) indicate that there is a lack of information available on the formation of primary products of the HDN of acridine and benzoquinolines. Therefore, only speculative mechanisms for the overall HDN may be proposed. Prins (2001) notes that the HDN of larger molecules should occur in principle similarly to that of smaller nitrogen-containing compounds. Prins (2001) proposes a generalized pathway for the HDN of these larger nitrogen compounds. First, at least both the nitrogen-containing ring and a neighbouring ring are hydrogenated. Then, after possibly more hydrogenation of fused rings, hydrogenolysis of the C – N bond occurs via elimination. An example of this is reported by Nagai et al. (1986), where the C – N hydrogenolysis of acridine is posited to take place after the successful hydrogenation of two neighbouring rings forming an octahydroacridine intermediate. Alternatively, octahydroacridine can undergo further hydrogenation to perhydroacridine and proceed with nitrogen removal by a double elimination reaction. Prins (2001) also comments on the reactivity of larger multi-ring aromatic compounds, stating that these compounds react faster than smaller nitrogen-containing compounds because of the larger compounds' higher adsorption constants and the weaker aromatic character of the heteroatomic ring.

#### *1.2.3.3.1 Acridine*

Two reaction networks for the HDN of acridine have been proposed by two separate works, one by Zawadski et al. (1982) and another by Nagai et al.

(1986). The study by Nagai et al. (1986) discovered the existence of multiple hydrogenation equilibria during the HDN of acridine over a sulfided Mo/Al<sub>2</sub>O<sub>3</sub> catalyst at temperatures ranging from 280 – 380 °C, a total pressure of 10.1 MPa, in a continuous flow microreactor. Figure 1-4 shows the reaction network of the HDN of acridine proposed by Nagai et al. (1986). Acridine is quickly hydrogenated to 9,10-dihydroacridine at temperatures as low as 280 °C. After subsequent hydrogenation to octahydroacridine and perhydroacridine, nitrogen removal occurred above 300 °C. The authors indicate that above 320 °C acridine seems to be in equilibrium with perhydroacridine, with hydrogenolysis of the saturated C – N bond of perhydroacridine to give dicyclohexylmethane as the rate determining step. At 340 °C, Nagai et al. (1986) observed that the major reaction product distribution consisted of largely perhydroacridine and dicyclohexylmethane, with little acridine or dihydroacridine present.

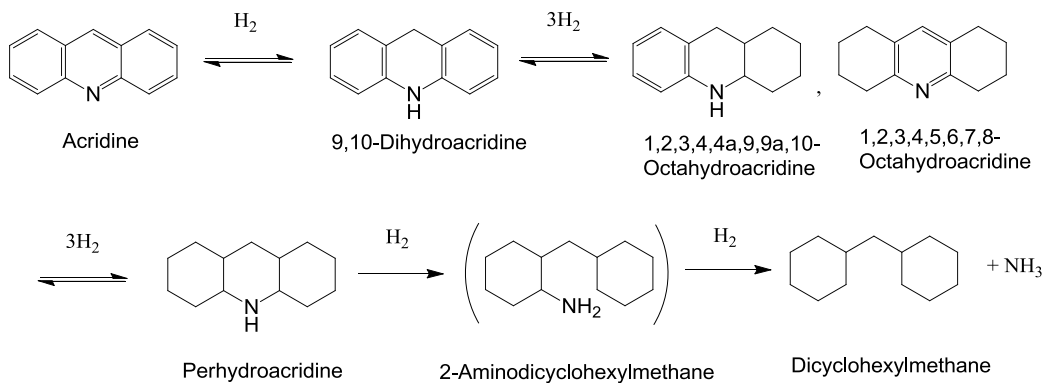


**Figure 1-4** Reaction network of the HDN of acridine (Nagai et al., 1986)

The schematic of hydrodenitrogenation of acridine proposed by Zawadski et al. (1982), with first-order rate constants for each pathway, is shown in Figure 1-5. This scheme suggests that the major HDN product is dicyclohexylmethane, although the HDN products were never identified; this agrees with Nagai et al.

(1986) (Furimsky and Massoth, 2005). Similar to the results of Nagai et al. (1986), this network confirms that acridine rapidly hydrogenates to dihydroacridine, thereafter, successively hydrogenating to octahydroacridine and

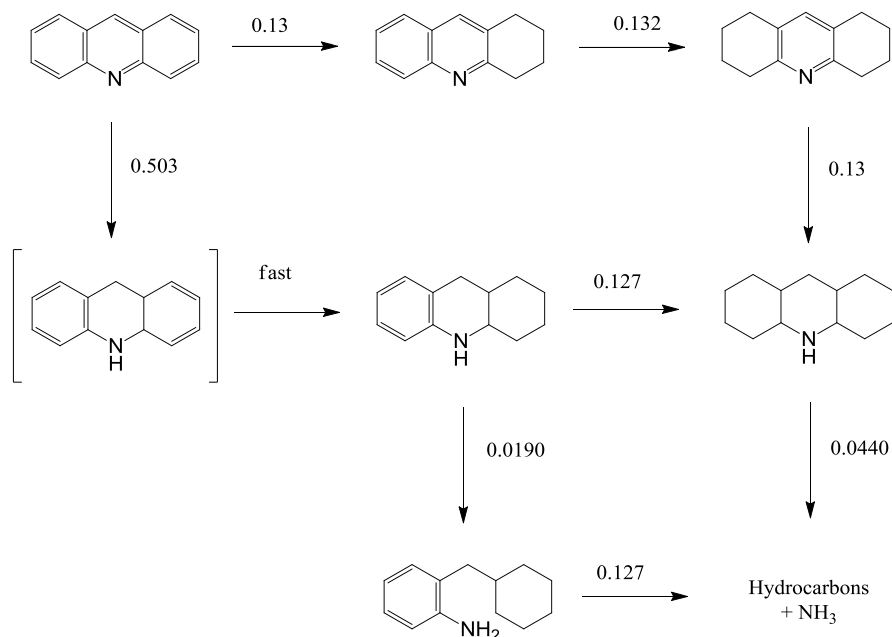


**Figure 1-5** Schematic of the HDN reaction network of acridine (Zawadski et al., 1982; Girgis and Gates, 1991). The numbers represent the pseudo-first-order rate constants in (g carrier oil)/(g<sub>cat</sub>·s) at 367 °C, 13.7 MPa, and 0.5 wt % acridine in the feed.

perhydroacridine. Subsequent hydrogenolysis of the perhydroacridine C – N bond occurred at temperatures above 300 °C, which again agrees with Nagai et al (1986). Girgis and Gates (1991) suggest that acridine and 9,10-dihydroacridine are in equilibrium since at short reaction times both are equally present in the product mixture. Like quinoline reaction networks, the primary hydrogenation product of hydrogenation of the heteroatomic ring is formed quicker than the primary hydrogenation product by hydrogenation of an adjacent ring. Girgis and Gates (1991) attributed this to larger  $\pi$ -electron density of the heteroatomic ring. Note that both schemes for the HDN of acridine support the requirement of the

hydrogenation of at least the nitrogen-containing ring and one other aromatic ring before nitrogen removal can take place.

The kinetics of acridine have been limited to the assumption of pseudo-first-order kinetics in the reactant concentration (Girgis and Gates, 1991). Both the hydrogenation and hydrogenolysis reactions were found to be kinetically important (Girgis and Gates, 1991). Also, steric effects may have greater influence on the relative reaction rates within the acridine network than quinoline, due to its 3 – ring structure. Nagai et al. (1986) found the reaction order to be 0.5 in acridine concentration (0.05 – 0.4 wt%) and 0.9 to 0.2 in H<sub>2</sub> pressure (2.2 – 13.0 MPa). The authors observed that H<sub>2</sub>S inhibited the hydrogenolysis of perhydroacridine. Furimsky and Massoth (2005) indicate that this is not typical, as H<sub>2</sub>S generally promotes hydrogenolysis. They believe that the unpromoted Mo/Al<sub>2</sub>O<sub>3</sub> catalyst may account for this observation. Both Furimsky and Massoth (2005) and Girgis and Gates (1991) comment on the low activity of acridine at low hydrogen partial pressures. Girgis and Gates (1991) note that acridine requires appreciably more H<sub>2</sub> than quinoline, stating that at 342 °C, 13.6 MPa of hydrogen was needed to achieve the same rate constant obtained with quinoline at 3.4 MPa. Furimsky and Massoth (2005) attribute the low activity of acridine relative to smaller molecules to the greater number of reaction steps needed to complete nitrogen removal, the higher H<sub>2</sub> consumption, and significance of steric effects.

#### *1.2.3.3.2 5,6- and 7,8-Benzoquinoline*

There are three prominent studies addressing the HDN of 5,6- and 7,8-benzoquinoline (Shabtai et al. (1989); Moreau et al. (1988); Malakani et al. (1987)). A schematic of the HDN reaction network of 5,6-benzoquinoline with accompanying pseudo-first-order rate constants proposed by Shabtai et al. (1989) is illustrated in Figure 1-6. This investigation was carried out at 340 °C and 17 MPa of H<sub>2</sub> over a sulfided CoMo/Al<sub>2</sub>O<sub>3</sub> catalyst. Shabtai et al. (1989) also report the change of the product distribution with time for the HDN of 5,6-

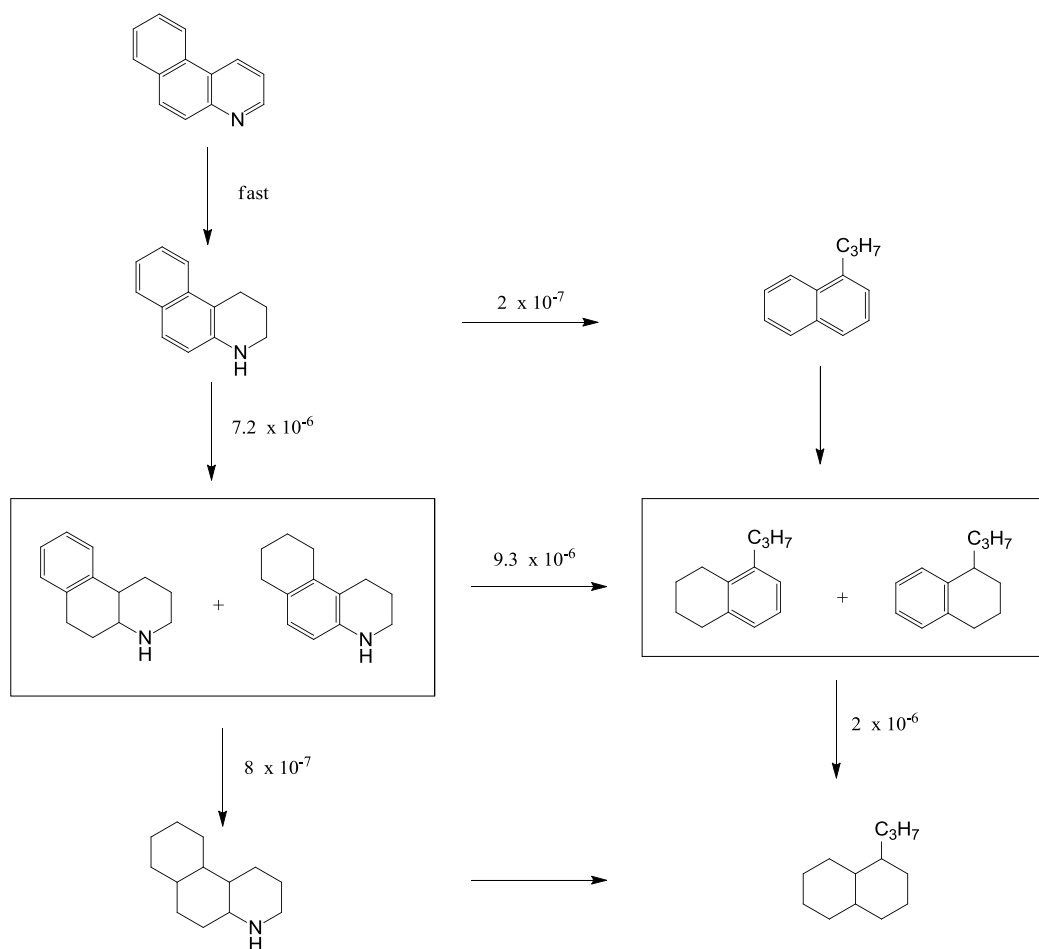


**Figure 1-6** Schematic of the reaction network of HDN for 5,6-benzoquinoline with pseudo-first-order reaction rate constants in  $L/(g_{cat} \cdot s)$  at  $300\text{ }^\circ\text{C}$  (Shabtai et al., 1989)

benzoquinoline at  $280\text{ }^\circ\text{C}$ , 17 MPa over a sulfided  $CoMo/Al_2O_3$  catalyst. This product distribution established the preference of hydrogenation of the heteroatomic ring over that of the adjacent aromatic rings. Likewise, in the reaction network shown in Figure 1-6, 1,2,3,4-tetrahydro-5,6-benzoquinoline is the only primary hydrogenation product formed from the hydrogenation of the nitrogen-ring. Cleavage of the C – N bond by hydrogenolysis was found to be slow, which was attributed to strong resonance stabilization of the N – ring (Girgis and Gates, 1991). The dominant pathway proceeded through nitrogen

removal of an octahydrobenzoquinoline intermediate to generate propyltetralins. Shabtai et al. (1989) reported that the activation energies for the hydrogenation were much lower than hydrogenolysis, being 50 – 54 kJ/mol and 100 – 205 kJ/mol, respectively. Furimsky and Massoth (2005) remark on the dilatory initial hydrogenation of the heteroatomic ring, which was as much as 10 times slower than that of quinoline. However, the hydrogenation still transpired too rapidly to be measured. Prins (2001) attributed this slower hydrogenation compared to quinoline to the angular shape of benzoquinoline, akin to phenanthrene. Girgis and Gates (1991) mention that in this study the rate constants for hydrogenation and hydrogenolysis decreased and increased, respectively, with H<sub>2</sub>S concentration. Furthermore, this observation agreed with results obtained by Satterfield and Yang (1984).

Moreau et al. (1988) published a different reaction network for the HDN of 5,6-benzoquinoline, which contained two, instead of one, primary hydrogenation products. This investigation was carried out at 340 °C and 7 MPa of H<sub>2</sub> over a sulfided Ni-Mo/Al<sub>2</sub>O<sub>3</sub>. One primary hydrogenation product was formed from the hydrogenation of the nitrogen-ring, the other from the hydrogenation of an adjacent aromatic ring. In contrast to results obtained by Shabtai et al. (1989), the dominant route for HDN took place by the hydrogenolysis of a 1,2,3,4-tetrahydro-5,6-benzoquinoline to form propyl-naphthalene, without creation of an aniline intermediate (Girgis and Gates, 1991). However, Furimsky and Massoth (2005) mention that tetrahydronaphthalene was also generated in appreciable quantities. No hydrogenation of the terminal aromatic ring was observed in this study, similar to the finding of the high activation energy for this step, 165 kJ/mol, reported by Shabtai et al. (1989). Girgis and Gates (1991) suggest that the differences in the observed reaction networks of Shabtai et al. (1989) and Moreau et al. (1988) are due to the different hydrogen pressure employed in each experiment, but note that no definitive assessment could be made. Likewise, Furimsky and Massoth (2005) comment that the smaller amounts of propyl-naphthalene produced relative to saturated and partially saturated products

by Shabtai et al. (1989) compared to Moreau et al. (1988) was due to the higher H<sub>2</sub> pressure and lower temperature.

A schematic of the HDN reaction network of 7,8-benzoquinoline is provided in Figure 1-7. Contrary to the behaviour observed by 5,6-benzoquinoline, 7,8-benzoquinoline forms 3 primary hydrogenation products. Similar to 5,6-benzoquinoline, the dominant hydrogenation product was found to be the hydrogenation of the heterocycle; in agreement with other non-quantitative studies by Malakani et al. (1987) and Shabtai et al. (1978b), who observed similar product distributions. This agreement was unsurprising given the near identical experimental conditions. However, there was disagreement as to what the prominent hydrocarbon HDN product was. Propylnaphthalene is reported by Moreau et al. (1988) and Shabtai et al. (1978), while propyltetralin is proposed by Malakani et al. (1987). Again, Girgis and Gates (1991) attribute this disagreement to differing hydrogen partial pressures used in the studies. Malakani et al. (1987) showed that the presence of H<sub>2</sub>S favoured hydrogenolysis and inhibited hydrogenation of the aromatic rings, but did not affect the overall nitrogen removal of 7,8-benzoquinoline. 7,8-benzoquinoline was determined to be more reactive than 5,6-benzoquinoline, and both more reactive than acridine, as indicated by a study conducted by Katti and Gates (1986) in a continuous flow reactor fed a mixture of strong nitrogen bases.

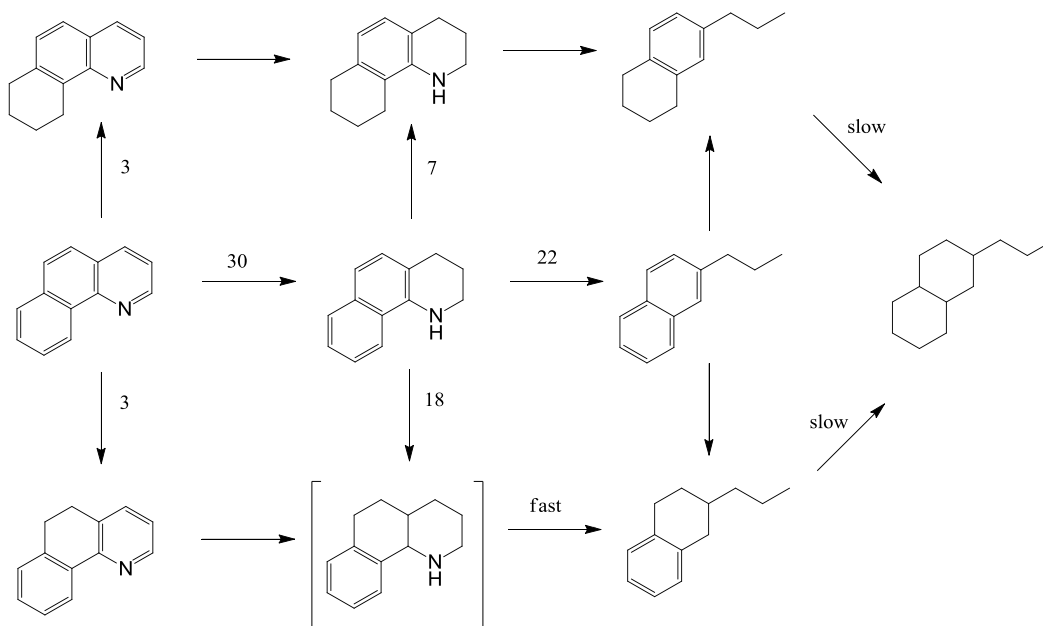


**Figure 1-7** Schematic of the reaction network of HDN for 7,8-benzoquinoline with the relative values of the pseudo-first-order reaction rate constants at 340 °C proposed by Moreau et al. (1988)

### 1.2.3.3.3 Carbazole

Furimsky and Massoth (2005) review much of the literature regarding carbazole, some of which is presented here. Three studies by Nagai et al. (1988; 1993; 1995) were conducted over a range of catalysts including conventional sulfided NiMo/Al<sub>2</sub>O<sub>3</sub>, nitride and carburized Mo/Al<sub>2</sub>O<sub>3</sub>. A schematic of the reaction network of the HDN of carbazole is given in Figure 1-8. This schematic illustrates the gradual hydrogenation of carbazole involving at least 4 equilibrium systems. The distribution of hydrogenated nitrogen-intermediates were also determined in these studies and was similar to the distribution published by Ho (1988), whom investigated the HDN of 3-ethyl-carbazole. It was discovered that hydrogenation of carbazole to octahydrocarbazole was required before hydrogenolysis of the C – N bond could occur, regardless of catalyst used. Liaw et al. (1997) found that over NiMo/Al<sub>2</sub>O<sub>3</sub> catalyst, fully saturated hydrocarbons in Figure 1-8 were the predominant products at temperatures above 600 K, with only trace amounts of cyclohexylbenzene detected. During the HDN of carbazole over

a Mo<sub>2</sub>N at 10 MPa, without H<sub>2</sub>S present, hydrogenolysis of the C – N bond of hexylhydrocarbazole was a minor pathway for nitrogen removal, with cyclohexylbenzene only detected above 600 K. Similar observations were made by Szymanska et al. (2003), which was conducted over a bulk Mo<sub>2</sub>C catalyst with 50 ppm of sulphur present at 633 K and 6 MPa. This resulted in a selectivity ratio of bicyclohexyl/cyclohexylbenzene of 9, without biphenyl being detected. Like acridine, the hydrogenation of carbazole to tetrahydrocarbazole over both reduced and sulfided Mo/Al<sub>2</sub>O<sub>3</sub> catalysts reached equilibrium at 633 K and 593 K, respectively. At 573 K, however, the hydrogenation of carbazole was far from equilibrium. Furimsky and Massoth (2005) remarked that this suggests that at lower temperatures nitrogen removal was limited by the hydrogenation of carbazole.

The HDN reactivity of five-membered nitrogen-compounds follows the order pyrrole > indole > carbazole (Furimsky and Massoth, 2005). This is supported by first order rate constants evaluated by Stern (1979), who reacted equimolar mixtures of the aforementioned nitrogen compounds over several sulfided catalysts. Nagai et al. (1999) estimated the rate constants of HDN of carbazole over several Mo nitrides at 300 °C and a H<sub>2</sub> pressure of 10 MPa. They found that the rate constants for hydrogenated intermediates were at least an order of magnitude greater than that of hydrogenolysis to hydrocarbon products. Investigation of the HDN of methyl and polymethyl substituted carbazoles was carried out by Wiwel et al. (2000). They determined the rate constants of these compounds relative to unsubstituted carbazole in a diesel oil fraction over a sulfided CoMo/Al<sub>2</sub>O<sub>3</sub> catalyst at 350 °C and 3 MPa of hydrogen. The retarding effect of any ring substitution, especially in the 1- position, was found to be significant.

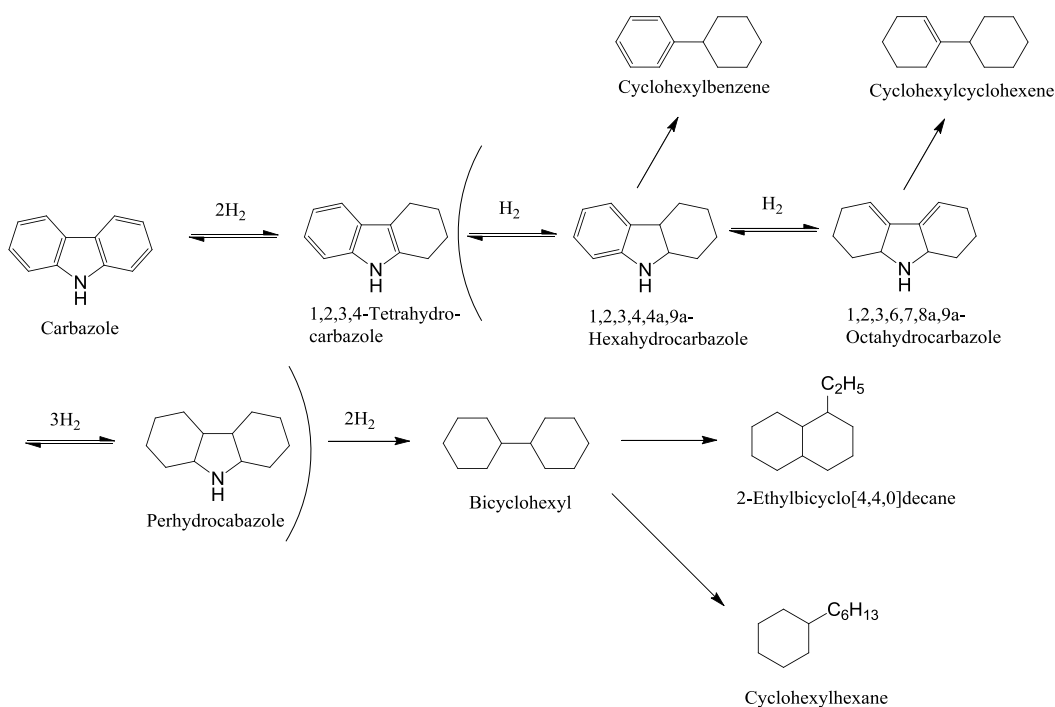


**Figure 1-8** Schematic of the reaction network of the HDN of carbazole (Nagai et al., 1988)

#### 1.2.3.4 Inhibition of HDN from the Presence of Other Compounds

Hydrodenitrogenation of nitrogen compounds can be inhibited by other chemical species present in hydrotreatment feeds, especially other more basic nitrogen species, by way of competitive adsorption onto the catalyst active sites. Prins (2001) notes that inhibition is not only caused by the different intrinsic reactivity between reactant compounds, but also from product intermediates and reaction end products including  $\text{H}_2\text{O}$ ,  $\text{H}_2\text{S}$  and  $\text{NH}_3$ . Adsorption equilibrium, and therefore inhibitive effects in general, have been shown to increase strongly in the following order: aromatic hydrocarbons < sulphur compounds < oxygen compounds < nitrogen compounds (Girgis and Gates, 1991; Prins, 2001). Prins (2001) indicates that reaction of compounds from one category of compounds will be inhibited by a species from another – the higher adsorbing species inhibiting the weaker adsorbing species. Moreover, compounds within the same category can mutually affect their hydrotreating rates. For example, Morávek et al. (1990)

investigated the competitive reactions of pyrrole, pyrrolidine, pyridine, and piperidine over a NiMo/Al<sub>2</sub>O<sub>3</sub> catalyst. The authors demonstrated that pyridine and pyrrolidine strongly inhibited the nitrogen removal of pyrrole.

Girgis and Gates (1991) provide a comprehensive review of the effect that a range of additive compounds have on HDN, some of which will be summarized here. From investigation of the influence of quinoline on a naphthalene reaction network, Bhide (1979) and Lo (1981) found that the inhibition of the HDN of quinoline by aromatic hydrocarbons was minimal. Similarly, sulphur compounds were also deemed weak inhibitors of HDN. Bhide (1979) evaluated the pseudo-first-order rate constants of the HDN of quinoline with a significant amount of dibenzothiophene additive. The overall rate constant for nitrogen removal remained relatively unchanged and the only discernable effect was 25% increase in the rate of C – N bond hydrogenolysis reaction. Nagai et al. (1986) studied the effect of several sulphur compounds on the HDN of acridine at conversions less than 20%. It was carried out in a flow reactor, at 208 – 360°C, 10 MPa with 0.25 wt % acridine in a xylene solvent over sulfided and unsulfided Mo/Al<sub>2</sub>O<sub>3</sub>. Addition of the sulphur compounds was found to inhibit the HDN of acridine, the yield of dicyclohexylmethane decreasing with increasing sulphur concentration.

Girgis and Gates (1991) summarized the effects of oxygen compound addition on hydrodenitrogenation, mentioning two generalized trends. The first trend was that competitive adsorption involving nitrogen and oxygen compounds results in mild inhibition of HDN at low concentrations. The second trend was that at high hydrodeoxygenation conversions, when appreciable amounts of H<sub>2</sub>O were created, nitrogen removal was enhanced slightly.

Bhide (1979) studied the effect of quinoline on the HDN of indole. Addition of 0.5 wt % quinoline to 0.5 wt % indole depressed the pseudo-first-order rate constant by a third, indicating significant inhibition by quinoline and its reaction products. Inhibition of the HDN of quinoline by addition of indole had a weaker inhibitory effect, attributed to its weaker adsorption (indole being non-basic). Self-inhibition was also addressed by experiments of mixtures of quinoline

and naphthalene, with quinoline varied from 0.2 to 2.0 wt % and naphthalene held constant. The overall nitrogen removal decreased significantly with the increasing feed concentration.

#### **1.2.3.5 The Effects of H<sub>2</sub> and H<sub>2</sub>S Partial Pressures on HDN**

Furimsky and Massoth (2005) state that the H<sub>2</sub>S/H<sub>2</sub> ratio is a critical parameter for maintaining the HDN activity of a catalyst. The H<sub>2</sub>S/H<sub>2</sub> ratio determine the number and type of active sites involved in HDN by establishing the number of coordinatively unsaturated sites (CUS), which is a catalyst surface complex that has one or more open coordination sites to accomodate a ligand and make sulphur ions available. Furimsky and Massoth (2005) further remark that the essential role of H<sub>2</sub>S in an HDN reaction network is to ensure that there is an optimal distribution of Brønsted sites and CUS. This promoting effect of H<sub>2</sub>S on HDN is then diminished with increasing H<sub>2</sub>S/H<sub>2</sub> ratio, i.e. the increase in rate of hydrogenolysis in an HDN reaction network in the presence of H<sub>2</sub>S is offset by the inhibition of ring hydrogenation within the same network (McIlvried, 1971; Furimsky and Massoth, 2005). Topsøe et al. (1989) demonstrated that the effect of H<sub>2</sub>S/H<sub>2</sub> ratio on relative HDN conversion transitions from a promotional regime to an inhibitory one, with an optimal ratio for nitrogen removal. This optimum in HDN performance is the result of two competing effects of the H<sub>2</sub>S/H<sub>2</sub> ratio. The ratio should not be large enough to cause inhibition of the hydrogenation of aromatic rings and yet needs to be sufficiently high to provide an effective rate of C – N bond hydrogenolysis reactions in the overall HDN reaction network. Therefore, it is understood that changes in the HDN system caused by changes in H<sub>2</sub>S partial pressure are the consequence of the combined effect of H<sub>2</sub>S and H<sub>2</sub> (Furimsky and Massoth, 2005).

Results of Vivier et al. (1991) demonstrated that the optimal H<sub>2</sub>S/H<sub>2</sub> ratio may be dependent on the type of nitrogen compound. Furthermore, results from Vit and Cinibulk (2002) suggest that the effect of H<sub>2</sub>S on HDN depended on the catalyst. For example, in the HDN of pyridine over sulfided Mo/Al<sub>2</sub>O<sub>3</sub>,

hydrogenation of the heteroatomic ring was inhibited by H<sub>2</sub>S and the hydrogenolysis of piperidine enhanced. Hanlon (1987) observed that increasing H<sub>2</sub> pressure from 2.5 to 10.0 MPa while holding constant the H<sub>2</sub>S/H<sub>2</sub> ratio (3.2 x 10<sup>-3</sup>) had negligible effect on the HDN of pyridine. Similarly, Lacroix et al. (1999) found that a large increase in H<sub>2</sub> pressure had negligible effect on hydrogen activation. Consequently, Furimsky and Massoth (2005) suggest that the role of high H<sub>2</sub> pressures during hydroprocessing is to maintain an optimal H<sub>2</sub>S/H<sub>2</sub> ratio.

### 1.2.3.6 Catalysts for Hydrodenitrogenation

Hydrotreating catalysts were developed in the 1920s by German researchers attempting to liquefy coal (Prins, 2001). Typical commercial hydrotreating catalysts today consist of molybdenum with a cobalt or nickel promoted catalyst supported on  $\gamma$ -Al<sub>2</sub>O<sub>3</sub> (Topsøe et al., 1996). Nickel molybdenum supported on alumina catalysts are preferred for HDN reactions, whereas, cobalt molybdenum on alumina is used to promote HDS. Prins (2001) provides an extensive review of HDN catalysts including the structure and synthesis of classic metal sulphide catalysts, recently introduced metal carbide and nitride catalysts, and catalyst supports.

Prins (2001) states that in practice, supported metal oxide catalysts are sulfided under controlled conditions prior to operation in a hydrotreatment process. This is done because MoS<sub>2</sub> has high activity for heteroatom removal and is considered the actual catalyst with Ni and Co as promoters. Hydrotreating catalysts often include other additives such as P, B, F and Cl to alter catalytic and mechanical properties. Although more expensive, tungsten has similar chemical properties to molybdenum. Sulfided Ni-W/ $\gamma$ -Al<sub>2</sub>O<sub>3</sub> is known to have advantages over sulfided Ni-Mo/ $\gamma$ -Al<sub>2</sub>O<sub>3</sub> for hydrogenation at severe conditions.

A study by Eijbouts et al. (1991) investigated the HDN activity of transition metal sulfides, including Ir, Os, Pt, Re, Rh, Pd, Ru, Mo, and W on active carbon supports. Prins (2001) remarked on a resurgence of interest of

metal carbides and metal nitrides for HDN. The author indicated that these metals can hydrogenate aromatic rings at low temperature, and remove nitrogen by hydrogenolysis of aliphatic nitrogen rings effectively. However, this hydrogenolysis property led to appreciable cracking of product molecules into gaseous ones, making liquid product yield a concern. Moreover, sulphur present in the feed sulfided the catalyst. Supports other than alumina have been investigated and Luck (1991) provides a comprehensive review of Ni-Mo and Co-Mo catalysts supported on silica, silica-alumina, zeolites, activated carbon, and titania. Table 1-3 shows the composition and surface area, where reported, of HDN catalysts supported on alumina used in several studies.

**Table 1-3** Elemental composition and surface area of hydrodenitrogenation catalysts used in various studies

Study	Elemental composition (wt %)				Surface area (g/m <sup>2</sup> )
	<i>Ni</i>	<i>Co</i>	<i>Mo</i>	<i>P</i>	
Satterfield and Yang (1984)	3.3		15.0	1.4	176*
Jian and Prins (1998)	3		8		212
	3		8	2	174
Hanlon (1987)	2.4		10		
Liaw et al. (1997)	3.1		13.3		138*
		2.7	11.1		288*
Shabtai et al. (1989)	3 – 6	3 – 6	8		

\*determined by BET

## **1.2.4 Process Technologies for Hydroconversion and Hydrotreatment**

Hydroconversion is a process where high temperatures over 410 °C provide substantial thermal cleavage of the chemical bonds of the molecules comprising a heavy feed. Hydrogen addition is used to suppress coke formation and in the presence of catalyst, hydrogenate aromatics and remove sulfur. The objective of hydroconversion is to convert low grade materials into lighter more valuable products and transform near – solid vacuum residua into liquid products. On the other hand, hydrotreatment of feedstocks entails the use of milder temperatures below 410 °C to catalytically remove sulphur and nitrogen, as well as the hydrogenation of olefins and aromatics. Another objective of hydrotreatment is the removal of metals, usually in a separate catalytic reactor, where organo-metallic compounds are hydrogenated and decomposed, generating metal deposits on catalyst pores. Here the thermal reactions are not significant. The objective of hydrotreating processes is to transform the feed into low sulphur and nitrogen liquid products, as well as hydrogen sulfide and ammonia. The remainder of this section will review the process technologies used in these two processes.

### **1.2.4.1 Hydroconversion**

Currently there are three types of hydroconversion processing technology: fixed bed, catalytic ebullated bed, and slurry or additive-based processes.

#### *1.2.4.1.1 Fixed Bed*

Fixed bed reactors excel in the areas of scale-up and operations. Figure 1-9 shows the schematic diagram of a conventional fixed bed hydroconversion unit. Typical operating parameters for fixed-bed processing, in this case, atmospheric residue desulfurization or ARDS, can be found in Table 1-4. Since feeds with modest mineral and metals content accumulate in the interstices of the catalyst pellets causing shut downs due to high pressure drop, Athabasca and Cold Lake feeds are not feasible for this processing method. Moreover, feed stocks for fixed

bed residuum treating units are limited to < 250 ppm metals content to maintain a reasonable catalyst life. Two fixed bed processes have been developed to address feeds with higher metals content. Chevron's OCR Process features on-line catalyst replacement, which allows for the processing of feeds with metals content as high as 400 ppm (Gray, 2009). Feed is introduced to the reactor at the top and catalyst enters from the bottom. The countercurrent flow of residue and catalyst ensures that the highest concentration of contaminants encounters the most deactivated catalyst. Bunker reactor technology created by Shell has catalyst removed from the bottom of the reactor and fresh catalyst added at the top (Gray, 2009). Consequently, catalyst slowly moves downward through the reactor. Licensors for fixed-bed hydroconversion processes include: Chevron, Exxon, IFP and Shell (Gray, 2009).

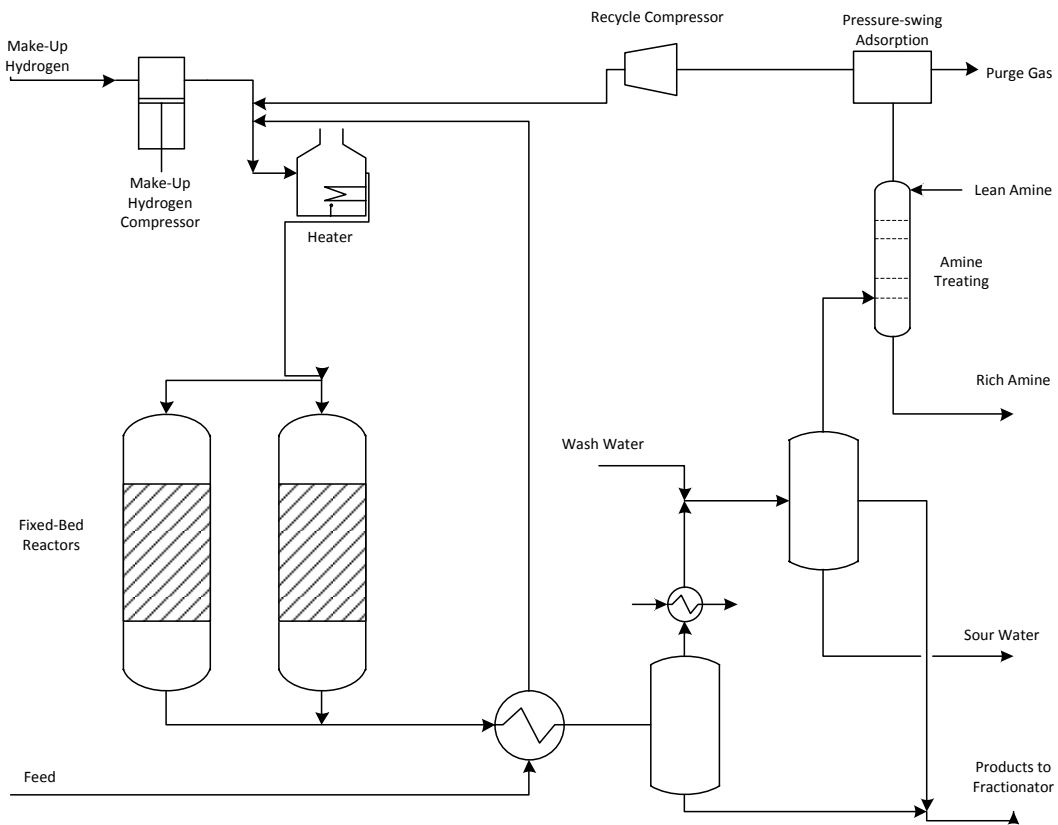


**Figure 1-9** Schematic diagram of a conventional fixed-bed residue hydroprocessing unit (Anon, 1998)

**Table 1-4** Operating parameters for a typical fixed-bed process (Topsøe et al., 1996)

<b>Operating Parameter</b>	<b>Operating Range</b>
Temperature	370 – 440 °C
H <sub>2</sub> Partial Pressure	8 – 13 MPa
LHSV	0.2 – 0.5 h <sup>-1</sup>
H <sub>2</sub> Consumption	100 – 175 Nm <sup>3</sup> /m <sup>3</sup>

#### 1.2.4.1.2 Catalytic Ebullated Bed

In order to prevent the plugging of the reactor by deposited metals and mineral solids in the feed, metal catalyst supported on alumina can be fluidized. Licensed processes for ebullated bed reactors include: Texaco's H-Oil and T-STAR (Texaco – Strategic Total Activity Retention) and the LC-Fining Process (Gray, 2009; Mohamed et al., 2010). In a typical ebullated bed reactor a mixture of hydrogen gas and liquid feed enter at the bottom of the reactor and flow upward through the expanded catalyst bed. Hydrogen, liquid products and hydrocarbon vapours exit from the top of the reactor. A recycle stream of liquid is drawn down a tube and pumped to a distributor at the bottom of the reactor. The flow rate of the recycle stream can be up to 5 – 10 times that of the feed rate and provides the energy to expand the bed. Hydrogen gas is recycled 3 – 4 times the consumption rate to keep hydrogen in excess in the liquid phase. Fresh catalyst is added continuously at the top of the reactor to maintain operating temperature and constant conversion. The general parameters for ebullated bed operation are given in Table 1-5. Advantages for the processing of heavy residues and bitumen feeds include: the expanded bed prevents clogging of the reactor by solids, the liquid recycle ensures good mixing within the reactor, and long operations can occur without shutting down because catalyst can be withdrawn continuously. Prevention of solids formation in the hydroconversion product stream is a concern and often limits conversions to 60 – 80% of the 524 °C+ fraction.

**Table 1-5** Operating parameters for a typical catalytic ebullated bed process (Topsøe et al., 1996)

<b>Operating Parameter</b>	<b>Operating Range</b>
Temperature	420 – 450 °C
H <sub>2</sub> Partial Pressure	10 – 15 MPa
LHSV	0.1 – 1.5 h <sup>-1</sup>
H <sub>2</sub> Consumption	150 – 300 Nm <sup>3</sup> /m <sup>3</sup>

#### 1.2.4.1.3 Slurry or Additive Based Processes

In these processes, finely divided additives are added to the feed and are circulated within the reactor. They enhance catalytic activity of the reactor and exit with unconverted residue but are not accumulated within the reactor. Instead of simultaneous HDS, HDN, hydrodemetallization, and cracking reactions, the objective of these additive processes is to maximize the conversion of residue with minimum coke formation. Since the reactive phase consists of a slurry or suspension of finely powdered catalyst, an upflow tubular reactor, where a liquid suspension of additive flows upward with hydrogen gas, is used. Cost restricts the types of additives employed. Emphasis is placed on tailoring the type and amount of additive to control coke formation in the reactor. Additives include: powdered coal impregnated with iron salts, iron oxide waste, and organometallic compounds such as molybdenum naphthenates. Table 1-6 summarizes some of the processes presented in literature based on laboratory, pilot and demonstration plants. None of the processes have been commercialized and all used tubular reactors.

**Table 1-6** List of various slurry hydroconversion processes

<b>Process</b>	<b>Company</b>	<b>Catalyst</b>	<b>Conditions</b>	<b>Reference</b>
Combi Cracking	Veba Oil	Fe <sub>2</sub> O <sub>3</sub>	200bbl/d, 440-490°C, 15-25 MPa	Niemann et al., 1988
CANMET Hydrocracking	CANMET	FeSO <sub>4</sub>	5000bbl/d, 430-440°C, 24 MPa	Pruden et al., 1989
HDH	PDVSA	Dispersed Mo	200bbl/d, 420-480°C, 14 MPa	Marzin et al., 1988

#### 1.2.4.2 Hydrotreatment

Hydrotreatment is differentiated from hydroconversion in that it is intended for the selective removal of heteroatoms from the feed with negligible cracking of hydrocarbons. The main role of hydrotreaters is to meet finished product specifications and preparation of feed for downstream units. The chemistry involved in hydrotreatment includes: desulfurization, denitrogenation, deoxidation, hydrogenation of chlorides, hydrogenation of olefins, hydrogenation of aromatics, hydrogenation of organometallic compounds and deposition of metals, and coke formation. Figure 1-10 shows the schematic of a conventional hydrotreating process called diesel hydrotreating.

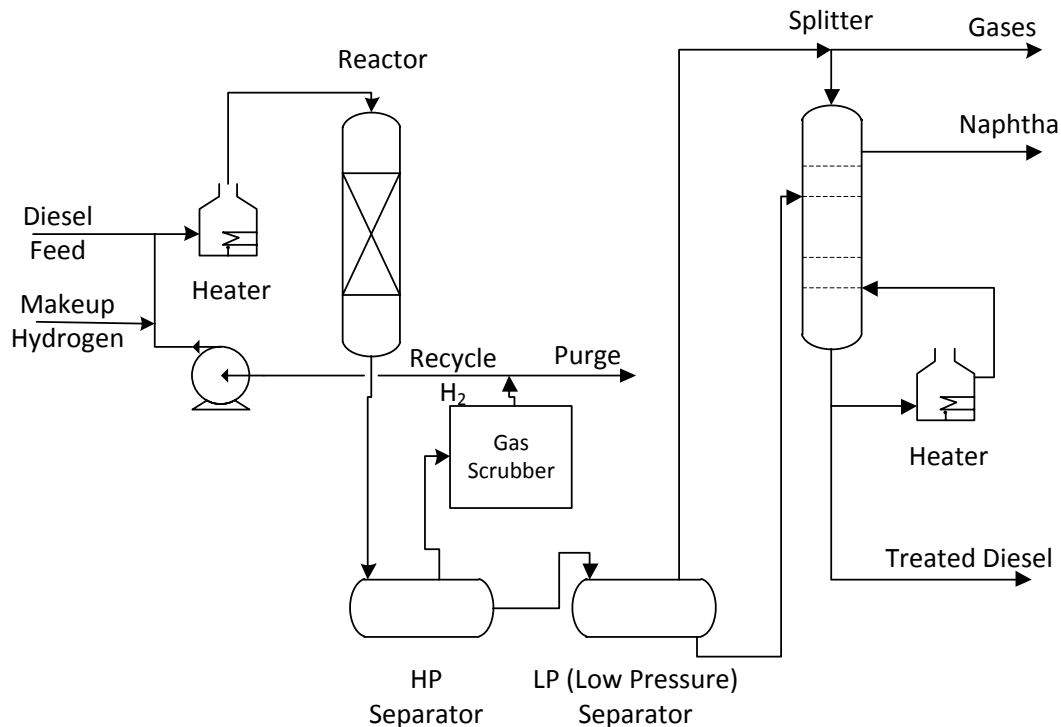


**Figure 1-10** Schematic of a diesel hydrotreating unit (Mohamed et al., 2010)

Feed is mixed with hydrogen gas and heated to reaction temperature by a furnace and then introduced to the top of a fixed bed reactor, which typically operates with liquid feed flowing downward over solid catalyst concurrent with hydrogen gas. Catalyst used is usually Co-Mo or Ni-Mo on  $\gamma$ -alumina comprised of 11 – 14 wt % Mo and 2 – 3 wt % of the Ni or Co promoter. Surface areas of the catalyst range from 150 – 200  $\text{m}^2/\text{g}$  giving high dispersion. The catalyst is present in the reactor as extruded cylinders (~2 mm diameter), lobed cylinders, or rings. Catalyst can often be regenerated in situ and then ultimately replaced after several regenerations. Reactor effluent is passed through a gas – liquid separator, where a hydrogen enriched gas is separated and recycled. Hydrogen sulfide is scrubbed from the hydrogen recycle stream because of its inhibiting effects on HDS kinetics and to reduce corrosion. Addition of cold make-up hydrogen gas at an intermediate point along the reactor controls both temperature and hydrogen partial pressure of the process. The treated liquid product is then fractionated.

Other process units and modifications available to tailor hydrotreatment for a specific feed and product specifications include: guard bed reactors and filters to remove solids, multiple points of adding quench gas, guarded beds using more than one type of catalyst, and upward flow reactor enabling counter-current contacting. Similar issues for fixed bed operation in hydroconversion processes also occur in hydrotreatment such as solids build up causing high pressure drops and poor mixing regimes with the reactor. Likewise, a major difficulty treating heavier feed stocks is their high metals content, circa 320 ppm. The operating parameters for the hydrotreatment of various feedstocks are presented in Table 1-7. Operating parameters and the boiling range of the feed determine the fraction of the feed in the vapour and liquid phase.

**Table 1-7** Operating parameters for hydrotreating different feedstocks (Heinrich and Kasztelan, 2001)

<b>Operating Parameter</b>	<b>Naphtha</b>	<b>Kerosene</b>	<b>Gas oil</b>	<b>Vacuum gas oil</b>	<b>Residue</b>
Boiling range (°C)	70-180	160-240	230-350	350-550	>550
Operating temperature (°C)	260-300	300-340	320-350	360-380	360-380
Hydrogen pressure (bar)	5-10	10-30	15-40	40-70	120-160
Hydrogen consumption (wt%)	0.05-0.1	0.1-0.2	0.3-0.5	0.4-0.7	1.5-2.0
LHSV* (h <sup>-1</sup> )	4-10	2-4	1-3	1-2	0.15-0.3

\* LHSV = Liquid volumetric flow rate at 15 °C (ft<sup>3</sup>/h)/(Volume of catalyst (ft<sup>3</sup>))

### 1.2.5 Knowledge Gaps

A limited number of studies have been conducted concerning the HDN of large multi-ring aromatic nitrogen compounds, as already been discussed (Nagai

et al. (1989, 1999); Shabtai (1978, 1989); Moreau (1988); Malakani et al. (1987)). However, these studies focused largely on acridine, benzoquinolines and carbazole. Although, extensive work has been undertaken investigating the HDN of quinoline as a model compound, results from Jokuty and Gray (1992) suggest that the HDN mechanism for nitrogen bases obtained from Athabasca bitumen derived crude oil consists of a multi-step process including the hydrogenation and cracking of fused rings to alkyl pyridines. This proposed mechanism differs significantly from reported mechanisms for quinoline. No studies have yet been conducted with large multi-ring nitrogen model compounds, with more than six rings, which act as models of predicted asphaltene molecular structures.

### **1.3 Objective**

The objective of this study is to determine the patterns and pathways of hydrogenation of large multi-ring nitrogen containing asphaltene model compounds. This objective will be achieved by seeking to answer the following questions:

1. Where does hydrogen addition occur on the parent model compound?
2. Does the heteroatomic ring preferentially hydrogenate?
3. Does significant nitrogen removal of these compounds occur at industrial hydrotreating conditions?
4. Are the pathways of hydrogenation observed for these model compounds similar to the reaction pathways reported for nitrogen compounds reported in literature?

## 1.4 References

- Akbarzadeh, K., H. Alboudwarej, W. Y. Svrcek and H. W. Yarranton. A generalized regular solution model for asphaltene precipitation from n-alkane diluted heavy oils and bitumens. *Fluid Phase Equilibria* **2005**, 232, 159-170.
- Anon. Chevron RDS Process. *Hydrocarbon Processing* **1998**, 77(11), 62.
- Bej, S. K., A. K. Dalai and J. Adjaye. Comparison of Hydrodenitrogenation of Basic and Nonbasic Nitrogen Compounds Present in Oil Sands Derived Heavy Gas Oil. *Energy & Fuels* **2001**, 15, 377-383.
- Bhinde, M. V. (1979). Quinoline Hydrodenitrogenation Kinetics and Reaction Inhibition. Newark, University of Delaware. **Ph. D. Dissertation.**
- Cerny, M. Hydrogenolysis of nitrogen-containing compounds on a cobalt-molybdenum catalyst. *Collection of Czechoslovak Chemical Communications* **1979**, 44(1), 85-98.
- Cocchetto, J. F. and C. N. Satterfield. Thermodynamic Equilibria of Selected Heterocyclic Nitrogen Compounds with Their Hydrogenated Derivatives. *Ind. Eng. Chem. Des. Dev.* **1976**, 15(2), 272-277.
- Cox, K. E. and L. Berg. Destructive catalytic hydrogenation of heterocyclic nitrogen compounds. *Chemical Engineering Progress* **1962**, 15(12), 54-55.
- Dorbon, M., I. Ignatiadis, J.-M. Schmitter, P. Arpino, G. Guiochon, H. Toulhoat and A. Huc. Identification of carbazoles and benzocarbasoles in a coker gas oil influence of catalytic hydrotreatment on their distribution. *Fuel* **1984**, 63(4), 565-570.
- Eijsbouts, S., V. H. J. d. Beer and R. Prins. Hydrodenitrogenation of quinoline over carbon-supported transition metal sulfides. *Journal of Catalysis* **1991**, 127(2), 619-630.

- Freund, H., M. G. Matturro, W. N. Olmstead, R. P. Reynolds and T. H. Upton. Anomalous side chain cleavage in alkylaromatic thermolysis. *Energy & Fuels* **1991**, 5, 840-846.
- Furimsky, E. and F. E. Massoth. Hydrodenitrogenation of Petroleum. *Catalysis Reviews* **2005**, 47, 297-489.
- Girgis, M. J. and B. C. Gates. Reactivities, Reaction Networks, and Kinetics in High-Pressure Catalytic Hydroprocessing. *Ind. Eng. Chem. Res.* **1991**, 30, 2021-2058.
- Gray, M. R. (2009). Course Notes - CH E 522 Fundamentals of Oil Sands Upgrading. Edmonton, AB, University of Alberta.
- Gray, M. R., R. R. Tykwinski, J. M. Stryker and X. Tan. Supramolecular Assembly Model for Aggregation of Petroleum Asphaltenes. *Energy & Fuels* **2011**.
- Groenzin, H. and O. C. Mullins. Molecular size and structure of asphaltenes from various sources. *Energy & Fuels* **2000**, 14, 677-684.
- Hanlon, R. T. Effects of  $P_{H_2S}$ ,  $P_{H_2}$ , and  $P_{H_2S}/P_{H_2}$  on the Hydrodenitrogenation of Pyridine. *Energy & Fuels* **1987**, 1, 424-430.
- Heinrich, G. and S. Kasztelan (2001). Hydrotreating. Conversion Processes. France, TECHNIP. **3**.
- Ho, T. C. *Catal. Rev.-Sci. Eng.* **1988**, 30.
- Hughey, C. A., R. P. Rodgers and A. G. Marshall. Resolution of 11 000 compositionally distinct components in a single electrospray ionization Fourier transform ion cyclotron resonance mass spectrum of crude oil. *Analytical Chemistry* **2002**, 74(16), 4145-4149.

- Jian, M. and R. Prins. Kinetics of the Hydrodenitrogenation of Decahydroquinoline over NiMo(P)/Al<sub>2</sub>O<sub>3</sub> Catalysts *Ind. Eng. Chem. Res.* **1998**, 37, 834-840.
- Jokuty, P. L. and M. R. Gray. Resistant Nitrogen Compounds in Hydrotreated Gas Oil from Athabasca Bitumen. *Energy & Fuels* **1991**, 5(6), 791-795.
- Jokuty, P. L. and M. R. Gray. Nitrogen Bases Resistant to Hydrodenitrogenation: Evidence against Using Quinoline as a Model Compound. *Ind. Eng. Chem. Res.* **1992**, 31, 1449-1457.
- Kanda, W., I. Siu, J. Adjaye, A. E. Nelson and M. R. Gray. Inhibition and Deactivation of Hydrodenitrogenation (HDN) Catalysts by Narrow-Boiling Fractions of Athabasca Coker Gas Oil. *Energy & Fuels* **2003**, 18, 539-546.
- Katti, S. S. and B. C. Gates. Catalytic Hydroprocessing of SRC-II Heavy Distillate Fractions. 6. Hydroprocessing of the Bases and Neutral Resins. *Ind. Eng. Chem. Process Des. Dev.* **1986**, 25, 618-626.
- Lacroix, M., C. Dumonteil, M. Breyse and S. Kasztelan. Hydrogen Activation on Alumina Supported MoS<sub>2</sub> Based Catalysts: Role of the Promoter. *Journal of Catalysis* **1999**, 185(1), 219-222.
- Liaw, S.-J., R. Lin, A. Raje and B. H. Davis. Hydrotreatment of coal-derived naphtha. Properties of zeolite-supported Ru sulfide catalysts. *Applied Catalysis* **1997**, 151, 423-435.
- Lo, H. S. (1981). Kinetic Modeling of Hydrotreating. Newark, University of Delaware. **Ph. D. Dissertation.**
- Luck, F. *Bull. Soc. Chim. Belgium* **1991**, 100, 781.
- Marzin, R., J. Guitan, J. Krasuk, F. Silva, A. Souto and B. Solari (1988). HDH, A process for residue conversion. 4th UNITAR/UNDP Conference on Heavy Crude and Tar Sands, Edmonton AB.

- McIlvried, H. G. Hydrodenitrification of Pyridine. *Ind. Eng. Chem. Des. Dev.* **1971**, 10, 125-130.
- McKay, J. F., J. H. Weber and D. R. Latham. Characterization of Nitrogen Bases in High-Boiling Petroleum Distillates. *Analytical Chemistry* **1976**, 48(6), 891-898.
- Mohamed, A. F., T. A. Alsahhaf and A. Elkilani (2010). Fundamentals of Petroleum Refining. Oxford, UK, Elsevier B. V.
- Morávek, V., J. C. Duchet and D. Cornet. Kinetic study of pyrrole and pyridine HDN on Ni-W and Ni-Mo catalysts. *Applied Catalysis* **1990**, 66(1), 257-266.
- Moreau, C., R. Durand, N. Zmimita and P. Geneste. Hydrodenitrogenation of Benzo(f)quinoline and Benzo(h)quinoline over a Sulfided NiO-MoO<sub>3</sub>/□-Al<sub>2</sub>O<sub>3</sub> Catalyst. *Journal of Catalysis* **1988**, 112, 411-417.
- Mushrush, G. W., E. J. Beal, D. R. Hardy and J. M. Hughes. Nitrogen compound distribution in middle distillate fuels derived from petroleum, oil shale, and tar sand sources. *Fuel Processing Technology* **1999**, 61, 197-210.
- Nagai, M., Y. Goto, A. Miyata, M. Kiyoshi, K. Hada, K. Oshikawa and S. Omi. Temperature-Programmed Reduction and XRD Studies of Ammonia-Treated Molybdenum Oxide and Its Activity for Carbazole Hydrodenitrogenation. *Journal of Catalysis* **1999**, 182(2), 292-301.
- Nagai, M., T. Masunaga and N. Hana-oka. Selectivity of Molybdenum Catalyst in Hydrodenitrogenation, Hydrodesulfurization, and Hydrodeoxygenation: Effects of Sulfur and Oxygen compounds on Acridine Hydrodenitrogenation. *Journal of Catalysis* **1986**, 101, 284-292.
- Nagai, M., T. Masunaga and N. Hana-oka. Hydrodenitrogenation of Carbazole on a Mo/Al<sub>2</sub>O<sub>3</sub> Catalyst. Effects of Sulfiding and Sulfur Compounds *Energy & Fuels* **1988**, 2(5), 645-651.

- Nelson, N. and R. B. Levy. The organic chemistry of hydrodenitrogenation. *Journal of Catalysis* **1979**, 58(3), 485-488.
- Niemann, K., K. Kretschmar, M. Rupp and L. Merz (1988). Upgrading of Alberta derived bitumen applying the VLC/VCC Technology. 4th UNITAR/UNDP Conference Heavy Crude Tar Sands, Edmonton, AB.
- Payzant, J. D., E. M. Lown and O. P. Strausz. Structural units of Athabasca asphaltene: The aromatics with a linear carbon framework. *Energy & Fuels* **1991**, 5, 445-453.
- Prins, R. Catalytic Hydrodenitrogenation. *Advances in Catalysis* **2001**, 46.
- Prins, R., M. Jian and M. Flechsenhar. Mechanism and kinetics of hydrodenitrogenation. *Polyhedron* **1997**, 16(18), 3235-3246.
- Pruden, B. B., J. M. Denis and G. Muir (1989). Upgrading of Cold Lake heavy oil in the CANMET hydrocracking demonstration plant. 4th UNITAR/UNDP Conference on Heavy Crude Tar Sands, Edmonton AB.
- Qian, K., K. E. Edwards, M. Siskin, W. N. Olmstead, A. S. Mennito, G. J. Dechert and N. E. Hoosain. Desorption and ionization of heavy petroleum molecules and measurement of molecular weight distributions. *Energy & Fuels* **2007**, 12.
- Richardson, S. M. and M. R. Gray. Enhancement of Residue Hydroprocessing Catalysts by Doping with Alkali Metals. *Energy & Fuels* **1997**, 11, 1119-1126.
- Satterfield, C. N. and S. H. Yang. Catalytic Hydrodenitrogenation of Quinoline in A Trickle-Bed reactor. Comparison with Vapor Phase Reaction. . *Ind. Eng. Chem. Process Des. Dev.* **1984**, 23, 11-19.
- Savage, P. E., G. E. Jacobs and M. Javanmardian. Autocatalysis and aryl alkyl bond cleavage in 1-dodecylpyrene pyrolysis. *Ind. Eng. Chem. Res.* **1989**, 28, 645-653.

- Shabtai, J., L. Veluswamy and A. G. Oblad. Steric Effects in Phenanthren and Pyrene Hydrogenation Catalyzed by Sulfided Ni-W / Al<sub>2</sub>O<sub>3</sub>. *Prepr. Pap. - Am. Chem. Soc., Div. Fuel Chem.* **1978**, 23, 114-118.
- Shabtai, J., L. Veluswamy and A. G. Oblad. Steric Effects in the Hydrogenation-Hydrodenitrogenation of Isomeric Benzoquinolines Catalyzed by Sulfided Ni-W/Al<sub>2</sub>O<sub>3</sub>. *Prepr. Pap. - Am. Chem. Soc., Div. Fuel Chem.* **1978**, 23, 114-118.
- Shabtai, J., G. J. C. Yeh, C. Russell and A. G. Oblad. Fundamental Hydrodenitrogenation Studies of Polycyclic N-Containing Compounds Found in Heavy Oils. 1. 5,6-Benzoquinoline. *Ind. Eng. Chem. Res.* **1989**, 28, 139-146.
- Sheremata, J. M., M. R. Gray, H. D. Dettman and W. C. McCaffrey. Quantitative Molecular Representation and Sequential Optimization of Athabasca Asphaltenes. *Energy & Fuels* **2004**, 18, 1377-1384.
- Shin, S., K. Sakanishi, I. Mochida, D. A. Grudoski and J. H. Shinn. Identification and Reactivity of Nitrogen Molecular Species in Gas Oils. *Energy & Fuels* **2000**, 14, 539-544.
- Stern, E. W. *Journal of Catalysis* **1979**, 57, 39.
- Strausz, O. P. and E. M. Lown (2003). The Chemistry of Alberta Oil Sands, Bitumens, and Heavy Oils. AERI, Calgary, AB.
- Szymanska, A., M. Lewandowski, C. Sayang and G. Djega-Mariadassou. Kinetic study of the hydrodenitrogenation of carbazole over bulk molybdenum carbide. *Journal of Catalysis* **2003**, 218(1), 24-31.
- Topsøe, H., B. S. Clausen and F. E. Massoth (1996). Hydrotreating Catalysis, Science and Technology. Berlin, Springer.

- Topsøe, H., B. S. Clausen, N.-Y. Topsøe and P. Zeuthen (1989). Progress in the Design of Hydrotreating Catalysts Based on Fundamental Molecular Insight. Conference on Catalysts in Petroleum Refining, Kuwait.
- Vit, Z. and J. Cinibulk. Effect of H<sub>2</sub>S on pyridine HDN over Ir, Mo and Ir-Mo/Al<sub>2</sub>O<sub>3</sub> sulfide catalysts. *Reaction Kinetics and Catalysis Letters* **2002**, 77(1), 43-49.
- Vivier, L., S. Kasztelan and G. Perot. *Bull. Soc. Chim. Belg.* **1991**, 100, 801.
- Wiwel, P., P. Knudsen, P. Zeuthen and D. Whitehurst. *Ind. Eng. Chem. Res.* **2000**, 39, 533.
- Ying, Z.-S., B. Gevert and J.-E. Otterstedt. Large-Pore Catalysts for Hydroprocessing of Residual Oils. *Ind. Eng. Chem. Res.* **1995**, 34(5), 1566-1571.
- Zawadski, R., S. S. Shih, E. Reiff, J. R. Katzer and H. Kwart (1982). Kinetics and Mechanism of Catalytic Hydroprocessing of Components of Coal-Derived Liquids: Tenth and Eleventh Quarterly Reports for the Period August 16, 1981 to February 15, 1982 D. o. Energy. Washington, DC, Office of Fossil Energy.

# CHAPTER 2

---

## Experimental Materials and Methods

### 2.1 Chemicals

A list of all the chemicals used in this study is presented in Table 2-1.

#### 2.1.1 Model Compounds

Two families comprised of three model compounds each were investigated under hydrotreatment conditions. The six model compounds categorized by their respective families are listed in Table 2-2. The pyrene/pyridine family of model compounds consisted of two pyrene groups

linked together by ethyl carbon bridges with a centre pyridine ring. The names of the model compound chemical structures for the pyrene/pyridine family, listed in Table 2-2, are abbreviated in the following manner:

- pyrene is abbreviated as P;
- the numerals preceding pyridine indicates the location of the two carbon linkages and substituents on the centre ring.

For example, P-2,6-pyridine-P refers to a compound with pyridine as the centre ring with two carbon-carbon bridges with pyrene at the ends, attached to the pyridine ring at the 2- and 6- positions.

The cholestane family of model compounds features a cholestane group fused to a 5,6-benzoquinoline structure with other various functional groups attached onto the heteroatomic ring. The cholestane family names for the chemical structures are abbreviated by indicating the functional group attached at the 2- position on the benzoquinoline structure of the model compounds by following cholestane with a hyphen in between. For example, cholestane-phenyl-*n*-butyl refers to a straight butane chain affixed to a phenyl ring, which is connected to the benzoquinoline structure of the model compound at the 2- position.

### 2.1.2 Catalyst

The catalyst used in this study was a commercially available Shell S424 Ni-Mo/ $\gamma$ -Al<sub>2</sub>O<sub>3</sub> hydrotreating catalyst. It contained approximately 2 – 4 wt % Ni and 12 – 15 wt % Mo. The estimated pore volume for this catalyst was 0.39 mL/g. The surface area was measured as 158 m<sup>2</sup>/g and the bulk density was 0.75 g/mL (Ying et al., 1995).

The tri-lobed catalyst, approx. 3 mm in length, was ground by mortar and pestle into a powder and passed through a Fisher Scientific No. 25 710  $\mu$ m sieve. The larger particles were discarded; therefore, no catalyst particle size was larger than 710  $\mu$ m.

**Table 2-1** List of the chemicals used

<b>Chemical</b>	<b>Manufacturer</b>	<b>Purity (%) and/or Grade</b>
1,2,3,4-tetrahydronaphthalene	Sigma Aldrich Co.	99
1,2,3,4-tetrahydroquinoline	Sigma Aldrich Co.	98
2,4,5,6-tetrachloro- <i>m</i> -xylene	Supelco Analytical	97.5
Benzo[ <i>a</i> ]pyrene	Sigma Aldrich Co.	N/A
Carbon disulfide	Fisher Scientific	Certified Grade
<i>Gas Cylinders</i>		
Hydrogen	PRAXAIR Canada Inc.	Ultra High Purity, 5.0
Nitrogen	PRAXAIR Canada Inc.	Ultra High Purity, 5.0
<i>HCCA Matrix</i>		
Acetonitrile	N/A	N/A
Trifluoroacetic acid	N/A	N/A
Water	N/A	N/A
$\alpha$ -cyano-4-hydroxycinnamic acid	Fluka	99, HPLC Grade
Methanol	Fisher Scientific	HPLC Grade
Methylene chloride	Fisher Scientific	HPLC Grade
Never Seez	Bostik, NSBT-8	Regular Grade
Phenanthrene	Sigma Chemical Co.	>96, HPLC Grade
Pyrene	Aldrich Chemical Company Inc.	98
Quinoline	Aldrich Chemistry	98, Reagent Grade
Sodium Hydroxide	Fisher Scientific	1N Solution
Toluene	Fisher Scientific	Certified ACS Grade

*N/A=not available*

**Table 2-2** List of model compounds investigated

Model Compound	Molecular Structure	Molecular Weight (g/mol)
<i>Pyrene/pyridine Family</i>		
pyrene-3,5-pyridine-pyrene ( <i>P-3,5-pyridine-P</i> )		535.68
pyrene-2,6-pyridine-pyrene ( <i>P-2,6-pyridine-P</i> )		535.68
pyrene-3-methyl-2,5-pyridine-pyrene ( <i>P-3-methyl-2,5-pyridine-P</i> )		549.25
<i>Cholestane Family</i>		
cholestane-phenyl		597.91
cholestane- <i>n</i> -butyl-phenyl		654.02
cholestane-bibenzyl		702.06

## 2.2 Experimental Equipment

The following sections list the equipment and their specifications used in this study.

### 2.2.1 Micro Batch Reactor

The schematic of the micro batch reactor, <1 mL in volume, used in this study is illustrated in Figure 2-1. This micro batch reactor design is a similar but smaller version of a laboratory reactor used previously in experiments studying hydroconversion (Richardson and Gray, 1997). The smaller micro reactor was chosen over the larger one for catalytic hydrogenation experiments because of the small quantity of feed used. The micro batch reactor consisted of a 6.35 mm (1/4") outer-diameter (OD) stainless steel tube, 5 cm (2") in length, which was joined and capped with Swagelok fittings. The bottom of the reactor was a Swagelok stainless steel end cap which sealed the bottom of the reactor. The top of the reactor was a 1/4" x 1/16" Swagelok reducing union. The neck of the reactor protruding from the 1/4" x 1/16" reducing union at the top of the reactor was a 1.6 mm OD (1/16") stainless steel tube, 8.26 cm (3/4") in length, which was connected to a 1/8" x 1/16" reducing union at the other end. The connection to both unions at the ends of the neck was made with ferrules fused to the 1.6 mm tube to seal the fittings.

The 1/8" x 1/16" reducing union at the top of the reactor neck was then affixed to a Swagelok Severe-Service Union-Bonnet Needle Valve. This valve allowed for operation at temperatures up to 648 °C and working pressures up to 29.4 MPa at 400 °C. The 1/8" male connector mouth of the valve was connected to a 1/8" female connector used to connect to the hydrogen gas cylinder. Not shown in Figure 2-1 is a relatively large stainless steel sleeve attached to the valve, which allowed the reactor to attach to a rod used to immerse the reactor in the sand bath. The micro batch reactors were assembled by the author, whereas,

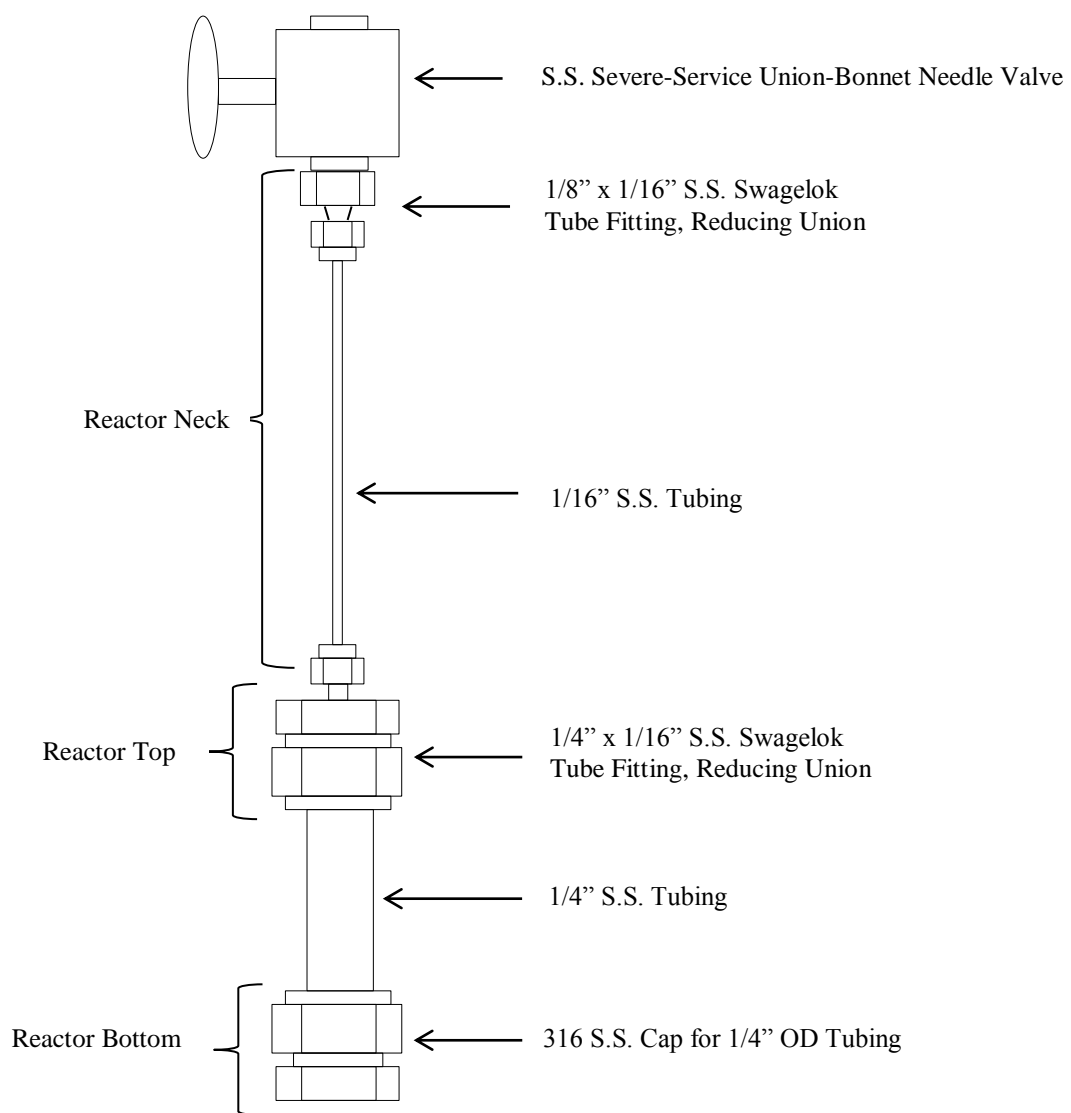


**Figure 2-1** Schematic of the micro batch reactor

the sleeve was custom built for the micro reactor by University of Alberta Chemical and Materials Engineering Department Machine Shop.

A larger batch reactor, circa 13 mL in volume, was also constructed with Swagelok parts and was assembled by the Chemical and Materials Engineering

Department Machine Shop. The same severe condition valve used in the micro batch reactor was also used for this larger reactor. The schematic and materials are the same as shown in Figure 2-1, except for larger dimensions. The reactor body was made of 3/4" stainless steel tube, 1/16" thick and 5 cm long, with a 3/4" end cap for a bottom, and a 3/4" x 1/8" reducing union for a top. The neck was constructed out of 1/8" stainless steel tube, approx. 7 cm long, with an 1/8" x 1/8" fitting at the end, which connected to the severe service valve. This larger batch reactor was used in the presulfidation of the catalyst, where a larger reactor volume was required.

### **2.2.2 Sand Bath**

The sand bath used to heat the micro reactor in the experiments for this study was a Tecam Fluidized Sand Bath Model No. SBS – 4. A picture of the sand bath set-up is shown in Figure 2-2. The sand bath was filled with approximately 20 cm of silica sand. Air was sparged through the sand near the bottom of the sand bath by a distributor. The air flow to the sand bath was regulated by a needle valve and measured by a Gilmont D1703 rotameter. Since the air flow controlled the heat transfer rate from the heating element of the sand bath, a constant setting of 35 % measured by the rotameter was used to ensure that the heat transfer rate remained constant throughout the experiments. An ALL Temperature Sensors thermocouple measured the temperature of the sand bath at approximately the mid-point along the sand bath. An OMRON E5CK controller maintained the sand bath temperature at the selected set point value. A rotating cam powered by a motor was mounted above the sand bath. Reactors were attached to a rod, which could be immersed in the sand bath. To immerse the rod, the upper arm of the rod was placed onto the cam and the motor switched on, which raised and lowered the rod. The reactor was raised and lowered a total of 3 cm at a frequency of 3 Hz. This reciprocating motion provided mixing within the micro reactors. A welded guide kept the rod centred within the sand bath.

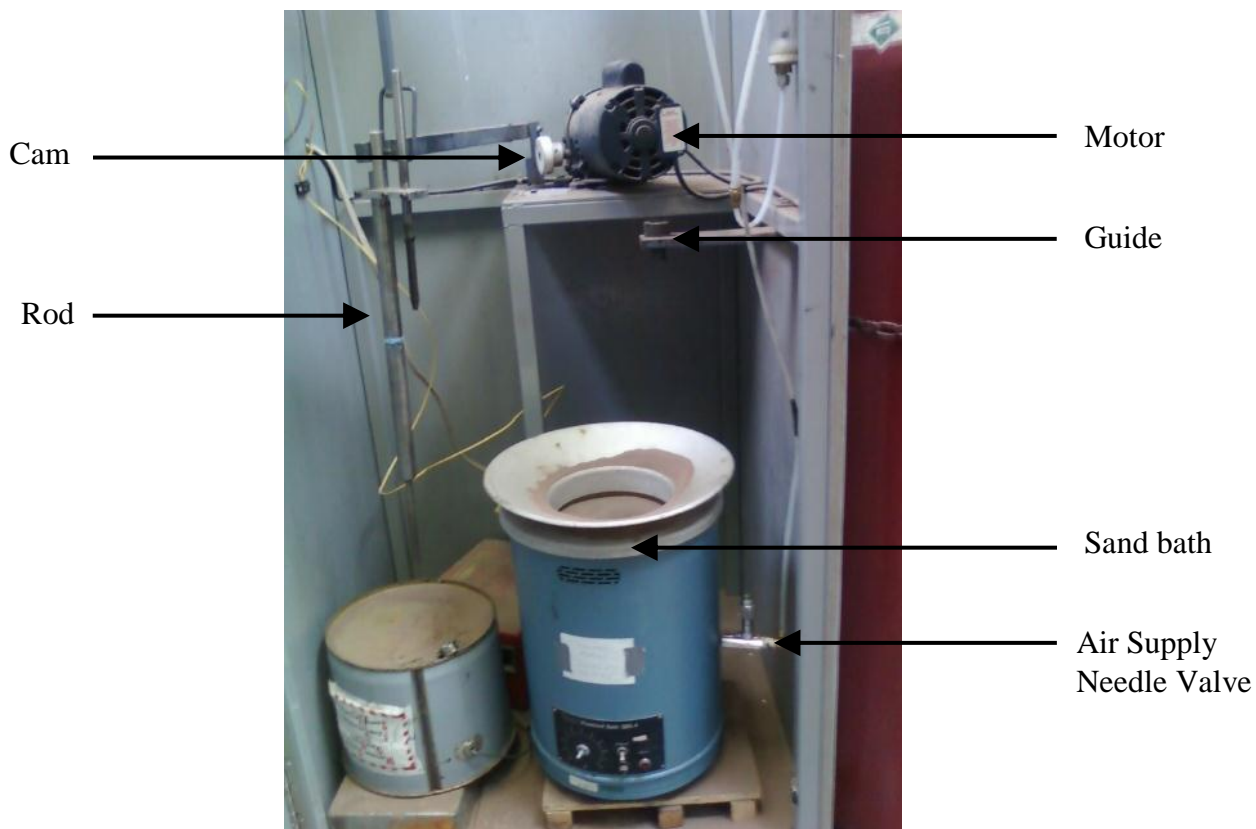


**Figure 2-2** Image of the sand bath with supporting equipment

### 2.2.3 Glove Box

A glove box was used in this study to provide a reliable nitrogen atmosphere and therefore avoid oxidation and subsequent deactivation of the catalyst. A Vacuum Atmospheres Co. NEXUS glove box used high purity nitrogen to maintain an anaerobic environment, i.e. <0.3 ppm of oxygen. Two sealed chambers, one larger and one smaller, allowed laboratory equipment to be moved inside and outside the glove box. Pressure detectors and a pump regulated the internal pressure, rarely exceeding 10 in. of H<sub>2</sub>O gauge. The procedure for moving laboratory equipment into the glove box was as follows:

- laboratory equipment was placed inside the loading chamber,
- the vacuum pump valve was opened,

- the pump vacated the chamber until a pressure gauge read circa -27 in. Hg, which took about 2 – 4 min,
- then the vacuum pump valve was closed and the valve connected to the N<sub>2</sub> cylinder was opened filling the chamber to atmospheric pressure,
- the valve to the N<sub>2</sub> cylinder was closed,
- from within the glove box the seal to the chamber was opened and the contents removed.

Removing material from inside the glove box followed the same procedure, except it began within the glove box and ended with removing the contents from the loading chamber into the lab.

#### **2.2.4 High Performance Liquid Chromatograph**

Measurement of the product model compound concentrations after a reaction had taken place was carried out by an Agilent Technologies 1200 Series High Performance Liquid Chromatograph (HPLC). The HPLC used a Zorbax Eclipse PAH column of 4.6 x 150 mm with a C18 phase of 3.5 µm particles.

The mobile phase consisted of 65 – 85% methanol and 15 – 35% methylene chloride. The temperature of the mobile phase was controlled by the instrument and was set to 23 °C. The mobile phase flow was regulated by a pump at constant flow; therefore the pressure fluctuated typically between 1 – 2 bar from steady state operation. The instrument stopped operation if a maximum pressure delivered by the pump of 400 bar was surpassed.

Table 2-3 shows the mobile phase composition and flow rate profile, either constant flow or a flow controller program for each sample analyzed. The flow controller program listed in Table 2-3, is presented in Table 2-4. This flow program allowed for good resolution during the retention times corresponding to product and parent peaks and for detection of the internal standard, which had a longer retention time, in a reasonable amount of time.

The injection of samples was automated by the instrument and was set to 1  $\mu$ L injection volumes, with a sample draw depth of -2.5 mm. The ultraviolet (UV) detector used to produce the chromatograms, was set record at two wavelengths, 239 nm and 270 nm, for each sample.

**Table 2-3** Mobile phase composition and flow profile for each sample analyzed

Sample	Mobile Phase Composition (%)		Flow Profile
	<i>CH<sub>3</sub>OH</i>	<i>CH<sub>2</sub>Cl<sub>2</sub></i>	
P-2,6-pyridne-P	65	35	Constant flow, 0.750 mL/min
P-3,5-pyridne-P	70	30	Flow controller program
P-3-methyl-2,6-pyridne-P	65	35	Constant flow, 0.750 mL/min,
cholestane-phenyl	85	15	Flow controller program
cholestane-phenyl- <i>n</i> -butyl	65	35	Constant flow, 0.750 mL/min
cholestane-bibenzyl	65	35	Constant flow, 0.750 mL/min

**Table 2-4** The mobile phase flow rate controller program

Time (min)	Flow (mL/min)
0 – 5	0.500
5 – 6	0.500 – 1.000
>6	1.000

### 2.2.5 Gas Chromatograph

Analysis of the feed and product samples of most of the control experiments and for several of the catalytic reaction experiments was performed by a Thermo Scientific – Trace GC Ultra (model no. K2733B000000B0) gas chromatograph with an AI3000 Auto-injector autosampler, as well as an attached Trace DSQII – Mass Spectrometer. The GC had a Thermo TR-5 GC Capillary Column. The column length was 7 m with a 0.32 mm inner diameter and a film thickness of 0.25  $\mu\text{m}$ . The gas chromatograph used Xcalibur 2.0.7 Thermo Fisher Scientific software for operation and analysis. Three PRAXAIR cylinders of ultra-high purity: nitrogen, hydrogen and helium were fed to the GC and were delivered at 283 kPa, 441 kPa and 441 kPa, respectively. The carrier gas was helium. Two detectors were used for analysis in this study and are shown in Table 2-5. Both instrument methods used splitless flow.

The flame ionization detector (FID) was used for quantification of samples. The FID was operated at 250  $^{\circ}\text{C}$  with the following gas flows: air at 350 mL/min, hydrogen at 35 mL/min, and make-up gas at 30 mL/min. The autosampler rinsed once with methylene chloride before injection and had a draw depth at the bottom of the sample vial.

Analysis by the mass spectrometer (MS) was performed to identify product peaks, which often was followed up by GC – FID analysis to quantify the peaks. As indicated in Table 2-5, samples were injected into the GC manually. Sample volumes were drawn with a 10  $\mu\text{L}$  micro pipette, which had been rinsed three times with carbon disulfide. The sample volume was then injected into the GC inlet once the software indicated to do so.

Subsequent GC – FID analysis conducted after identification by GC – MS differed from the GC – FID instrument method only in that it used the temperature profile and acquisition time for the GC – MS method. This alteration was made so easy identification of peaks within the GC – FID spectra could be made from the corresponding GC – MS spectra.

**Table 2-5** Instrument method by detector used for GC operation

Parameter	Instrument Method	
	<i>GC – FID</i>	<i>GC – MS</i>
Sample Injection method	Autosampler	Manual injection
Sample Volume (µL)	1	1
Carrier Gas Flow (mL/min)	1.0	0.2
Acquisition Time (min)	20	34.5
Intel Temperature (°C)		
Temperature Profile		
<i>Initial Oven Temperature</i>	40 °C	35 °C
<i>Hold Time</i>	1.00 min	2.00 min
<i>1<sup>st</sup> Ramp</i>	10.0 °C/min to 230 °C	2.0 °C/min to 45 °C
<i>Hold Time</i>	-	0.00 min
<i>2<sup>nd</sup> Ramp</i>	-	10 °C/min to 320 °C

## 2.2.6 Matrix-Assisted Laser Desorption Ionization – Mass Spectrometer

The Integrated Nanosystems Research Facility at the University of Alberta graciously allowed the use of their matrix-assisted laser desorption ionization – mass spectrometer (MALDI – MS). This MALDI – MS was an Applied Biosystems/MDS SCIEX 4800 Plus MALDI TOF/TOF Analyzer. Samples to be analyzed were prepared on a 384 Opti-TOF 123 mm x 81 mm stainless steel plate by Applied Biosystems, which was then magnetically affixed to a 1016492B TES plate holder.

For the data acquisition of ions below 5 000 Da, as in the case here, the MS Reflector Positive setting was used, with the laser intensity set to approx. 3300. This particular MALDI – MS featured a tandem MS/MS mode that allowed for the fragmentation of selected precursor ions identified by normal MS operation. The settings used for MS/MS mode were the same as MALDI – MS data acquisition.

## **2.2.7 Fourier Transform Infrared Spectrometer**

The Fourier transform infrared spectroscopy performed in this study was carried out by a Thermo Scientific Nicolet 6700 FT – IR spectrometer. The instrument used a DTGS TEC detector with a KBr beam splitter which allowed for detection over a range of 600 – 4000  $\text{cm}^{-1}$ . This device used OMNIC software for operation.

## **2.3 Experimental Procedure**

### **2.3.1 Reactor Feed**

All six asphaltene model compounds were found to be fully soluble in 1,2,3,4-tetrahydronaphthalene (tetralin) at room temperature with brief sonication, less than 5 min, at a feed concentration of approximately 2.40 mg of model compound per mL tetralin. A combination of heating and sonication ensured that any undissolved particles of model compound eventually blended into a visually homogenous mixture. Tetralin was chosen as a solvent for these experiments because of its ability to maintain a liquid phase at experimental conditions, 370 °C and 17.9 MPa. Reactor feed was prepared in batches of sufficient amount to perform 3 experiments, i.e. circa 3.60 mg of model compound in 1.5 mL of tetralin, and stored in a screw top vial (~2 mL) in a drawer at room temperature until the experiment was performed. No more than one batch at a time was prepared and stored in this way. Catalytic hydrogenation experiments performed with pyrene feed were prepared in the same way and concentration as the asphaltene model compounds.

Feeds for control experiments were prepared in the same fashion with the following exceptions. For the control experiments with phenanthrene and quinoline feeds, solutions of 1 wt % of compound in tetralin were prepared. The calculations to achieve the weight of compound needed to obtain 1 wt % assumed

a density for tetralin of 0.970 g/mL. Both compounds were fully miscible at these concentrations and formed visibly homogenous solutions. Generally, batches of feed sufficient for 3 experiments were prepared at one time, i.e. 1.5 mL of solution.

### **2.3.2 Catalyst Presulfidation**

In order to activate the crushed and sieved unsulfided fresh catalyst a presulfidation procedure was carried out. The larger batch reactor (~13 mL), instead of the micro batch reactor (<1 mL), was used for this catalyst presulfidation procedure. The valve and sleeve were the same ones used in the micro batch reactor. Approximately, 1 g of catalyst was loaded into the batch reactor, with 2 stainless steel mixing balls 4 mm in diameter. Carbon disulphide was loaded into the reactor in the amount of circa 1.84 g. Sufficient hydrogen was then loaded into the reactor to achieve a pressure of 18.5 MPa at the reaction temperature of 350 °C. The batch reactor was then immersed in the sand bath at 350 °C for 2 h.

After the reaction was complete, the reactor was removed and quenched with water shortly after. The product gas was then released slowly, over about an hour, into a scrubbing apparatus which consisted of a 1/16" stainless steel tube connected to the valve opening by 1/8" x 1/16" reducing union. The open end of the tube was submerged in a caustic wash of sodium hydroxide. The product gas was checked for H<sub>2</sub>S with Sigma-Aldrich Hydrogen Sulfide Test Strips, which confirmed the presence of H<sub>2</sub>S. The product sulfided catalyst was then recovered from the reactor by rinsing with toluene solvent over a metal fabric mesh to filter out the catalyst. The catalyst was then dried in a vacuum oven, under vacuum at 80 °C for 30 min.

This entire process was repeated a second time with the product catalyst as the feed, hence the catalyst was recycled. This recycle presulfidation was carried out in the same manner just described except for the catalyst amount fed was lower due to losses, circa 0.92 g. The final product catalyst was visibly black

throughout the catalyst particles and its activity was confirmed by control experiments.

### **2.3.3 Reactor Loading**

Feed was added to the micro reactor using the following procedure. The micro reactor with the end cap tightly on and the reducing union at the top of the reactor unattached was moved into the glove box. Then, the bottom half of the reactor with the top opened was placed onto a scale inside the glove box. Presulfided catalyst was then added to the small opening of the reactor by using a folded aluminum foil sheet. For the first experiment of a sequential series, the amount of catalyst added was approx. 40 mg with diminishing amount thereafter due to loss of catalyst. Two small stainless steel mixing balls, 1 mm in diameter, were then added to the reactor to promote mixing. Then, the feed was added to the reactor, circa 0.40 g, by pipette. The typical error for loading this amount of feed was  $\pm 0.02$  g. A small amount of CS<sub>2</sub> was added to the reactor, 10  $\mu$ L, by a 50  $\mu$ L syringe to ensure the catalyst remained sulfided. The syringe was rinsed at least two times with CS<sub>2</sub> before injection into the reactor. With the valve closed, the top half of the reactor was fastened to the bottom half by hand tightening the reducing union fitting.

### **2.3.4 Reactor Sealing and Hydrogen Pressurization**

After the reactor was successfully loaded with feed and hand tightened the reactor was removed from the glove box. The top of the reactor was then loosened, but not opened, and the female nut lifted up so Never Seez sealant could be applied to the threading of the reactor top. Never Seez promoted a more effective seal, helping to prevent leaks, and made the reactor easier to open after reaction. The reactor was then sealed by tightening the top of the reactor with a bench vice and wrench.

After the reactor was sealed, the reactor was connected to the H<sub>2</sub> cylinder with the valve apparatus shown in Figure 2-3. The reactor was pressurized by opening the H<sub>2</sub> cylinder valve (Valve 1), H<sub>2</sub> supply valve (Valve 2) and the reactor valve (Valve 4). Once pressurized, a leak detection fluid, usually water or a mixture of water and Snoop, was applied to the reactor fittings to check for leaks. If no leaks were suspected (absence of bubbles formed by the fluid), the reactor valve was closed, the cylinder valve closed, the purge valve (Valve 3) opened, and then the reactor valve opened (Valve 4). Subsequently, H<sub>2</sub> would vent from the reactor. The sequence was reversed to fill the reactor with H<sub>2</sub>. Once the filling/purge sequence was started Valve 1 was left open. The reactor valve was always opened and closed first to prevent back flow of air from entering the reactor from the purge line. This filling and purge cycle was repeated three times. Then, the reactor and cylinder valves were closed and the reactor was disconnected. The reactor was then observed briefly for leaks before being immersed in the sand bath. If at any time in the above procedure a leak was detected, the reactor was disconnected from the H<sub>2</sub> cylinder and either the seal was tightened or loosened and Never Seez reapplied and retightened again. The H<sub>2</sub> pressurization procedure was then repeated to check the new seal. This procedure to address leaks rarely occurred more than twice. If a reactor was becoming problematic to seal, it was removed from service to insure that it did not fail to seal once feed and catalyst were inside.

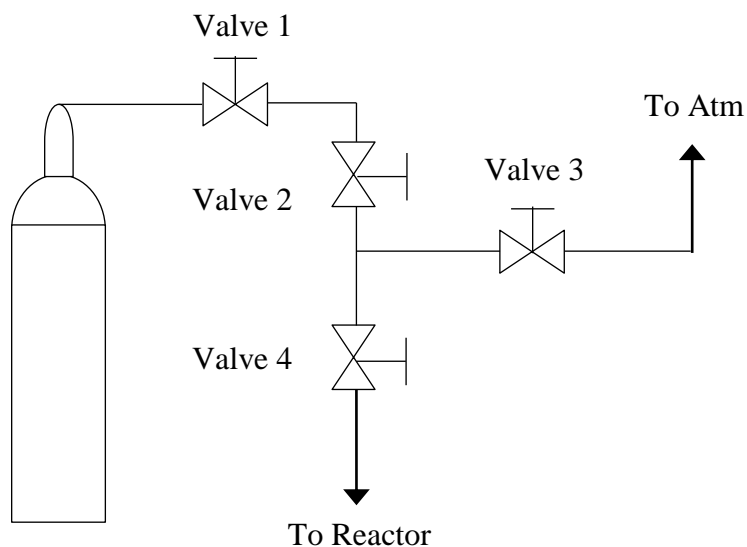


**Figure 2-3** Schematic of the hydrogen cylinder valve set-up

### 2.3.5 Reaction

After the reactor has been successfully sealed and pressurized with 8.3 Mpa of H<sub>2</sub> at room temperature, it was attached to the rod in the sand bath apparatus and immersed in the sand bath by placing the arm connected to the rod onto the cam and turning the motor on. The shaking of the reactor promoted good mixing within the interior of the reactor, and was aided by the two mixing balls.

The conditions for all the experiments performed in this study are shown in Table 2-6. The normal conditions for the experiments of this study were 370 °C for 60 min with 17.9 MPa of pressure at reaction temperature. Several control experiments were conducted at 350 °C for 20 min with 8.7 MPa of pressure at reaction temperature, one without hydrogen and one without catalyst. One thermal cracking control experiment was conducted at 370 °C for 60 min with 17.9 MPa of pressure at reaction temperature without catalyst. Note that all pressures reported in this study are estimated pressures using the ideal gas equation at state at the appropriate temperature.

Once the reaction time had elapsed, the reactor was lifted from the sand bath and left to air cool briefly. Then, the reactor was removed from the rod and quenched with water in a nearby sink. After the reactor had cooled, the product gases were purged into a fume hood.

**Table 2-6** Experimental conditions and reaction times

<b>No.</b>	<b>Experiment</b>	<b>Temperature (°C)</b>	<b>Pressure (MPa)</b>	<b>Reaction Time (min)</b>
20	Catalytic hydrogenation	370	17.9	60
1	Thermal control	370	17.9	60
	Control experiments			
2	<i>mild</i>	350	8.7	20
2	<i>normal</i>	370	17.9	60
1	<i>w/o hydrogen</i>	350	-	20
1	<i>w/o catalyst</i>	350	8.7	20

### 2.3.6 Product Recovery

Once the product gases had been vented, the reactor was placed in a bench vice and the top end of the reactor loosened, but not unsealed. The reactor was then placed inside the loading chamber to the glove box, as well as a 20 mL glass beaker and a square fabric metal mesh. With the contents of the loading chamber successfully moved inside the glove box, a lab stand was erected to hold the beaker with the square cut out of metal fabric mesh atop it.

The loosened top of the reactor was then unsealed by hand and the contents drained through the mesh and into the beaker and rinsed with solvent. Solvents used include: toluene, methylene chloride and carbon disulfide. Then, the neck of the reactor was rinsed with solvent and drained through the mesh into

the beaker. Once it was thought the all the contents of the reactor had been removed, i.e. the catalyst, two mixing balls and the product liquid, the filtered catalyst and the mesh holding it were rinsed.

The reactor and product liquid in the glass beaker were then removed from the glove box, while the catalyst to be reused in another experiment was left to dry in the glove box. The product liquid and solvent solution always had residual catalyst fines which had to be removed for the protection of analysis equipment. Therefore, a 1 mL plastic syringe and fitted filter, 0.2  $\mu\text{m}$ , were used to remove the residual catalyst. The solvent was then evaporated by mild blowing from an air hose for 5 – 10 min. The product liquid was then pipetted into a vial, usually a HPLC vial approx. 1.0 mL in volume, to be stored for later analysis.

Due to the small quantity to be recovered, circa 0.40 g, losses from pipetting the product liquid into a vial and tetralin solvent from evaporation were significant. Most of the product liquid mass was about 60 to 70% of the original feed mass. It was found that about half of the mass lost was from evaporation and the other half from losses in the syringe and filter and the pipette walls. Since only the mass of tetralin lost affected the product concentrations measured, only it was accounted for in the calculation of the conversions from the subsequent sample analysis, i.e. the solvent lost caused the final concentrations to be 15% higher than they otherwise would be.

### **2.3.7 Sample Analysis**

Once the reactions had been completed and the product liquid recovered, analysis by HPLC, MALDI – MS or GC was carried out depending on the experiment performed. The catalytic hydrogenation experiment product samples were analyzed by HPLC to determine the conversion, while MALDI – MS was used to identify product species, detect cracked products for the cholestane family, and determine a selectivity ratio for product compounds, and GC to detect and quantify cracked products for the pyrene/pyridine family.

Control experiments performed with pyrene, quinoline and phenanthrene feeds were analyzed by GC for product identification and quantification. One thermal control experiment with model compound P-3,5-pyridine-P was analyzed by GC for cracked product identification and quantification, and MALDI – MS to identify possible addition products.

### 2.3.7.1 HPLC Analysis

Product samples were analyzed by HPLC to evaluate the remaining model compound concentration and therefore measure the conversion of the model compounds after a catalytic reaction was performed. HPLC analysis was selected for conversion evaluation because these model compounds were known not to elute in GC instruments due to their relatively large size >500 Da.

All the product samples to be analyzed were undiluted except for the P-3,5-pyridine-P and cholestane-phenyl product samples, which were diluted 1:30 by volume in methylene chloride.

A benzo[*a*]pyrene internal standard was then added to the product samples. This was done by weighing circa 0.40 – 1.00 mg of benzo[*a*]pyrene on weighing paper and then dissolving the solid in the small vial containing the diluted or undiluted product sample. Typical internal standard concentrations ranged from 0.5 mg/mL to 4.5 mg/mL depending on the remaining volume of product sample.

Integration of the resulting chromatograms was performed by the Agilent software operating the HPLC. Generally, peak resolution was good and retention times consistent. Several times it was observed that the retention times of peaks shifted. However, retention times relative to the internal standard retention time remained consistent. For example, a peak may have shifted 0.5 min later than a previous analysis of the same product sample; however, the internal standard would also have shifted 0.5 min later.

Calibration curves were constructed for the calculation of the measured concentration of the analytes for pyrene-3,5-pyridine-pyrene, pyrene-3-methyl-2,5-pyridine-pyrene and cholestane-phenyl. All were linear in the signal response (area of peaks) to the quantity of model compound added. Both model compounds cholestane-bibenzyl and cholestane-phenyl-*n*-butyl had such low response in the product sample that making calibration curves was unnecessary. Detailed information on how the calibration curves and the chromatograms were obtained can be found in Appendix A. For model compound pyrene-2,6-pyridine-pyrene, an internal standard single-point calculation, which is described in detail in Appendix B, was used instead of a calibration curve because of the low supply of the model compound available.

#### **2.3.7.2 GC Analysis**

GC analysis was used to detect and quantify lighter compounds such as compounds used in control experiments and cracked products formed from reactions of asphaltene model compounds.

Product samples were diluted 1:40 by volume in carbon disulfide. This was accomplished by adding 400  $\mu\text{L}$  of  $\text{CS}_2$  to a 1.0 mL GC analyte vial. Then using a micro syringe, 10  $\mu\text{L}$  of product sample was added to the vial and mixed to form a fully miscible solution. A 2,4,5,6-tetrachloro-*m*-xylene internal standard was added to the diluted analyte solution by weighing on paper approximately 0.50 – 1.00 mg of internal standard and then dissolving it in the vial. The vial was then placed in the autosampler to be injected and analyzed by the GC.

No calibration curves were made for GC analysis because the single point method outlined in Appendix B was deemed sufficiently accurate. Integration of the peaks was carried out by Xcalibur software which also operated the instrument. This integration method required manual drawing of the base line by the user. Single-point internal standard calculations were performed using the integrated peak area of the feed and product peaks of the compound analyzed and the feed and product peaks of the internal standard.

For identification of product peaks by GC – MS, use of the library database usually identified the peak considered. However, consultation of the mass/charge ratio spectra often accompanied the database's suggestion of molecular structure to either confirm the suggestion or identify the molecular structure of the peak altogether.

### **2.3.7.3 MALDI – MS Analysis**

Analysis by MALDI – MS allowed for the identification of heavier product compounds, those >400 Da, and determine a selectivity ratio of the catalytic reaction products.

MALDI – MS/MS is a powerful mass spectrometer technique that allows for the verification of plausible product peaks in a reaction product MALDI – MS spectrum. This technique isolates ions of a single precursor (selected m/z ratio) by two polarized plates, and irradiates them with a high intensity laser, and then detects the resulting ionized fragments. Unfragmented parent ions also are detected at the appropriate mass to charge ratio.

Producing the HCCA matrix, which is used to ionize the large molecules to be analyzed, was the first step in preparation of the MALDI plate to be analyzed by the MALDI – MS instrument. The HCCA matrix was prepared by first measuring 5 – 6 mg of  $\alpha$ -cyano-4-hydroxycinnamic acid in a container. A solution of 50 vol % acetonitrile, 0.1 vol % trifluoroacetic acid with the remainder water was then added to dissolve the solid acid to achieve a concentration of 5 mg  $\alpha$ -cyano-4-hydroxycinnamic acid per mL of solution. The HCCA matrix was briefly mixed with a vortex device at ~1000 rpm and subsequently centrifuged for less than 5 min. Typically, batches of circa 1.1 mL of HCCA matrix were prepared for analysis of a single plate.

Once the HCCA matrix was prepared, 30  $\mu$ L subsamples to be placed in the wells of the MALDI – MS ionization plate were made by pipetting the product samples with matrix, in a 1:5 ratio by volume, into small containers. Typically 7 –

8 subsamples were prepared in this way and were mixed by a vortex device and centrifuged. These subsamples were not fully miscible due to the polarity of the HCCA matrix, however, good MALDI – MS spectra were still obtained. The subsamples prepared with HCCA matrix were then pipetted on the stainless steel plate in rows of 5 – 10 wells per sample, with 0.5  $\mu$ L of prepared subsample per well. The plate was then left to dry for 20 – 30 min.

The plate with the samples to be analyzed, once dry, was blown mildly across the surface with air to remove dust. Dust was also removed in this way from the metal plate holder and the loading chamber to the MALDI – MS instrument. The plate was then affixed to the plate holder and placed into the loading chamber.

The generation of MALDI – MS spectra was performed manually by directing the laser to irradiate sections of the plate with sample. The results obtained in this study are representative of the typical spectrum produced from the observance of multiple spectra from various wells of the same sample. Poor MALDI – MS spectra, i.e. lots of noise, no model compound or products detected, too little ionization, or excessive detection of matrix adducts and contaminants, were summarily discarded. MALDI – MS/MS spectra were obtained in the same fashion using the same sample plate. Further detail of MALDI – MS analysis method can be found in Appendix C.

## 2.4 References

- Kanda, W., I. Siu, J. Adjaye, A. E. Nelson and M. R. Gray. Inhibition and Deactivation of Hydrodenitrogenation (HDN) Catalysts by Narrow-Boiling Fractions of Athabasca Coker Gas Oil. *Energy & Fuels* **2003**, 18, 539-546.
- Satterfield, C. N. and S. H. Yang. Catalytic Hydrodenitrogenation of Quinoline in A Trickle-Bed reactor. Comparison with Vapor Phase Reaction. . *Ind. Eng. Chem. Process Des. Dev.* **1984**, 23, 11-19.
- Shabtai, J., L. Veluswamy and A. G. Oblad. Steric Effects in Phenanthren and Pyrene Hydrogenation Catalyzed by Sulfided Ni-W / Al<sub>2</sub>O<sub>3</sub>. *Prepr. Pap. - Am. Chem. Soc., Div. Fuel Chem.* **1978**, 23, 114-118.

# CHAPTER 3

---

## Results

### **3.1 Validation of Experimental Method**

#### **3.1.1 Reactor Heat-up Curve**

A heat-up curve was obtained to evaluate the temperature profile of the contents of the batch microreactor as illustrated in Figure 2-1. This procedure was carried out by constructing a modified microreactor with a 1/4" x 1/16" union installed in place of the end cap of the typical reactor. Then a thermocouple was inserted inside the microreactor, through the union, to approximately half way along the 2" body section of the reactor, where the temperature was observed. The reactor was then loaded with sufficient hydrogen to obtain 8 650 kPa of reactor

pressure at 350 °C, with no feed present. The reactor interior was then sealed from the outside atmosphere. The thermocouple was connected by wire to a device equipped with software to record the signal.

Figure 3-1 shows the temperature of the microreactor as a function of time. The steady state temperature was determined by the average of the plateau of the curve by inspection and was found to be 351 °C. The reactor's heating time, defined as the time required to reach 95% of the steady state temperature, was 2 min and 36 seconds. The cool down time was defined as the amount of time required to reduce the reactor interior temperature to 100 °C below the desired reaction temperature from the end of steady state operation.

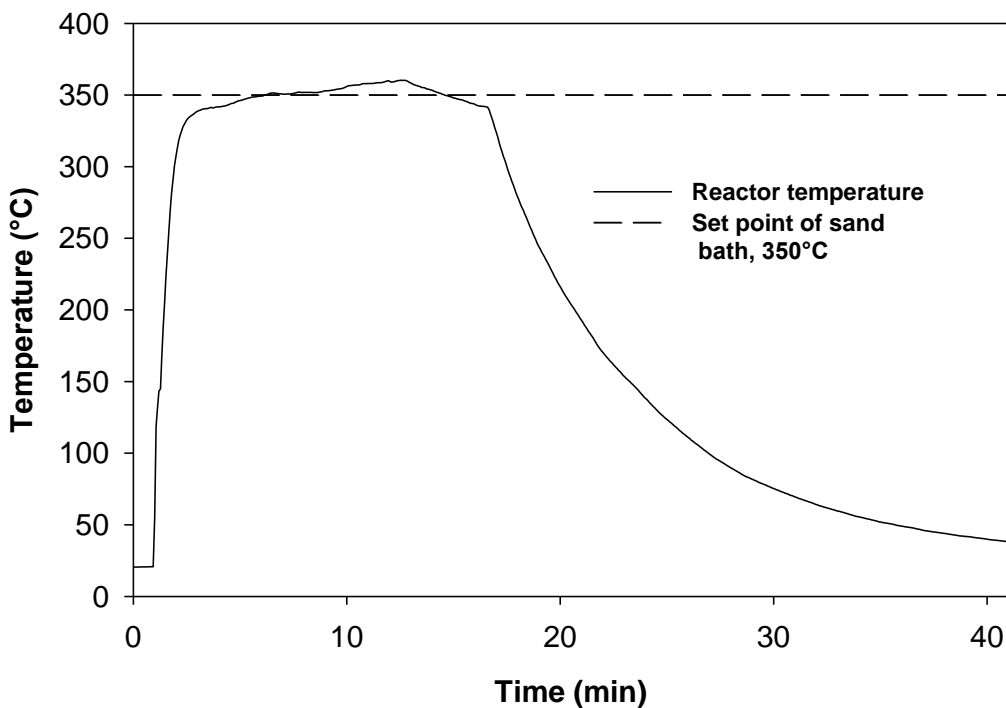


**Figure 3-1** Heat-up curve of a microreactor immersed in a sand bath at a set point of 350 °C

The cool down time is a measure of how long after the microreactor is removed from the sand bath that the reaction could possibly still take place. On this basis, the cool down time was 2 min and 36 seconds.

The sand bath temperature controller would overshoot the set point value of 350 °C, at which point the heater would turn off allowing the temperature of the sand bath to drop until the temperature fell below the set point value, turning the heater back on. During this steady state operation the temperature of the reactor varied from 340 °C to 360 °C, and therefore only deviated within 2.9% of the set point temperature at any time in operation. This variation should not have had a significant effect on the repeatability of experiments because the settings on the sand bath were the same in all cases. Although, heat up of the feed and the exothermic hydrogenation reactions were not accounted for in this experiment, both should have negligible effect on temperature profile in comparison to heating of the mass of the reactor itself, given the small quantity of feed, i.e. 0.40 g of liquid feed compared to the ~56.3 g mass of the reactor.

### **3.1.2 Repeatability of Results**

Analysis of the repeatability of results was conducted to ensure that the HPLC, MALDI – MS, and the GC data were repeatable, and also provide the error estimates involved with these techniques.

#### **3.1.2.1 Repeatability of HPLC Analysis**

A check of the repeatability of HPLC results was performed to verify the technique's ability to provide meaningful and accurate data and estimate the uncertainty. Figure 3-2 shows the calibration curve of the pyrene/pyridine family model compound P-3-methyl-2,5-pyridine-P. The calibration curve was constructed by HPLC analysis of prepared samples of P-3-methyl-2,5-pyridine-P in tetralin solvent at various replicate concentrations. The

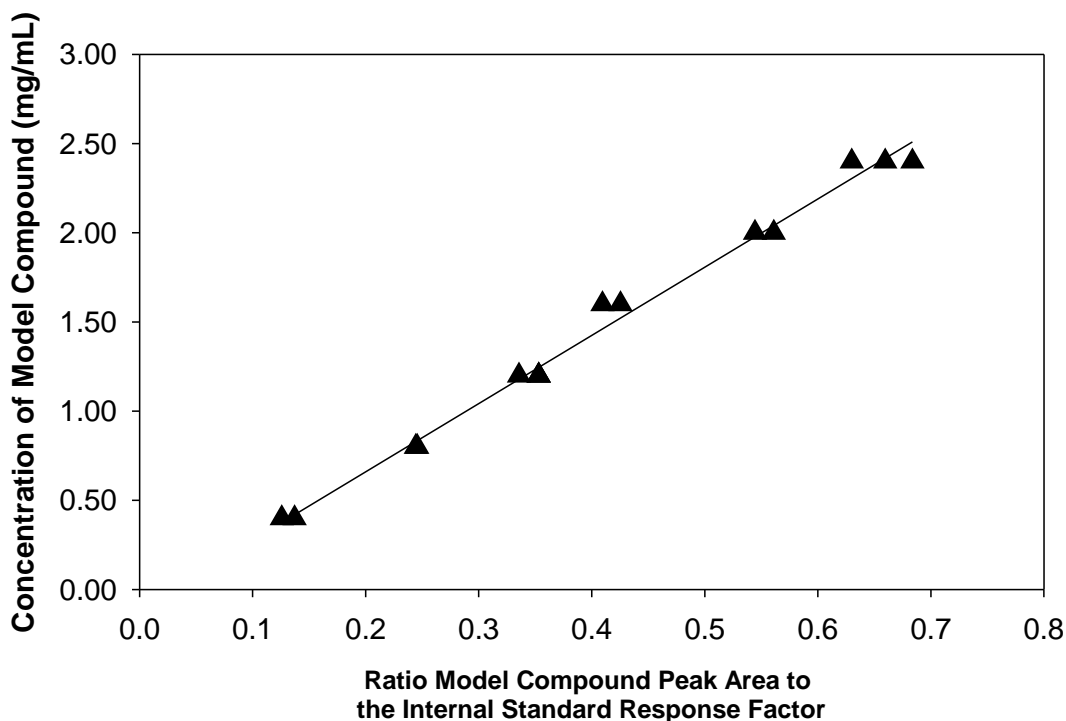


**Figure 3-2** HPLC calibration curve of model compound P-3-methyl-2,5-pyridine-P

resulting peak area of both the model compound and the internal standard benzo[*a*]pyrene was tabulated, as shown in the Appendix A, and plotted to produce Figure 3-2. Linear regression was then used for measurement of reaction product concentrations. The standard error for the measurement of the concentration of this model compound by HPLC analysis was 0.07 mg/mL. It is evident from Figure 3-2 that the quality of repeatability remains consistent throughout the replicate samples tested, especially the lower concentrations where most of the reaction product samples were evaluated. Since the HPLC analysis was deemed to be reliable and reproducible as demonstrated here most product samples were only analyzed once or twice. They were analyzed more than once if:

- there was difficulty resolving the parent model compound or internal standard peaks, or
- there was a result that differed greatly from expectations.

### **3.1.2.2 Repeatability of GC Analysis**

The repeatability of results determined by GC analysis was also explored to ensure the validity of those results. Since complete calibration curves for GC analysis were not made, a comparison of replicate signal responses for a series of analytes was carried out and is shown in Table 3-1. Therefore, Replicates 1 and 2 were at identical concentrations for each sample, while different samples had different concentrations of analyte. The average error was 3.45% and the maximum error was 7.51% of the signal response, defined as the ratio of area of analyte peak to internal standard response factor. Similar to the HPLC analysis, GC analysis was considered reliable and repeatable and therefore was typically repeated no more than twice unless results were doubtful for the same reasons as described for HPLC analysis.

**Table 3-1** GC analysis of a series of replicate samples at identical concentration

Sample	Signal Response*		Difference (%)
	Replicate 1	Replicate 2	
Pyrene feed	0.133	0.130	2.45
Quinoline feed	0.241	0.223	7.51
Quinoline reaction product	0.111	0.112	0.67
Quinoline reaction product	0.181	0.173	4.38
Phenanthrene feed	0.249	0.234	5.93
Phenanthrene reaction product	0.222	0.217	2.15
Phenanthrene reaction product	0.131	0.132	1.03

\* ratio of area of analyte peak area to internal standard response factor

### 3.1.2.3 Repeatability of MALDI – MS Analysis

Due to the nature of the MALDI – MS instrument there can be large variations in individual peak areas from spectrum to spectrum. These variations occur:

- among the prepared samples,
- among the multiple sample wells of a single plate, all of which originate from a single prepared sample,
- among the different spectra measured from the same well.

Therefore, it is important to determine the error of measurements acquired from the MALDI – MS technique to ensure the accuracy and quality of data produced. Figure 3-3 shows the ratio of a single product’s peak intensity, i.e. a product peak 6 Da larger than the parent model compound, to the parent model compound peak intensity versus cumulative reaction time. The two model compounds cholestane-phenyl and P-2,6-pyridine-P were analyzed. Each data point was evaluated as the mean of multiple measurements, no less than four, of the aforementioned ratio from different spectra of the same prepared MALDI - MS sample. The standard error was then calculated from those measurements and plotted as the errors bars in Figure 3-3.

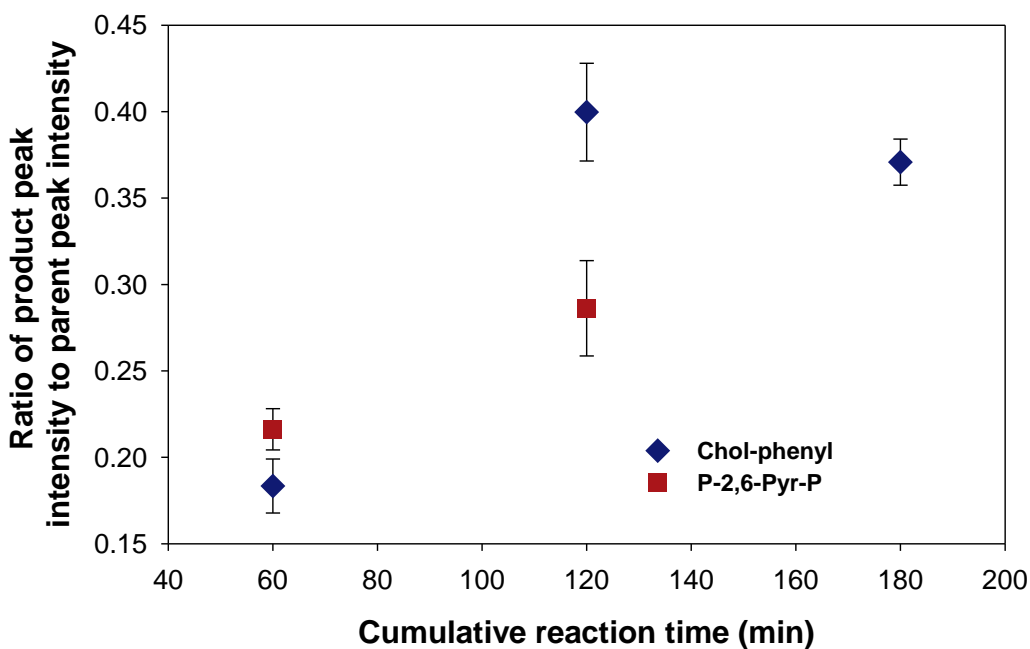


**Figure 3-3** Repeatability of MALDI measurements as a function of cumulative reaction time for model compounds cholestane-phenyl and P-2,6-pyridine-P with standard error bars ( $n \geq 4$ )

The standard error shown in Figure 3-3 demonstrates a reasonable level of repeatability for this technique considering the limitations of the MALDI instrument. The average percent error for each for each replicate sample analyzed ranged from 5.1% to 16.6%. The average percent error for all repeatability data obtained was 11.7%.

### **3.1.3 Validation of Catalytic Activity**

A series of control experiments were conducted to verify conversion of functionally similar compounds via catalytic hydrogenation, demonstrate the lack of conversion activity without catalyst or hydrogen, and to compare the extent of thermal cracking of a catalytic hydrogenation reaction to a thermal reaction.

#### **3.1.3.1 Catalytic Conversion of Control Compounds**

Experiments were performed to demonstrate that the experimental method provided sufficient catalytic hydrogenation activity by producing adequate conversions of well-known compounds. The control compounds used were phenanthrene, quinoline and pyrene. The compounds were selected because of the presence of similar chemical functional groups to the model compounds studied and because of their use in many other studies including Satterfield and Yang (1984) and Shabtai et al. (1978a).

Table 3-2 shows the conditions of reaction and conversions of two experiments conducted with quinoline. Except for the feed used, both experiments did not differ from the experimental method typically employed in this study. The feed consisted of 1 wt % quinoline in tetralin. The pressure reported is estimated using the ideal gas equation of state at reaction temperature. The catalyst was presulfided NiMo/ $\gamma$ -Al<sub>2</sub>O<sub>3</sub> that was recycled at least once from similar reactions with the same feed to avoid observed irreversible adsorption of quinoline onto the catalyst from affecting the reported conversions. The conversions were evaluated by GC – FID with tetrachloro-*m*-xylene as the internal standard. The mild

experimental conditions were conducted for comparison with similar experiments performed by Kanda et al. (2003). They reported conversion of the same feed concentration of quinoline at the same temperature and pressure, although in a different solvent, as 51% which corresponded well with the conversion observed here. The almost complete disappearance of quinoline under the normal reaction conditions used in this study shows that the chosen reaction conditions are sufficient to provide effective catalytic hydrogenation activity of an aromatic nitrogen containing species.

**Table 3-2** Conversion of quinoline at mild and normal conditions

<b>Experiment</b>	<b>Temperature (°C)</b>	<b>Time (min)</b>	<b>Pressure (kPa)</b>	<b>Catalyst: Solvent (g/L)</b>	<b>Conversion (%)</b>
Mild	350	20	8650	38.6	54
Normal	370	60	17850	89.0	>99

Conversion of phenanthrene was investigated in a similar fashion to evaluate the catalytic hydrogenation activity of an aromatic multi-ring compound without nitrogen. Table 3-3 shows the conditions and conversions of two experiments performed with phenanthrene. In these experiments, the catalyst employed was not recycled because no significant irreversible adsorption onto the catalyst surface was expected to take place. The conversions were also determined via GC – FID. The mild conditions did not provide adequate activity for vigorous catalytic hydrogenation, whereas, the normal conditions provided activity likely to produce sufficiently high conversions for the large aromatic hydrocarbons studied. Note that the predominant reaction product detected by GC – MS was

9,10- dihydrophenanthrene which was consistent with catalytic hydrogenation as the dominant reaction pathway.

**Table 3-3** Conversion of phenanthrene at mild and normal conditions

<b>Experiment</b>	<b>Temperature (°C)</b>	<b>Time (min)</b>	<b>Pressure (kPa)</b>	<b>Catalyst: Solvent (g/L)</b>	<b>Conversion (%)</b>
Mild	350	20	8650	89.2	13
Normal	370	60	17850	99.4	47

Another series of experiments was conducted with pyrene to compare with the activity obtained with phenanthrene and to ensure that the conditions chosen for this study would produce sufficient activity, especially given the significance of pyrene in the chemical structure of the pyrene/pyridine family. The experiments were carried out with the same method described in the Experimental Materials and Methods section with three sequential batch reactions. A feed of pyrene dissolved in tetralin with a concentration of 2.58 mg/mL was added to the reactor. A total of three experiments with cumulatively recycled catalyst, the first experiment having fresh catalyst, were performed to account for any possible irreversible adsorption by this larger aromatic compound. The resulting conversions and the apparent first order reaction rate constants obtained are presented in Table 3-4. The conversions were evaluated by GC – FID using tetrachloro-*m*-xylene as an internal standard. The conversion was consistently near completion for all three experiments. The apparent first order reaction rate constant reached a pseudo-steady state rate constant. Comparing these results to those of phenanthrene at normal conditions shown in Table 3-3, it is observed that pyrene exhibited significantly higher activity at the same conditions. This was expected due to the chemical structures of the two compounds, pyrene having

twice as many 9,10 carbon-carbon type bonds as phenanthrene. In summary, the normal reaction conditions provide a vigorous catalytic hydrogenation environment that has been shown to give significant conversion of compounds similar to the building blocks of the asphaltene model compounds investigated.

**Table 3-4** Pyrene conversion and apparent first order rate constant at normal conditions

<b>Experiment</b>	<b>Catalyst:Solvent (g/L)</b>	<b>Conversion (%)</b>	<b>Apparent first order reaction rate constant, k(L/ (g cat · s))</b>
<b>1</b>	103.1	95	$0.83 \times 10^{-5}$
<b>2</b>	64.2	99	$2.27 \times 10^{-5}$
<b>3</b>	41.0	96	$2.25 \times 10^{-5}$

### 3.1.3.2 Catalytic Activity without Hydrogen and without Catalyst

These experiments were conducted to ensure that catalytic hydrogenation was not occurring without catalyst, or without hydrogen. These experiments would then confirm that the catalytic hydrogenation activity observed in the previous section required the presence of catalyst and hydrogen. Both experiments were performed using the same experimental method as this study, however, at the milder conditions of 350 °C and 20 min. Table 3-5 shows the feed and reported conversion for both experiments. Note that the catalyst used in the experiment without hydrogen was fresh, non-recycled catalyst. Therefore, the 25% conversion corresponds to the typical amount of irreversible adsorption of quinoline on fresh catalyst observed and is not attributed to significant hydrogenation. Furthermore, the conversion of the ‘without hydrogen’ experiment

**Table 3-5** Conversions obtained in experiments without hydrogen and without catalyst

<b>Experiment</b>	<b>Feed</b>	<b>Pressure (kPa)</b>	<b>Catalyst: Solvent (g/L)</b>	<b>Conversion (%)</b>
w/o catalyst	1 wt % phenanthrene	8650	0	3
w/o hydrogen	1 wt % quinoline	0	96.8	25

can be cross-referenced with the similar reaction conversion shown in Table 3-2, i.e. 54%, which is more than double the value obtained here. The 3% conversion obtained in the experiment on phenanthrene without catalyst is well within experimental error of no appreciable reaction occurring. In summary, no evidence for significant hydrogenation activity was observed in these experiments without hydrogen and without catalyst.

### 3.1.3.3 Thermal Cracking of Model Compound P-3,5-pyridine-P

A thermal cracking experiment of the pyrene/pyridine family model compound P-3,5-pyridine-P was conducted to compare the extent of cracked material created thermally to that of the catalytic hydrogenation reactions investigated. A comparison of the cracking yield of P-3,5-pyridine-P after both catalytic and thermal reactions is shown Table 3-6. The experiment was carried out in the same manner and conditions as described in the Experimental Procedure section, except that no catalyst and CS<sub>2</sub> were added to the microreactor. The feed for both experiments was P-3,5-pyridine-P in tetralin. The cracked product concentration for the catalytic experiment was determined using GC – FID by quantifying the peaks attributed to pyrene, methyl-pyrene, and hydrogenated species of methyl-pyrene and pyrene, as identified by GC – MS.

**Table 3-6** The yield of cracked products after catalytic and thermal reactions of P-3,5-pyridine-P

<b>Experiment</b>	<b>Feed Concentration (mg/mL)</b>	<b>Concentration of cracked products via GC (mg/mL)</b>	<b>Concentration of cracked products via HPLC (mg/mL)</b>	<b>Conversion to cracked products (wt %)</b>
Catalytic	2.33	0.53	ND	23
Thermal	2.57	0.19	0.15	7

*ND = not detected*

Then the yield of cracked products for the catalytic experiment was calculated from the concentration of cracked products.

The cracked product concentration of the thermal cracking experiment was quantified by both GC and HPLC. The concentration of cracked products by GC was determined using the same procedure described for the catalytic experiment. The quantification of cracked products by HPLC was determined by identifying the pyrene and methyl-pyrene peaks and, with the assumption that the response factors of both peaks were the same, adding their peak areas and performing a single point internal standard calculation to determine the concentration of cracked products. The single point internal standard calculation used a HPLC calibration chromatogram of a known amount pyrene analyte with a benzo[*a*]pyrene internal standard and was carried out in the same manner described in Appendix B.

The overall disappearance of P-3,5-pyridine-P for both the catalytic and thermal reactions as measured by HPLC was comparable, i.e. >99 % and 93 %, respectively. Data from Table 3-6 show that there is good agreement between the

HPLC and GC measurement of the thermal experiment cracked products concentration, giving confidence in the accuracy of the measurement. However, there is a substantial discrepancy for the thermal experiment in Table 3-6 between the disappearance of feed model compound, 93 %, and the yield of cracked products, 7 %. This discrepancy can be accounted for by: the coke observed at the end of the thermal cracking control experiment and the formation of oligomers as products. Therefore, it is likely that the 93 % conversion of model compound represents the overall conversion of P-3,5-pyridine-P by all cracking reactions including: coke, oligomers and other addition products, and cracked products. Consequently, there is a large difference in cracking reaction conversion between the thermal and catalytic reactions, 93 % and 23 %, respectively. This difference in conversion is attributed to the suppression of thermal addition product formation and cracking reactions by catalytic hydrogenation.

The data of Figure 3-4 and Figure 3-5 compare the HPLC chromatograms of products of the catalytic and thermal reactions, respectively. Note that benzopyrene is an added internal standard and not a product peak. Evidently there are pronounced qualitative differences between these figures, especially the distribution of the product peaks formed and the magnitude of those peaks. The effect of catalytic hydrogenation on the types and variety of products produced compared to thermal cracking is significant.

This phenomenon can be explored in greater depth by inspecting the MALDI – MS spectra of the product samples of both thermal cracking and catalytic hydrogenation reactions. Figure 3-6 and Figure 3-7 compare the MALDI product sample spectra of both the catalytic hydrogenation reaction and thermal cracking reaction of the model compound P-3,5-pyridine-P, respectively. The figures demonstrate the effective suppression of addition products created by thermal cracking reactions by the hydrogenation activity of the catalyst. The product peaks and parent compound ( $m/z = 536.26$ ) that are labelled were verified by MS/MS spectra, while other unlabelled peaks are either contaminants or unverified product peaks. These figures further illustrate the formation of

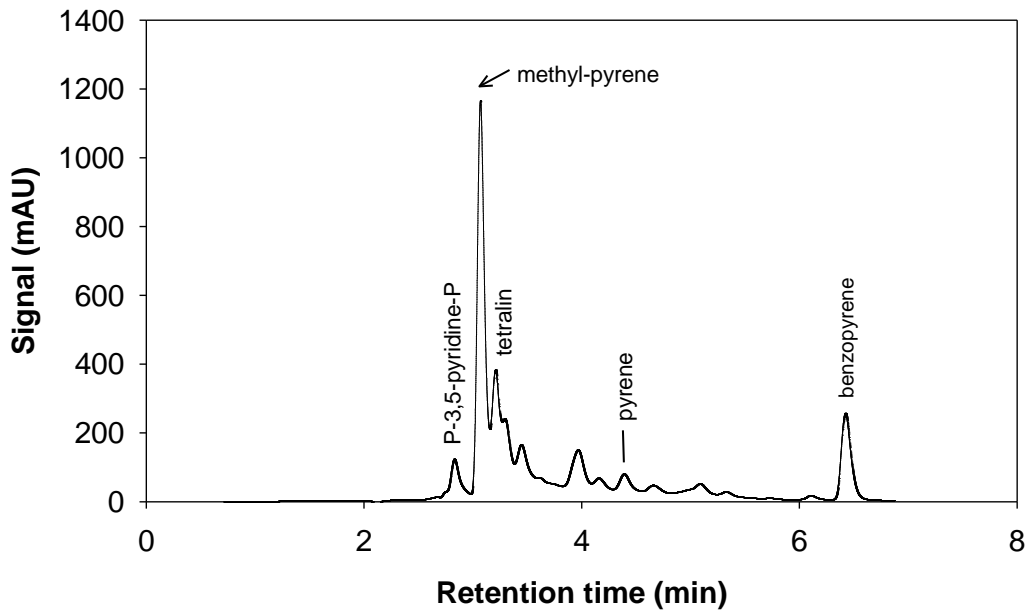


**Figure 3-4** HPLC chromatogram of P-3,5-pyridine-P products from catalytic reaction. Benzo[a]pyrene was added as an internal standard.

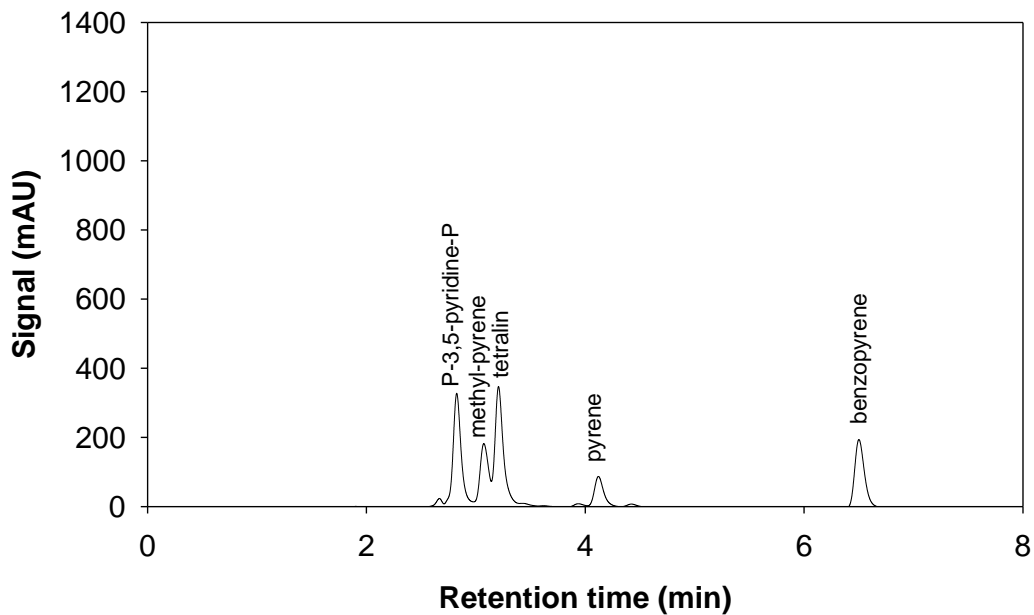


**Figure 3-5** HPLC chromatogram of P-3,5-pyridine-P products from thermal cracking reaction. Benzo[a]pyrene was added as an internal standard.

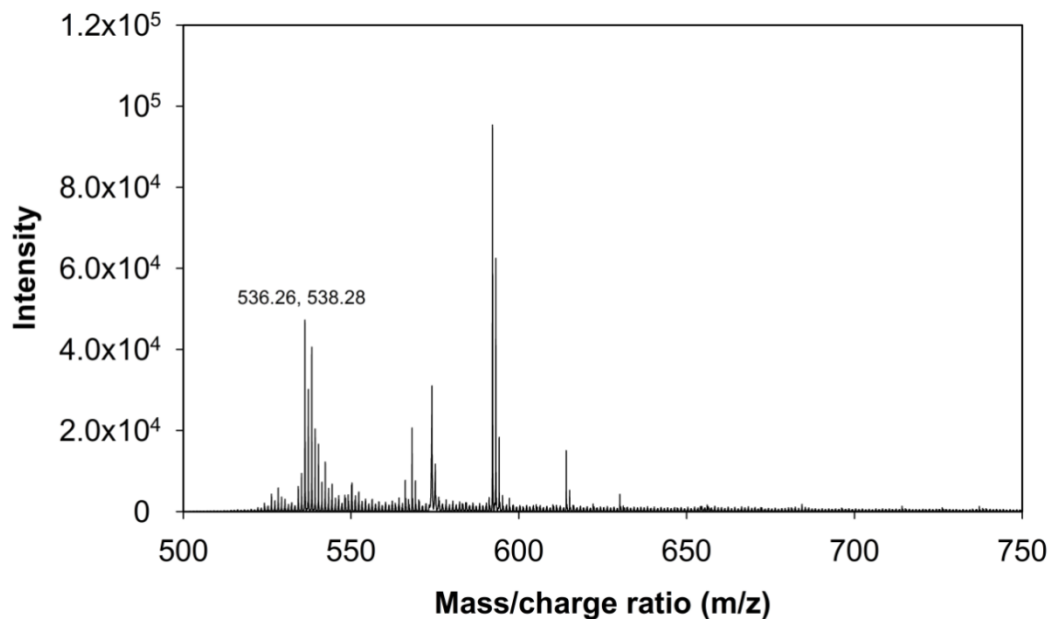


**Figure 3-6** MALDI spectrum of the catalytic hydrogenation reaction products from model compound P-3,5-pyridine-P

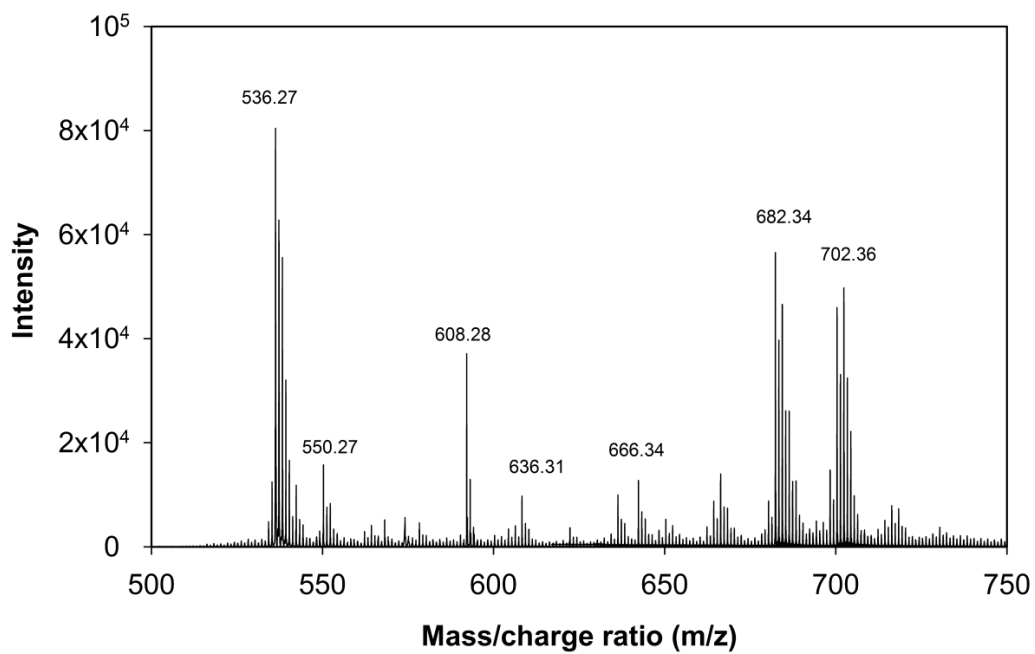


**Figure 3-7** MALDI spectrum of reaction products from thermal cracking reaction of model compound P-3,5-pyridine-P

oligomers during the thermal cracking of the pyrene/pyridine family, forming product compounds greater than 166 Da from the parent compound.

To summarize, there is good evidence for the formation of oligomers and other addition products to such a degree as to account for the discrepancy in Table 3-6 between the conversion of the parent compound and the detection of cracked products. Also, there is ample evidence that the catalytic hydrogenation reaction suppresses the formation of oligomers and addition products.

## **3.2 Model Compound Activity and Pathway Yields**

### **3.2.1 Steady State Activity in Sequential Batch Catalytic Reactions**

The accuracy and repeatability of the reaction rate constants determined from sequential batch reaction experiments is important if any conclusions concerning the objective of this study are to be made. Due to the nature of the experimental design, some catalyst was lost between each sequential batch operation and the limited supply of model compound constrained the number of successive experiments that could be performed to 3 – 4. The catalyst was recycled between each batch reaction in order to check for possible irreversible adsorption of model compound onto the surface of the catalyst, and to allow the catalyst to reach a pseudo steady state level of adsorbed reactants and reaction products. The resulting product sample concentration was then evaluated by HPLC analysis. Catalyst activity may increase or decrease during sequential batch reactions, depending on the sulfidation state of the catalyst, inhibition of the catalyst by reactants or products, and catalyst deactivation. If the catalyst is reasonably stable, and inhibition and deactivation are not severe, then the catalyst activity is expected to reach a pseudo-steady state. Calculation of the reaction rate constant from successive batch experiments is a method of deriving the reaction rate constant with the catalyst at a pseudo-steady state condition.

Assuming an apparent first order reaction occurs in a batch reactor the following equation holds:

$$\frac{dC}{dt} = -kw_{cat}C \quad (3-1)$$

where  $w_{cat}$  is the ratio of mass of catalyst to volume of liquid feed in  $g_{cat}/L$ . Then integrating and solving for conversion, the result is:

$$1 - X = \exp(-kw_{cat}t) \quad (3-2)$$

where  $k$  is the reaction rate constant with units  $L/(g_{cat}\cdot s)$ . This rate constant for a given model compound will depend on the temperature, hydrogen pressure, and catalyst activity. From the measured product sample concentrations a reaction rate constant, as defined by Equation (3-2), can be determined for each of the model compounds. Figure 3-8 to Figure 3-10 illustrate the reaction rate constant versus the cumulative reaction time for all model compounds where sufficient data was available for this analysis, i.e. 3 to 4 reliable data points. The dotted reference line denotes the reaction rate constant reported for that model compound and was calculated as the mean between the last two acceptable data points considered free of irreversible adsorption or shifts in catalyst activity in the series of sequential runs, i.e. the pseudo-steady state activity of the catalyst. Therefore, the deviation of the two points from the mean serves as the error estimate for the reaction rate constants from this analysis. A similar trend of establishing a pseudo-steady state, shown in Figure 3-8 to Figure 3-10, is demonstrated in Figure 3-3, where the signal response of single hydrogenation product within multiple MALDI – MS spectra is observed to become relatively constant after 3 sequential runs.

The reaction rate constants and the error estimates can be found in Table 3-7. Upon inspection of the relevant figures and the % Error in Table 3-7 it is clear that this analysis provides an effective estimate of reaction rate constants; the average error being 4.2%.

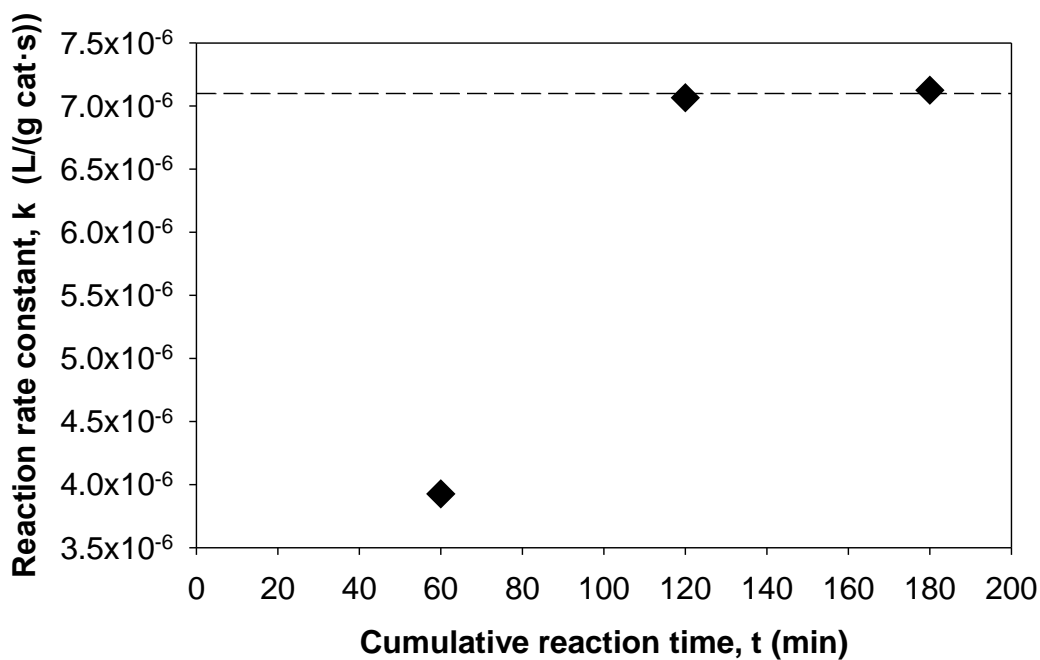


**Figure 3-8** Reaction rate constant of P-3-methyl-2,5-pyridine-P versus cumulative reaction time. The dashed line shows the pseudo-state rate constant.

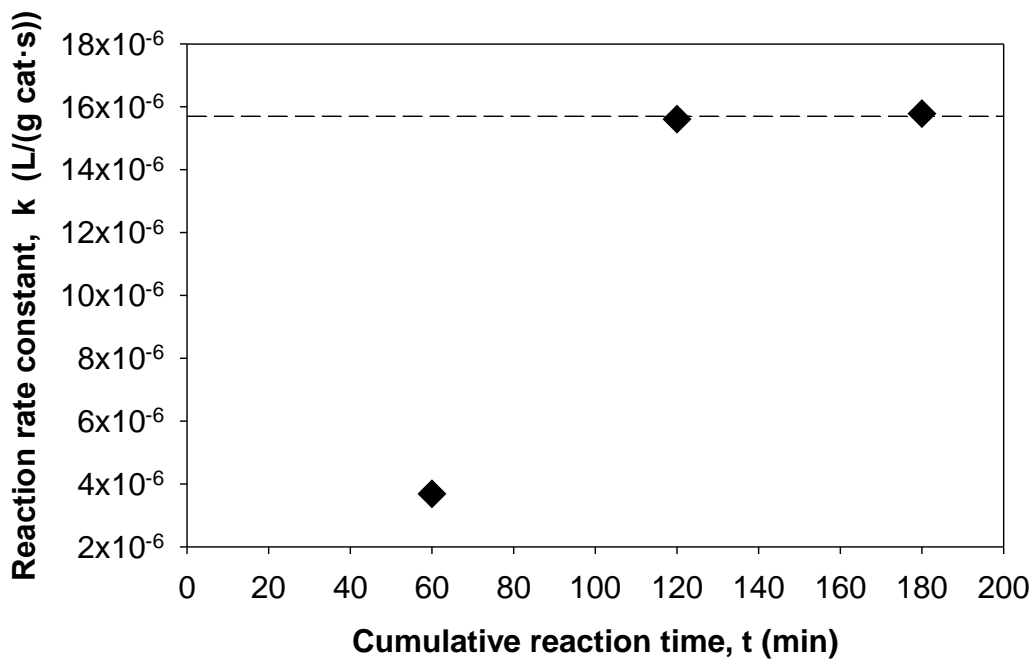


**Figure 3-9** Reaction rate constant of cholestane-phenyl versus cumulative reaction time. The dashed line shows the pseudo-state rate constant.

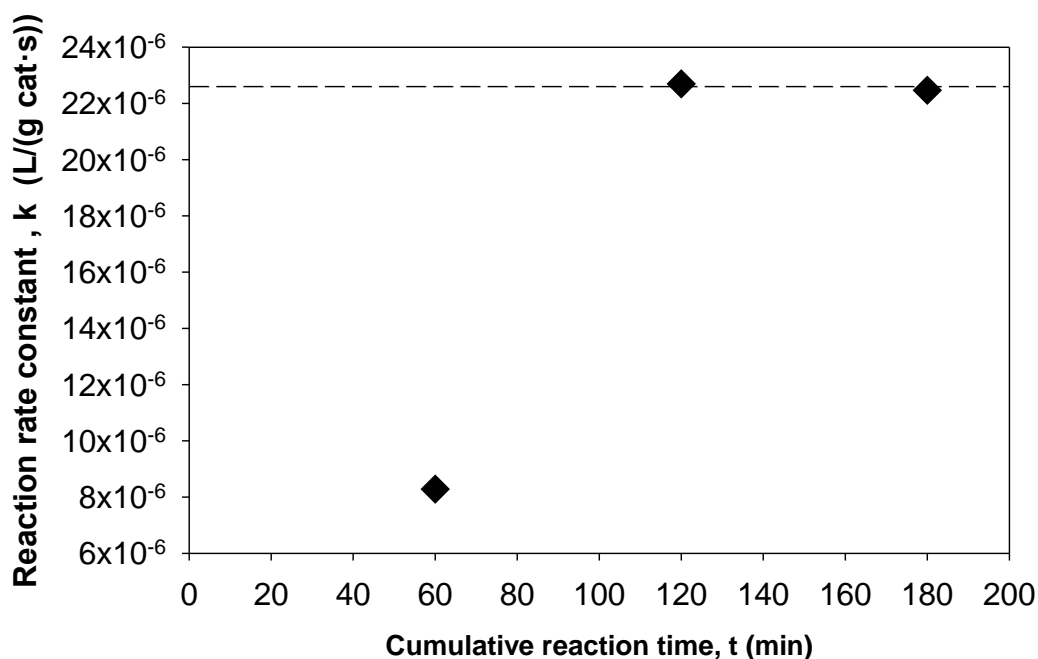


**Figure 3-10** Reaction rate constant of pyrene versus cumulative reaction time. The dashed line shows the pseudo-state rate constant.

**Table 3-7** Reaction rate constant estimates and error of estimates

<b>Model Compound</b>	<b>Reaction rate estimate, k (L/(g<sub>cat</sub>·s))</b>	<b>Uncertainty (L/(g<sub>cat</sub>·s))</b>	<b>% Uncertainty</b>
P-3-methyl-2,5-pyridine-P	7.1 × 10 <sup>-6</sup>	0.1 × 10 <sup>-6</sup>	1.4
cholestane-phenyl	15.7 × 10 <sup>-6</sup>	0.1 × 10 <sup>-6</sup>	0.6
pyrene	22.6 × 10 <sup>-6</sup>	0.1 × 10 <sup>-6</sup>	0.4

Figure 3-11 presents the reaction rate plot of P-2,6-pyridine-P, where the reaction rate constant could not be determined. The kinetics for this model compound exhibited erratic behaviour, with no discernible pseudo-steady state. Moreover, the last data point was a result from an experiment performed with appreciably less solvent feed (majority of feed was spilled before loading into micro reactor) in comparison to the catalyst loaded, resulting in a high catalyst to feed ratio of 146 g/L. The red data point shown in Figure 3-11 represents the calculated reaction rate constant if a full amount of feed had been used, i.e. a catalyst to feed ratio of 53 g/L and the conversion had remained the same. Therefore, the reaction rate constant for this compound remains inconsistent, and is only defined to be in the range of  $3 - 7 \times 10^{-6} \text{ L}/(\text{g}_{\text{cat}} \cdot \text{s})$ .

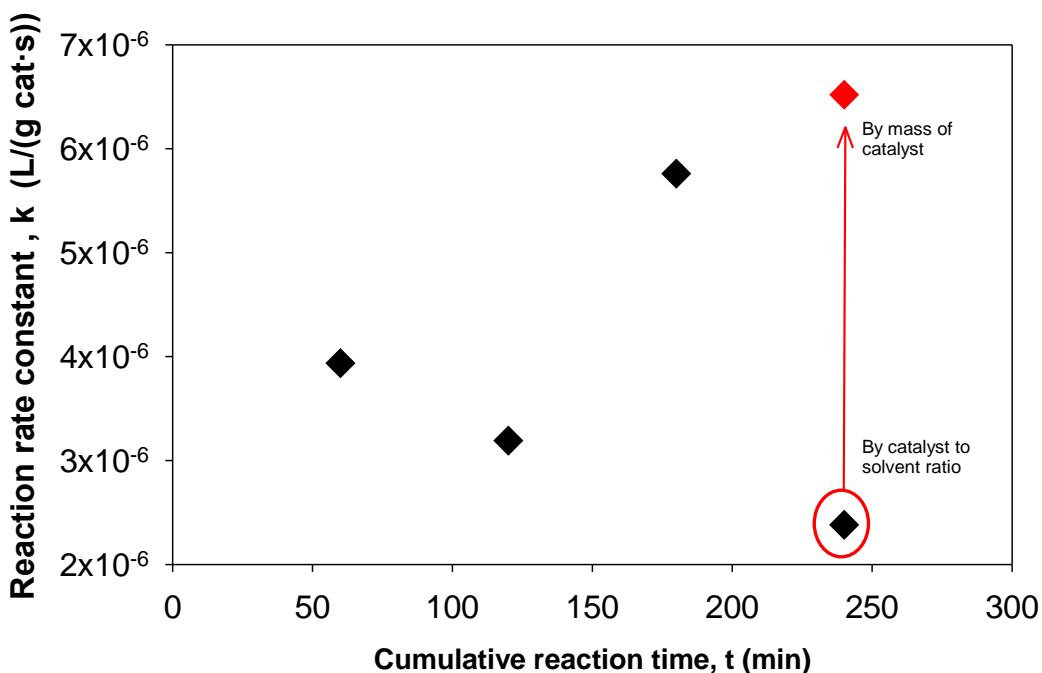


Figure 3-11 Reaction rate plot of P-2,6-pyridine-P versus cumulative reaction time

Table 3-8 summarizes the conversion by all pathways, overall apparent rate constant, and the cracking, HDN, and hydrogenation yields for all six model compounds in the two families of model compounds investigated. The conversion by all pathways reported in the Table 3-8 is determined from the average of the last two runs of a series of cumulative runs of recycled catalyst, when it is evident that they are without irreversible adsorption on the surface of the catalyst as just described. Likewise, the overall apparent reaction rate constant was then determined from the above procedure.

The yields were determined by first calculating the cracking yields from direct measurement of the concentration of expected cracked products via GC – MS and GC – FID. It is then assumed that the remaining products are hydrogenation products by simple mass balance. Therefore, from this mass balance the remaining mass attributed to hydrogenation products was divided by a selectivity ratio provided by analysis of MALDI – MS spectra of the reaction product samples into HDN and hydrogenation yields.

Table 3-8 presents the range of activity of the model compounds, reporting conversion by weight by all pathways and the reaction rate constants as defined by Equation (3-2). The cholestane family of model compounds exhibited the highest reactivity, almost more than double of all the pyrene/pyridine family of model compounds. This was unexpected given the large, relatively stable chemical structure of the cholestane compounds. The conversion and reaction rate constant was determined for the cholestane-phenyl compound but was not quantified precisely for the other two cholestane compounds because there was insufficient remaining feed concentration in the reaction product sample to be evaluated reliably. Therefore, it was inferred that the reaction rate constants for the cholestane-bibenzyl and cholestane-phenyl-*n*-butyl model compounds were larger than that of cholestane-phenyl. The pyrene/pyridine family of compounds produced a range of catalytic hydrogenation activities. The conversion and reaction rate constant are without

**Table 3-8** Pathway conversions, yields and apparent reaction rate constant for asphaltene model compounds

<b>Model Compound</b>	<b>Conversion by all pathways (%)</b>	<b>Overall apparent reaction rate constant, <math>k</math> (L/(g<sub>cat</sub>·s))</b>	<b>Yield of cracked products (wt %)</b>	<b>Yield of HDN products (wt %)</b>	<b>Yield of hydrogenation products (wt %)</b>
<i>Pyrene/pyridine family</i>					
P-2,6-pyridine-P	69 ± 2	3 – 7 x 10 <sup>-6</sup>	17	38	13
P-3-methyl-2,5-pyridine-P	84 ± 1	7.1 ± 0.1 x 10 <sup>-6</sup>	37	2	45
P-3,5-pyridine-P	>99	>9.5 x 10 <sup>-6</sup>	23	10	65
<i>Cholestane family</i>					
Cholestane-phenyl	98 ± 1	15.7 ± 0.1 x 10 <sup>-6</sup>	ND	ND	>99
Cholestane-phenyl-n-butyl	>99	>15.7 x 10 <sup>-6</sup>	ND	ND	>99
Cholestane-bibenzyl	>99	>15.7 x 10 <sup>-6</sup>	ND	ND	>99

ND = not detected

error estimates for P-3,5-pyridine-P because only the first run was evaluated correctly by HPLC analysis. This problem was due to the concentrations of the reaction product samples of the other two runs lying outside the calibration range. Therefore, only the data available, i.e. the first run, is reported in Table 3-8 as a minimum estimate.

### **3.2.2 Yield of Cracked Products**

The data of Table 3-8 shows that there was no cracking of cholestane compounds. This result was obtained from the MALDI – MS feed and product spectra of the cholestane family compounds; that is, no appreciable plausible cracked product masses of each model compound were identified in those spectra. The MALDI – MS analytical technique was used for the cholestane model compounds because the expected cracked products should have fallen into the detectable range of the instrument, i.e. greater than 400 Da. Masses that did happen to coincide with a possible cracked product were ruled out by MALDI – MS/MS spectra.

The pyrene/pyridine family cracked product yields were evaluated by GC – MS in combination with GC – FID. These techniques were chosen because the expected cracked products should have been detectable by GC in the mass range less than 300 Da. The two major cracked products identified by GC – MS for all pyrene/pyridine model compounds were pyrene and methyl-pyrene. The other cracked products identified were the hydrogenated species of these two major products. The cracked product yields were then determined by directly measuring the concentration of the identified cracked products by a single-point internal standard calculation. This assumed that methyl-pyrene and other product peaks had the same response factor as pyrene. The concentration of cracked products could then be calculated using a calibration spectrum of a known quantity of pyrene and internal standard tetrachloro-*m*-xylene. The yield of cracked products differs for each compound in this family and ranged from approximately 20 % to 40 %.

### **3.2.3 Yield of Hydrodenitrogenation and Hydrogenation Products**

The hydrodenitrogenation and hydrogenation yields shown in Table 3-8 were evaluated by first determining the cracking yields by direct measurement of the concentration from GC – FID. Then, the remaining amount of mass was attributed to HDN and hydrogenation products by mass balance. MALDI – MS product peaks were then verified as products and categorized as HDN and hydrogenation products by MALDI - MS/MS. Once achieved, modified integrated peak area spectra were constructed which allowed for the calculation of a selectivity ratio and subsequently, HDN and hydrogenation yields. This approach assumed that all products that were not cracked products were either HDN or hydrogenation products.

#### **3.2.3.1 Verification and Categorization of Hydrodenitrogenation and Hydrogenation Products by MALDI – MS/MS**

The MALDI – MS/MS spectrum of the hydrogenation product of P-3-methyl-2,5-pyridine-P ( $m/z = 554.28$ ), shown in Figure 3-12, gives an opportunity to infer the chemical structure of the product compounds. Each peak in this spectrum represents an ion fragmented from the precursor ion. Note that this technique is used to identify product fragment peaks and then distinguish or verify the product compound chemical structure, and is not used for quantitation. Three observations can be inferred from Figure 3-12. First, a plausible structure for the 553.28  $m/z$  precursor can be proposed given the fragment peaks. Secondly, the 202.05, 205.06 and 207.08  $m/z$  ions correspond to a fragmented pyrene group from the precursor ion, where 202.05  $m/z$  is not hydrogenated but 205.06  $m/z$  and 207.08  $m/z$  are. This result is evidence that the pyrene group hydrogenates. Third, the 120.07  $m/z$  fragment ion could refer to the unreacted alkyl-substituted centre heteroatomic ring after the breaking of the carbon-carbon bonds of the two bridging chains, giving evidence that the heteroaromatic ring does not

preferentially hydrogenate. Similarly, the 334.13  $m/z$  and 336.13  $m/z$  fragment ions are assigned to the remaining compound after the scission of one carbon-carbon link and loss of a pyrene group, with the other pyrene group either unreacted ( $m/z = 334.13$ ) or hydrogenated ( $m/z = 336.13$ ).

Figure 3-13 shows the MALDI – MS/MS spectrum of P-2,6-pyridine-P hydrogenation product precursor ion  $m/z = 538.19$ . Highlighted are the fragment ions corresponding to a pyrene,  $m/z = 203.9$ , and the hydrogenated pyrene group,  $m/z = 205.09, 207.09$  from the precursor ion  $m/z = 538.19$ . The precursor ion is considered to be a singly hydrogenated parent compound. This analysis allows us to determine the location of hydrogen addition onto the parent molecule. Figure 3-14 shows the MALDI – MS/MS spectrum of P-3,5-pyridine-P hydrogenation product precursor ion  $m/z = 544.22$ . The peak detected at  $m/z = 107.06$  labelled in Figure 3-14, corresponds with an unreacted centre heteroaromatic ring with two remaining methyl groups at the 3 and 5 position; the two – carbon links were broken by the laser energy. The other two peaks of note labelled in Figure 3-14, demonstrate the hydrogenation of a pyrene group with an attached methyl group indicative of scission of the carbon-carbon bridge.

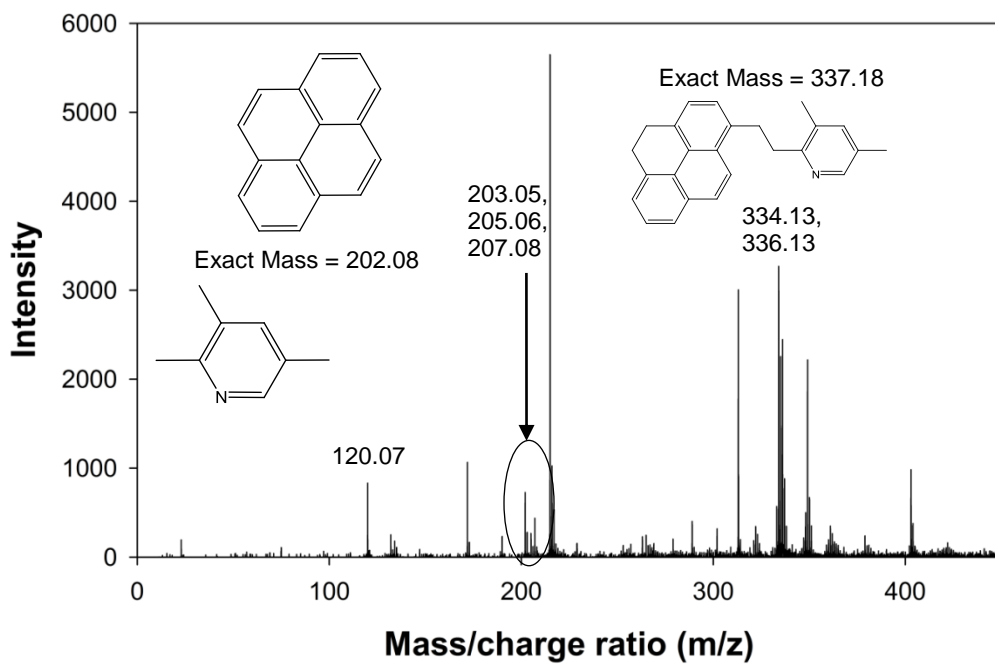


Figure 3-12 MALDI-MS/MS spectrum of P-3-methyl-2,5-pyridine-P hydrogenation product peak  $m/z = 554.28$

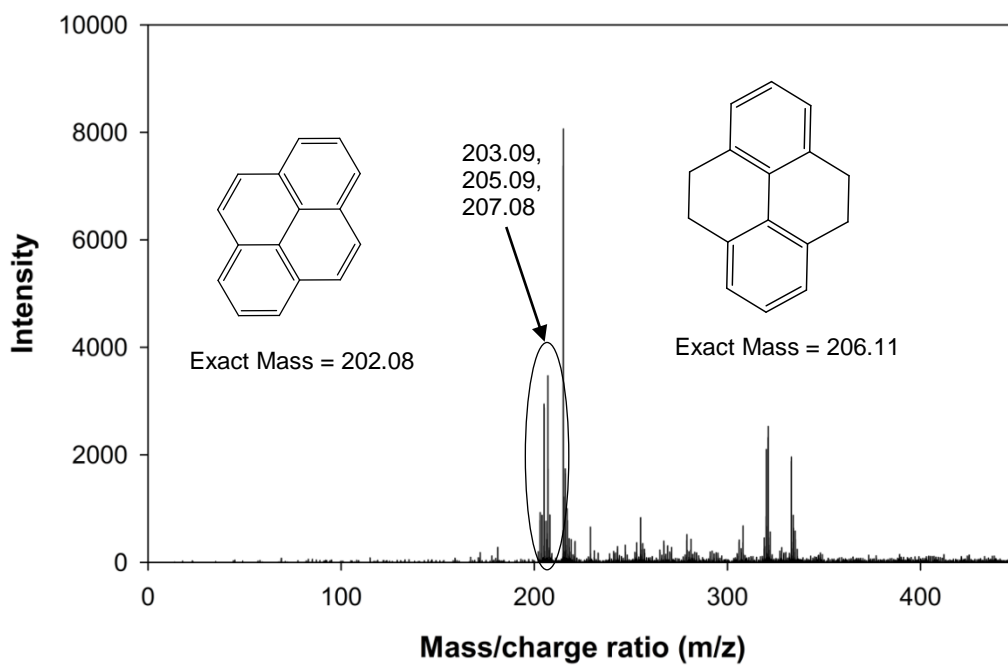
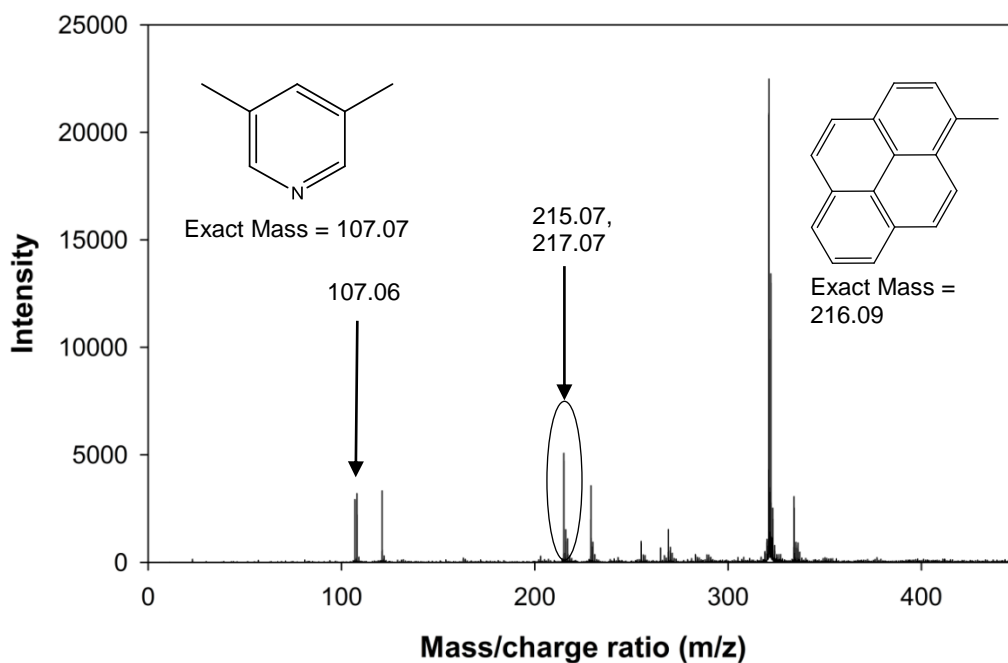


Figure 3-13 MALDI-MS/MS spectrum of P-2,6-pyridine-P hydrogenation product peak  $m/z = 538.19$



**Figure 3-14** MALDI-MS/MS spectrum of P-3,5-pyridine-P hydrogenation product peak  $m/z = 544.22$

### 3.2.3.2 Selectivity Ratio of HDN and Hydrogenation Products by Modified Integrated Peak Area Spectra

The mass of HDN and hydrogenation products was attributed to each pathway using a selectivity ratio determined from MALDI – MS modified integrated peak area spectra of the product samples from the experimental reactions. The modified peak spectrum was developed from analysis of MALDI – MS spectra of the feed and product samples of the catalytic hydrogenation experiments. This analysis of MALDI – MS spectra to produce modified integrated peak area spectra consisted of four steps:

- comparison of MALDI feed and product spectra on an amount-detected basis to identify plausible product peaks;

- the use of MALDI – MS/MS on the plausible product peaks of the product MALDI spectra to verify that the peaks are products of the parent model compound;
- identification of isotopes of both the product and feed spectra product peaks via the Scientific Instrument Service Isotope Distribution Calculator to obtain an accurate measure of the total peak area attributed to each product peak, including isotope peaks;
- construction of the modified integrated product peak spectrum from the summation of the integrated area under each verified product peak in the product MALDI spectrum, accounting for isotopes, minus the integrated area of the same peak if present in the feed MALDI spectrum.

This analysis approach assumed that similar compounds have comparable ionization efficiencies; specifically that the product compounds are similar in chemical structure due to the nature of the reactions and therefore should have similar proportional signal responses to the concentration in the product sample. Also, it was assumed that the samples prepared for MALDI analysis had identical concentrations as the reaction product samples. Complete details of the analysis of the reaction product samples by MALDI are provided in Appendix C.

Figure 3-15 shows the modified integrated peak area spectrum of cholestane-phenyl-*n*-butyl. The height of each bar represents the total increase in peak area of a reaction product sample from the peak area of a feed sample for each identified and verified product peak. This is not the case for the bars labelled ‘parent compound,’ as they represent the peak area of the parent compound for the product sample spectrum only and is shown for comparison with the other modified peaks in the figure.

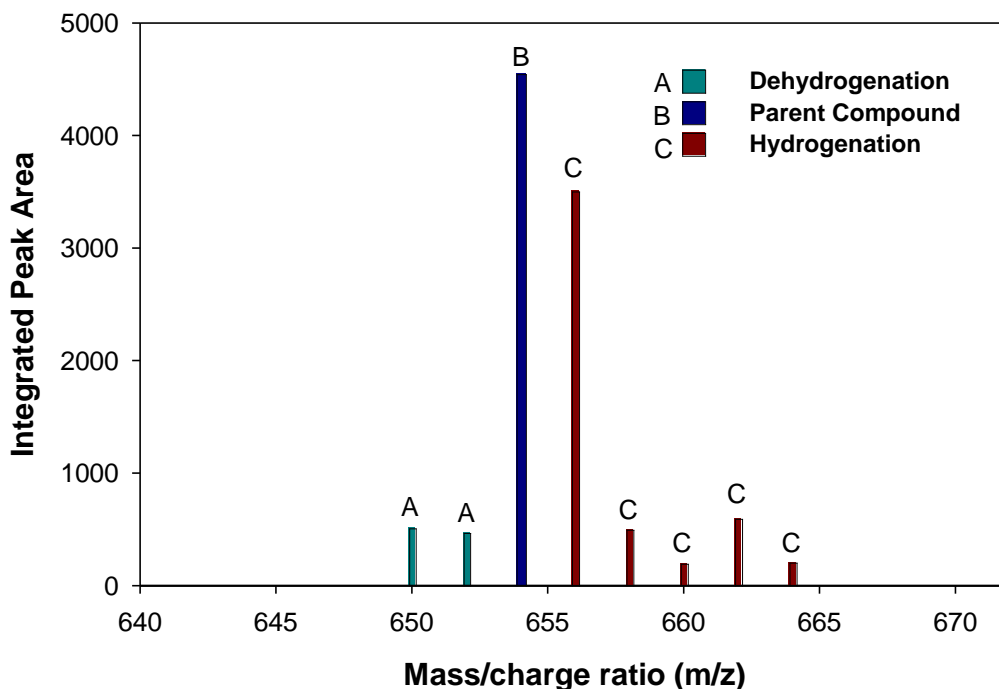


**Figure 3-15** Modified integrated peak area spectrum of cholestane-phenyl-*n*-butyl

Each peak in the figure has been verified as a product and categorized into HDN, hydrogenation or dehydrogenation reaction products by MALDI – MS/MS. This categorization of products by MALDI – MS/MS was achieved by comparing the MALDI – MS/MS spectra of the parent ion and a product ion. Then interpretation of resulting fragment ions within the product ion’s MALDI – MS/MS spectrum would both verify that it is indeed a product ion with common fragments found in the parent ion’s chemical structure, and provide evidence that the ion belonged to one of the reaction product categories. For example, a fragment ion  $m/z$  that could not possibly be reconciled with an intact nitrogen heteroatom ring indicating HDN. The selectivity ratio used for evaluating the yields in Table 3-8 was determined by dividing the sum of the modified integrated peak area attributed to HDN by the same sum attributed to hydrogenation.

Figure 3-15 to Figure 3-17 are the modified integrated peak area spectra for all three cholestane family model compounds, including: cholestane-phenyl-*n*-butyl, cholestane-phenyl, and cholestane-bibenzyl, respectively. It can be observed from the modified integrated peak area spectra that the cholestane family of model compounds underwent solely hydrogenation and dehydrogenation reactions and did not participate in HDN reactions. A single step hydrogen addition reaction product was the most abundant catalytic hydrogenation reaction product of this family of model compounds. There were significantly less other products, which included product compounds as high as five additions of hydrogen to the parent compound. Past this range either the product peaks in the MALDI spectra became too small to be readily distinguished as a product peaks or was not verified by MALDI – MS/MS.

The modified integrated peak area spectra for the pyrene/pyridine family of model compounds P-3,5-pyridine-P, P-3-methyl-2,5-pyridine-P and P-2,6-pyridine-P are shown in Figure 3-18, Figure 3-19 and Figure 3-20, respectively.

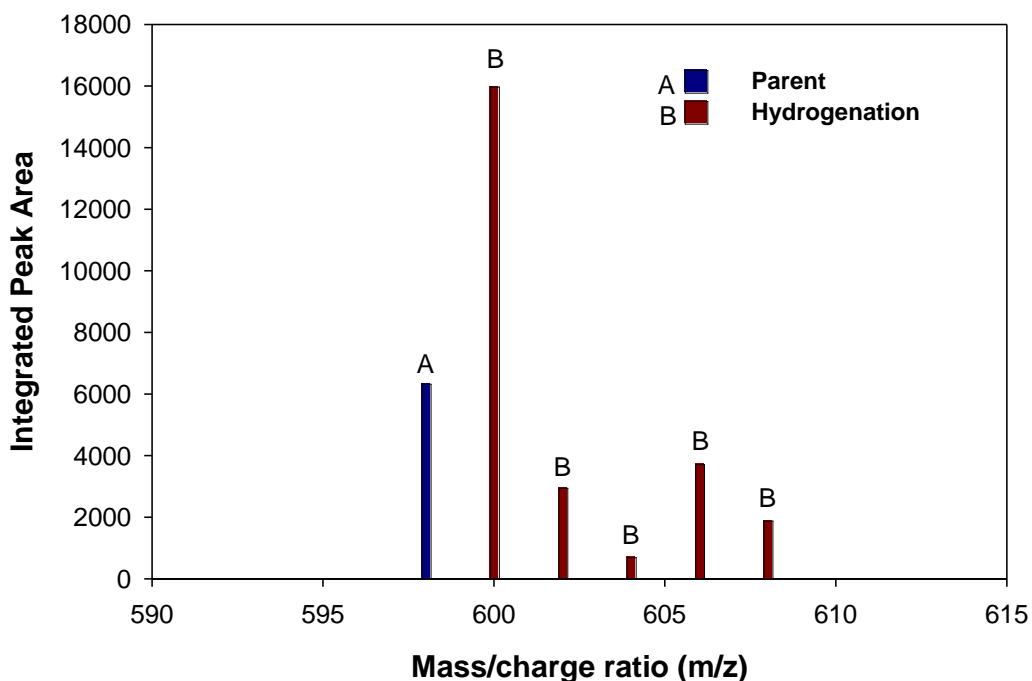


Figure 3-16 Modified integrated peak area spectra of cholestane-phenyl

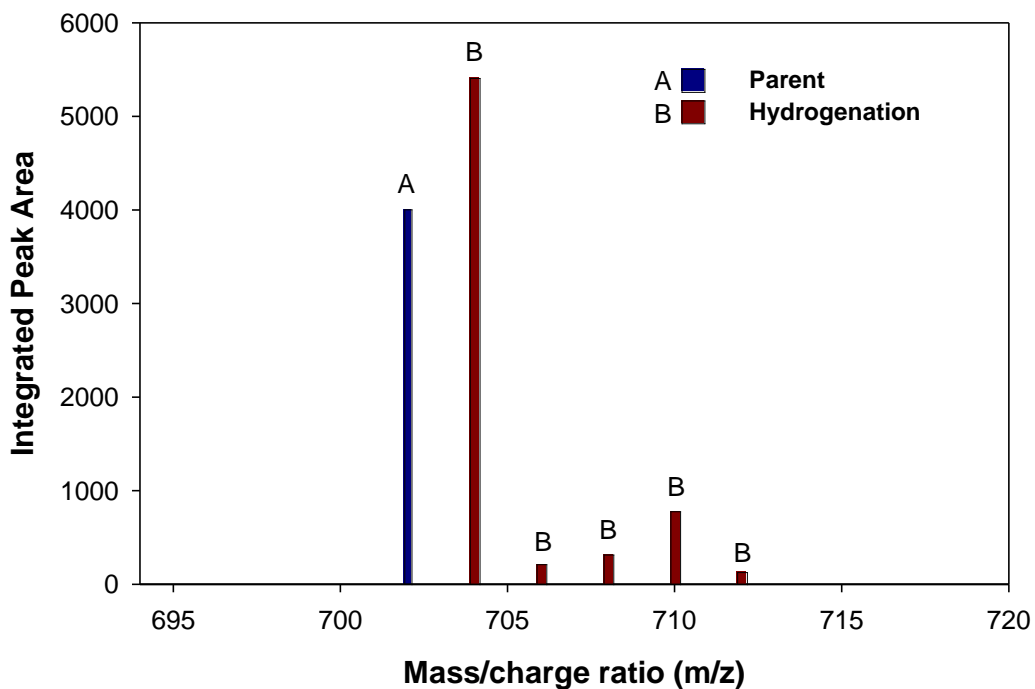


Figure 3-17 Modified integrated peak area spectra of cholestane-bibenzyl

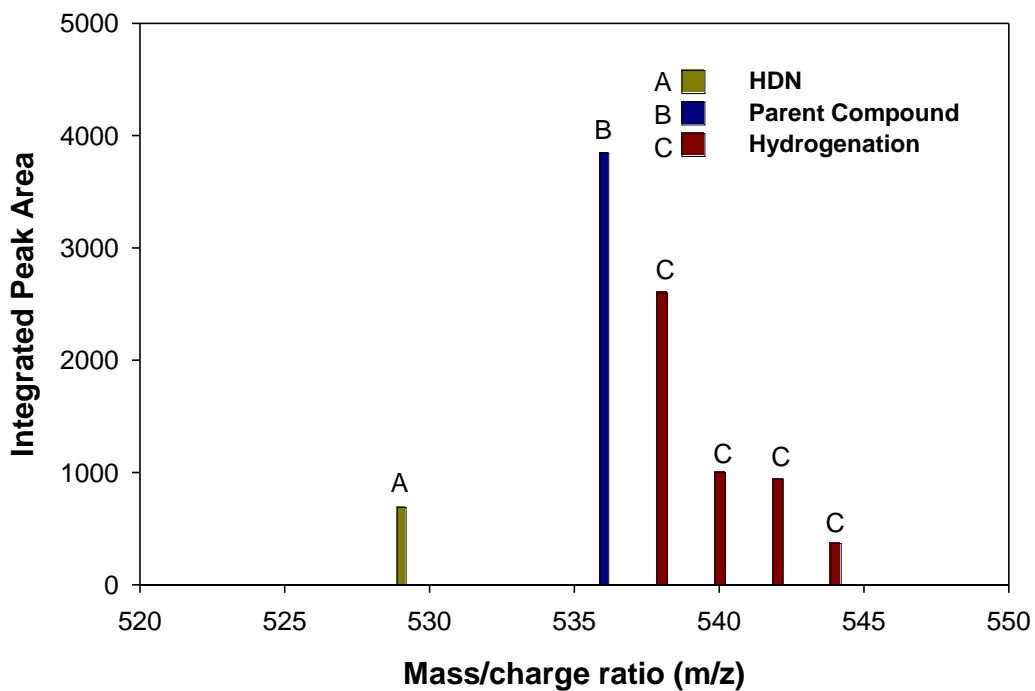


Figure 3-18 Modified integrated peak area spectra of P-3,5-pyridine-P

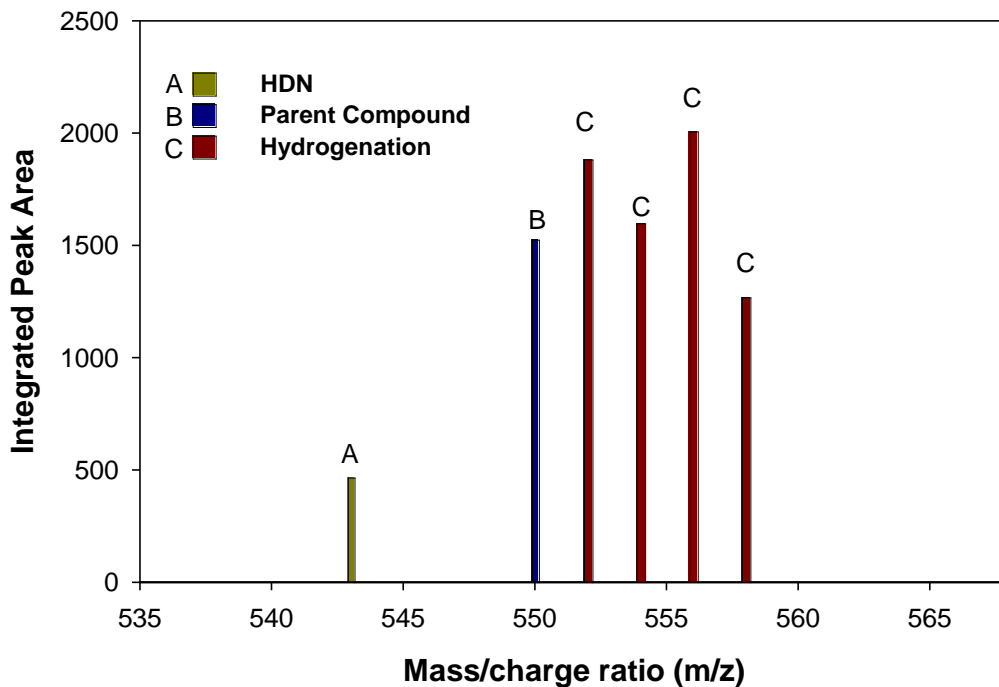


Figure 3-19 Modified integrated peak area spectra of P-3-methyl-2,5-pyridine-P

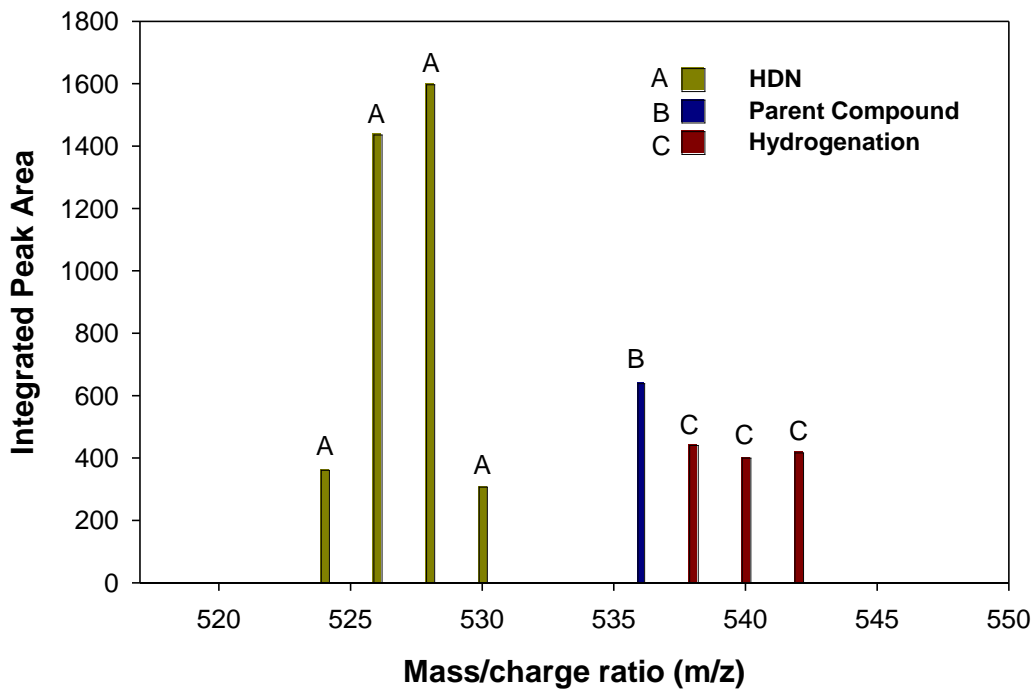


Figure 3-20 Modified integrated peak area spectra of P-2,6-pyridine-P

The pyrene/pyridine family of model compounds reacted in both HDN and hydrogenation reaction pathways to different extents depending on the model compound involved. This result is demonstrated by comparing the modified integrated peak area spectra of P-3,5-pyridine-P (Figure 3-18) and P-2,6-pyridine-P (Figure 3-20). A simple change in the bridging locations on the centre heteroatomic ring produced a significant difference in the amount of HDN occurring. The model compounds P-3-methyl-2,5-pyridine-P and P-3,5-pyridine-P exhibited similar behaviour despite having greater differences in chemical structure than between P-3,5-pyridine-P and P-2,6-pyridine-P. Both yielded predominantly hydrogenation products with only one HDN product, 7 Da smaller than the parent compound, corresponding to hydrogenation of the heteroatomic ring and removal of the nitrogen from the heteroatomic ring by ammonia elimination. The model compound P-2,6-pyridine-P produced the most HDN products of any compound investigated and had an HDN yield significantly greater than the other two pyrene/pyridine compounds. The other product peaks attributed to HDN in Figure 3-20, those peaks not 7 Da smaller than the parent compound, represent HDN products that have been further hydrogenated or dehydrogenated and all were confirmed via MALDI – MS/MS. Similar to the cholestane family of model compounds no more than four hydrogen addition reaction steps (+ 4H<sub>2</sub>) to the parent compound was detected.

### **3.2.3.3 Irreversible Adsorption of Nitrogen Compounds onto Catalyst**

#### **Surface**

Partial hydrogenation of the pyridine rings on the model compounds could generate amine compounds. Cyclic amine product compounds were of particular concern because of their potential to irreversibly adsorb onto the catalyst surface and their importance establishing model compound pathway yields and behaviour. Since the mass to charge ratio corresponding to a potential cyclic amine product was successfully detected by MALDI – MS but not verified by MALDI – MS/MS, i.e. the fragment ion of a precursor ion that could possibly be a cyclic

amine, did not suggest that the centre pyridine ring was hydrogenated. Therefore, another check with Fourier transform infrared spectroscopy (FT – IR) was conducted to ensure that cyclic amines were not present in the product samples. Figure 3-21 and Figure 3-22 are IR spectra of the model compound cholestane-phenyl and 1,2,3,4-tetrahydroquinoline in tetralin solvent, respectively. The FT – IR spectrum taken of 1,2,3,4-tetrahydroquinoline in tetralin was to ensure that the FT – IR instrument effectively detected an amine group and at what wave number that particular amine group would be expected to appear. According to Figure 3-22, a cycloamine attached to another aromatic ring is detected at a wave number of approximately  $3400\text{cm}^{-1}$ . This vibration of the amine group at  $3400\text{cm}^{-1}$  is absent from the IR spectrum of the cholestane-phenyl product sample shown in Figure 3-21, and is likewise absent in the IR spectra for the other two model compounds of the cholestane family. From these results we conclude that no detectable amines were present in the product mixtures from the cholestane compounds, and that the hydrogenation of these compounds was in the other aromatic rings, not in the heteroaromatic ring.

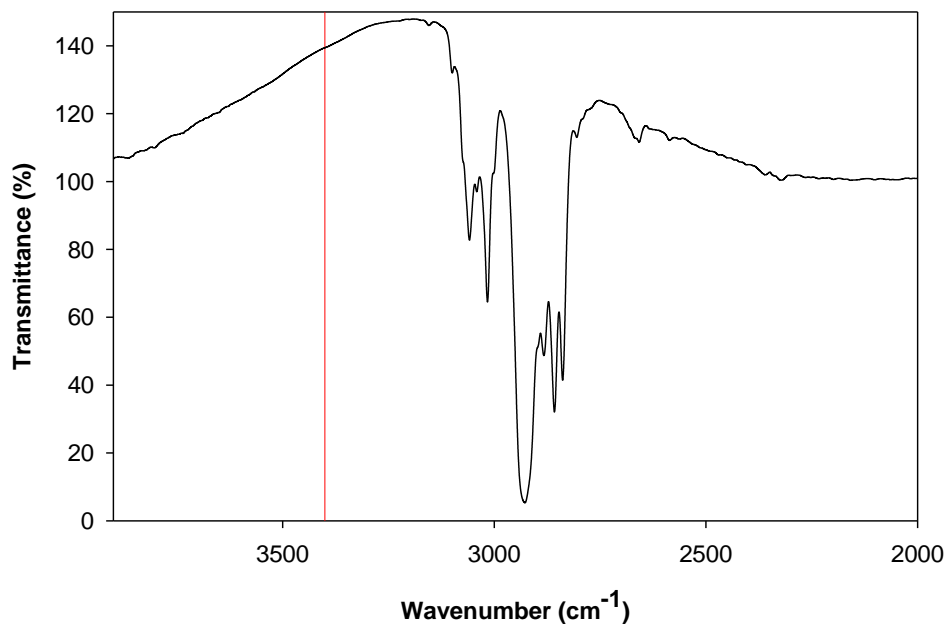


**Figure 3-21** IR spectrum of cholestane-phenyl reaction product in tetralin solvent. The reference line indicates the wave number for amine vibration.

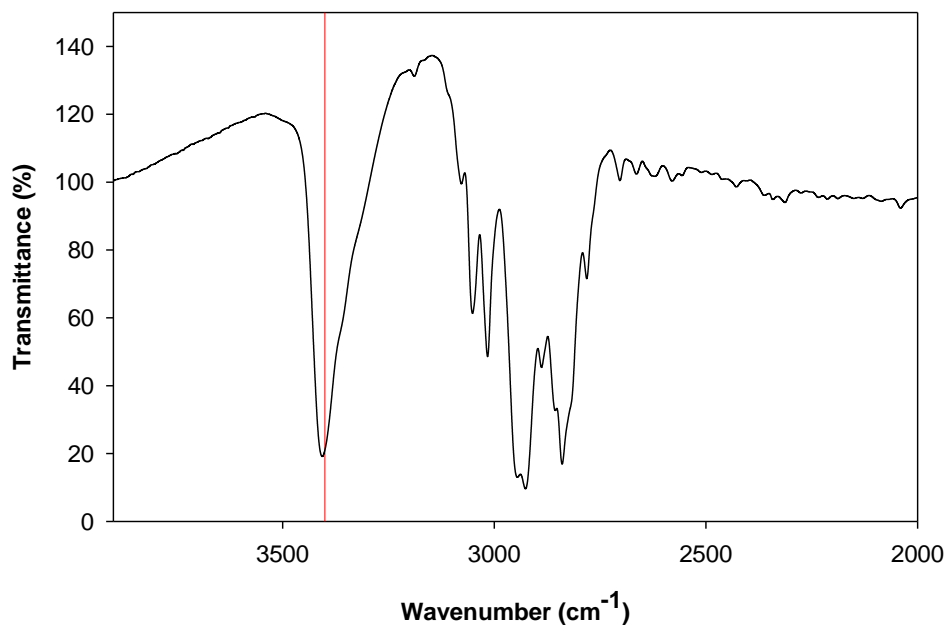


**Figure 3-22** IR spectrum of 1,2,3,4-tetrahydroquinoline in tetralin solvent. The reference line indicates the wave number for amine vibration.

### 3.3 References

- Kanda, W., I. Siu, J. Adjaye, A. E. Nelson and M. R. Gray. Inhibition and Deactivation of Hydrodenitrogenation (HDN) Catalysts by Narrow-Boiling Fractions of Athabasca Coker Gas Oil. *Energy & Fuels* **2003**, 18, 539-546.
- Satterfield, C. N. and S. H. Yang. Catalytic Hydrodenitrogenation of Quinoline in A Trickle-Bed reactor. Comparison with Vapor Phase Reaction. . *Ind. Eng. Chem. Process Des. Dev.* **1984**, 23, 11-19.
- Shabtai, J., L. Veluswamy and A. G. Oblad. Steric Effects in Phenanthren and Pyrene Hydrogenation Catalyzed by Sulfided Ni-W / Al<sub>2</sub>O<sub>3</sub>. *Prepr. Pap. - Am. Chem. Soc., Div. Fuel Chem.* **1978**, 23, 114-118.

# CHAPTER 4

---

## Discussion and Conclusions

### **4.1 Pyrene/Pyridine Family of Model Compounds**

Schematics of the main products from each pathway detected for the catalytic hydrogenation reactions of the pyrene/pyridine family and the selectivity for each pathway are illustrated in Figure 4-1, Figure 4-2 and Figure 4-3. Pyrene-3-methyl-2,5-pyridine-pyrene yielded nearly double the amount of cracked products of the other two model compounds. This difference could be the result of steric hindrance in adsorbing onto the catalyst surface, caused by the substituted methyl group,

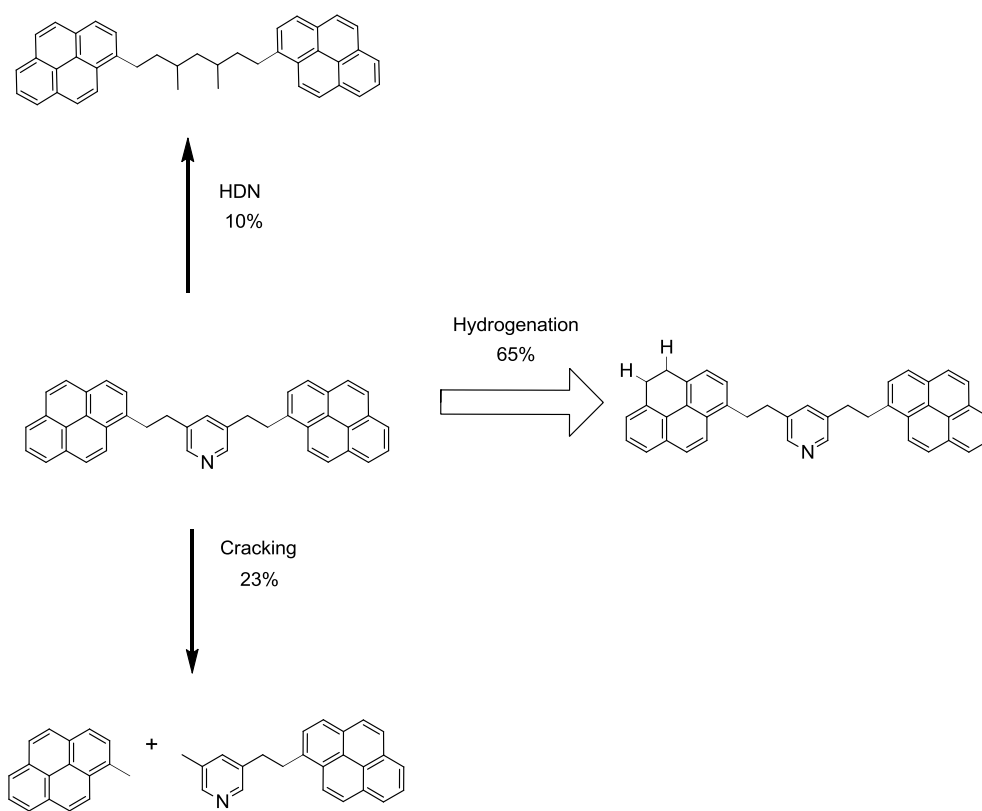


**Figure 4-1** Schematic of the main products from each of the detected pathways of the catalytic reaction of pyrene-3,5-pyridine-pyrene, with the corresponding selectivity on a mass basis

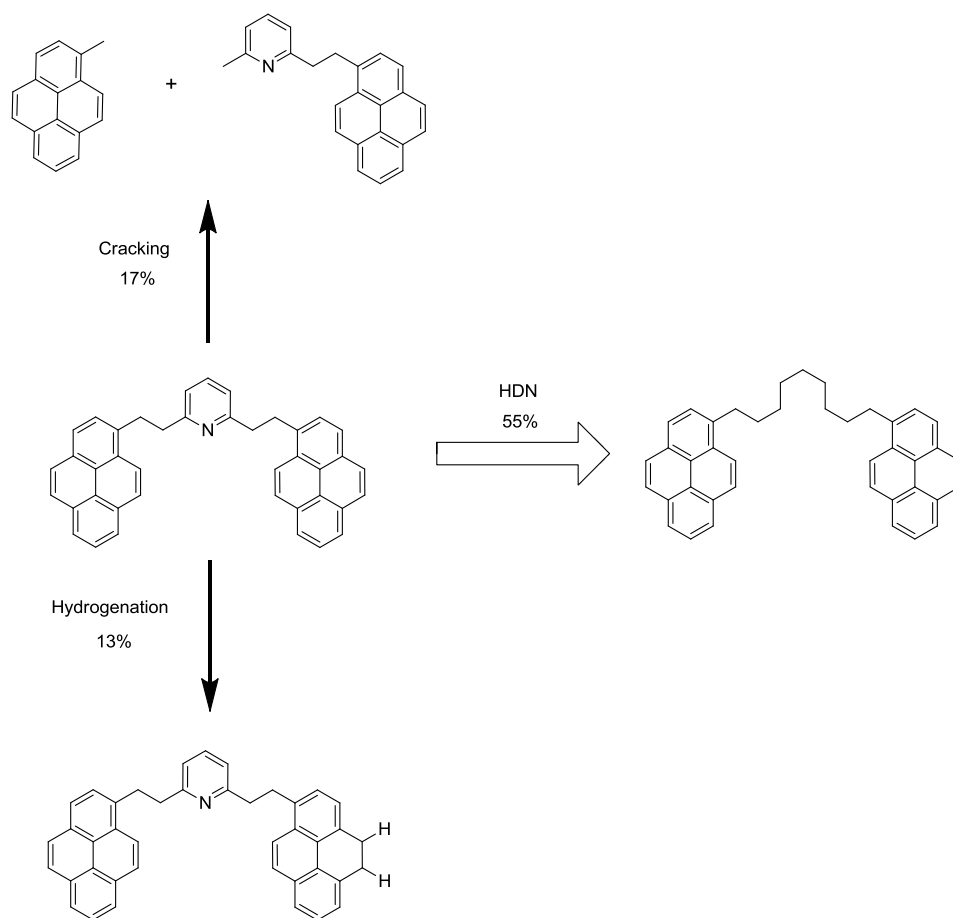


**Figure 4-2** Schematic of the main products from each of the detected pathways of the catalytic reaction of pyrene-2,6-pyridine-pyrene, with the corresponding selectivity on a mass basis

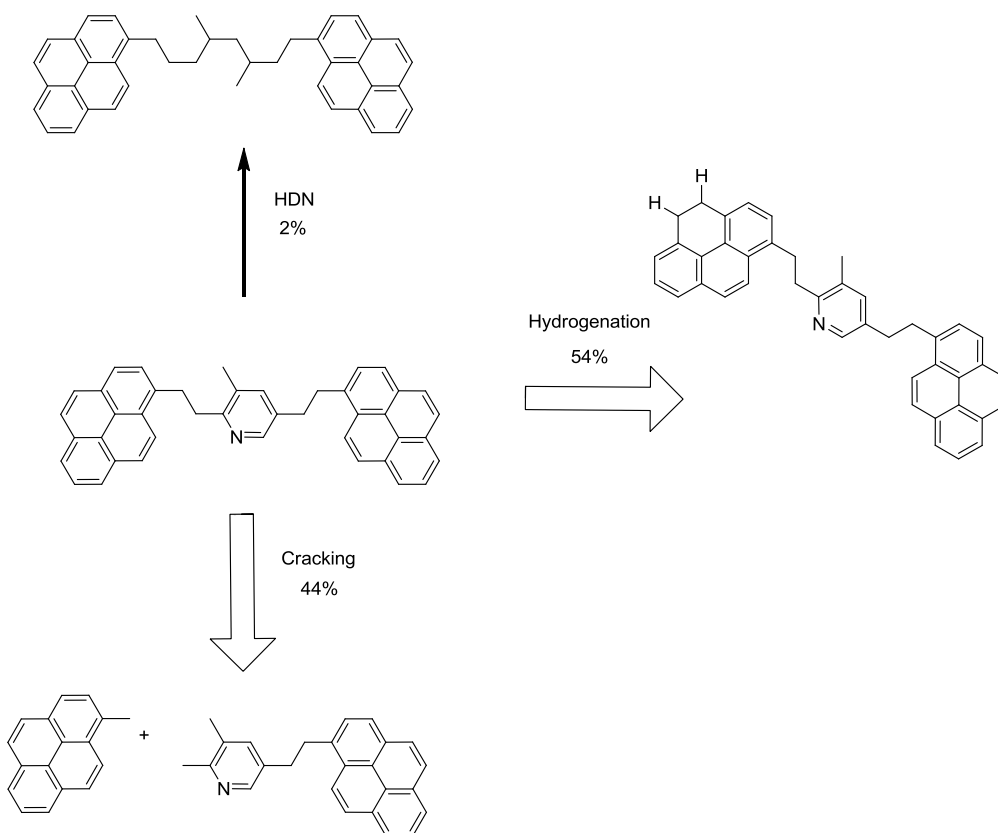


**Figure 4-3** Schematic of the main products from each of the detected pathways of the catalytic reaction of pyrene-3-methyl-2,5-pyridine-pyrene, with the corresponding selectivity on a mass basis

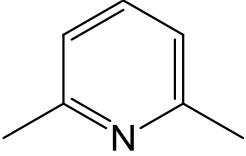
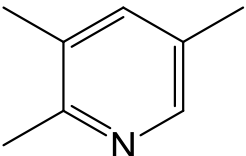
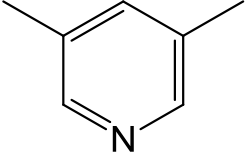
promoting the cracking reaction instead of hydrogenation or hydrodenitrogenation reactions. Nevertheless, the other two pyrene/pyridine model compounds exhibited modest cracking under these conditions. The major cracked products were the same for all three pyrene/pyridine model compounds. These cracked products included: pyrene, methyl-pyrene and smaller amounts of 9,10-dihydropyrene and other singly hydrogenated pyrene species as detected by GC – MS. The cracked products identified follow known cracking behaviour including  $\beta$  – scission of the C – C bridge to give methyl-pyrene as a detectable cracked product, and cleavage of the aryl – alkyl C – C bond to generate pyrene as a detectable cracked product. Precedent for cleavage of this strong aryl – alkyl C –

C bond was established by Freund et al. (1991) and Savage et al. (1989), where they observed dealkylation of alkylated pyrene compounds to yield pyrene.

The only model compound in the pyrene/pyridine family to exhibit significant HDN was P-2,6-pyridine-P. The model compound P-3,5-pyridine-P yielded a minor amount of HDN products and P-3-methyl-2,5-pyridine-P generated an insignificant quantity of HDN products. The lack of HDN products for P-3-methyl-2,5-pyridine-P can be attributed to steric hindrance from the alkyl substitution of the heteroatomic ring. Table 4-1 elucidates two observed trends discerned from the data presented in Table 3-8. First, that the data is consistent with the hypothesis that the more basic central ring is more effectively denitrogenated. Thus the stark difference in selectivity between the model compounds P-2,6-pyridine-P and P-3,5-pyridine-P could be attributed to the large basicity difference of the centre heteroatomic rings, i.e. a  $pK_b$  of 7.33 and 8.19 for 2,6-dimethyl-pyridine and 3,5-dimethyl-pyridine, respectively. The second trend is that the overall conversion by all pathways for the model compounds adheres to an inverse relationship with basicity. That is, the more basic pyridinic centre ring exhibited less overall conversion by all pathways. However, results from Cox and Berg (1962), where heterocyclic nitrogen containing hydrocarbons were catalytically hydrogenated by a flow reactor at circa 370 °C with a Raney nickel catalyst, found that 2,6-dimethyl-pyridine had an overall reaction rate constant more than six times larger than 3,5-dimethyl-pyridine at the same conditions and feed concentration, and showed no relationship between basicity and the overall reactivity of the alkyl-substituted pyridine compounds. These two trends taken together show that pyrene/pyridine model compounds that undergo a significant amount of HDN result in low overall conversions. Therefore, these observations suggest that binding of the reactant molecule to the catalyst active sites to undergo HDN inhibit hydrogenation.

All the HDN products identified for all three model compounds of the pyrene/pyridine family were consistent with the HDN mechanism supported in literature, i.e. saturation of the nitrogen containing ring followed by hydrogenolysis of the C – N bond and subsequent elimination of ammonia. The

**Table 4-1** Comparison of overall reactivity by all pathways, the yield of HDN products (%) and heteroatomic centre ring basicity for the pyrene/pyridine family

Model Compound	Conversion by all pathways (%)	Yield of HDN Products (%)	Centre heterocyclic ring	pK <sub>b</sub>
P-2,6-pyridine-P	69 ± 2	38	 2,6-dimethyl-pyridine	7.33
P-3-methyl-2,5-pyridine-P	84 ± 1	2	 2,3,5-trimethyl-pyridine	7.47
P-3,5-pyridine-P	>99	10	 3,5-dimethyl-pyridine	8.19

main HDN product would then be represented in a MALDI – MS spectrum by a product peak 7 Da less than the parent compound. This is confirmed by both the appropriate modified integrated MALDI – MS spectra for each model compound, and by MALDI – MS/MS spectra suggesting only structures consistent with these HDN products.

According to Figure 4-1, Figure 4-2 and Figure 4-3, the selectivity for the hydrogenation of the model compounds P-3,5-pyridine-P and P-3-methyl-2,5-pyridine-P were similar, whereas, for P-2,6-pyridine-P hydrogenation was a minor

pathway for reaction. Up to four hydrogen addition steps were detected for all three pyrene/pyridine model compounds and both P-2,6-pyridine-P and P-3-methyl-2,5-pyridine-P showed no preference in abundance for these four hydrogenation products. In contrast, from Figure 3-18, it is evident that the most abundant hydrogenation product for P-3-methyl-2,5-pyridine-P was the first H<sub>2</sub> addition with diminishing abundance with increasing hydrogenation. The main hydrogenation product for this family of model compounds, as illustrated in the above figures, shows the hydrogen addition occurring on the pyrene group, particularly at the 9,10- position. The location of this hydrogen addition at the pyrene group is supported by four results:

- the MALDI – MS/MS spectra of hydrogenation products showing fragment ions consistent with partially saturated pyrene groups as illustrated in both Figure 3-12 and Figure 3-13,
- the lack of fragment ions consistent with hydrogenation of the centre pyridinic ring without nitrogen removal from MALDI – MS/MS spectra of hydrogenation products,
- detection of the centre pyridinic ring intact without hydrogenation from the MALDI – MS/MS spectra of hydrogenation products as shown in Figure 3-12,
- detection of 9,10-dihydropyrene and other hydrogenated pyrene cracked products from all three model compounds via GC – MS.

Hydrogen addition occurring particularly at the 9,10- position on a pyrene group is because it is the most likely location for hydrogenation to take place on the pyrene structure, as that is the weakest carbon – carbon bond.

Results for the pyrene/pyridine family are consistent with two mutually exclusive phenomena: either hydrogenation of the centre pyridinic ring or hydrogenation of the linked pyrenes. This observation suggests that the reaction scheme of these large molecules permits only adsorption of one of the three rings onto the catalyst surface. Furthermore, the patterns of reaction observed indicate

that the basicity and steric substitution of the centre ring determine whether pyrene or pyridine rings adsorb to the active site.

## 4.2 Cholestane Family of Model Compounds

The schematic of the main product detected from the catalytic hydrogenation of the cholestane family of model compounds is illustrated in Figure 4-4. Only hydrogenation and dehydrogenation products were detected for the cholestane family of model compounds. From Figure 3-15 to Figure 3-17, it is evident that the most abundant product generated for all three model compounds was a singly hydrogenated compound, with significantly less amounts of greater hydrogen addition products being formed. The likely H<sub>2</sub> addition location is the 9,10- position on the 5,6-benzoquinoline structures, as shown in Figure 4-4. The only other identified and verified products from the catalytic reactions of the three cholestane model compounds were dehydrogenated products formed from the reaction of cholestane-phenyl-*n*-butyl, shown in Figure 3-15. No cracked products were detected from these compounds by MALDI – MS. What little product peaks were present in MALDI – MS product spectra that corresponded to possible cracked products were not confirmed by MALDI – MS/MS and were either matrix adducts or contaminants.

No reaction of the nitrogen-bearing ring was found to take place for the cholestane family of compounds. First, no HDN products were identified in the MALDI – MS spectra for these compounds. Second, there was an absence of cycloamine product compounds as evaluated by FT – IR, as illustrated in Figure 3-21 and Figure 3-22. Both published reaction networks for 5,6-benzoquinoline from Shabtai et al. (1989) and Moreau et al. (1988) found that hydrogenation of the heterocycle was a major pathway to HDN, therefore, the absence of a cycloamine peak indicates the nitrogen-bearing ring was not hydrogenated. Moreover, the product distribution provided by Shabtai et al. (1989) for the HDN of 5,6-benzoquinoline showed appreciable amounts of 1,2,3,4-tetrahydrobenzoquinoline in the product mixture. For significant HDN to occur,

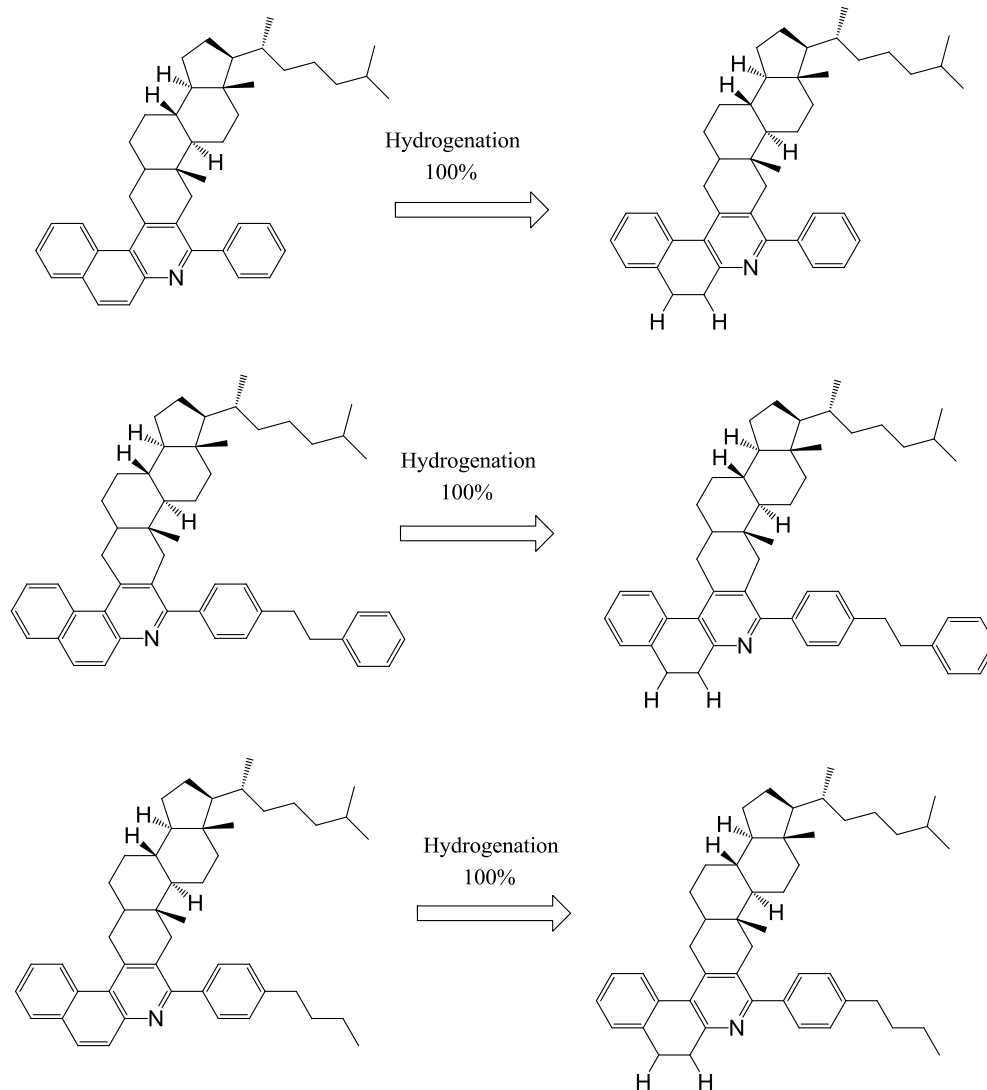


**Figure 4-4** Schematic of the main product from the reaction pathway detected from the catalytic reaction of the cholestane family of model compounds. In descending order: cholestane-phenyl, cholestane-bibenzyl and cholestane-phenyl-*n*-butyl.

hydrogenation of the heteroatomic ring to a saturated amine must occur. Therefore, the absence of cycloamines present in the product mixtures and the absence of any HDN products strongly suggest that no nitrogen removal is taking place.

The reactivity of the cholestane compounds, considering the conversion from all pathways in Figure 3-8, is comparable to one another despite differences

in the attached functional group to the heteroatomic ring. The pseudo-first order reaction rate constants could only be determined for the model compound cholestane-phenyl, because the product concentrations of the other two cholestane model compounds were too low to provide a reliable measurement by calibration curve.

Comparing the conversions by all pathways between the two model compound families and the reaction rate constants of cholestane-phenyl and P-3-methyl-2,5-pyridine-P, it is clear that the cholestane family is more reactive than the pyrene/pyridine family. Prins (2001) suggests that larger nitrogen compounds tend to react more readily than smaller nitrogen compounds because of the larger adsorption constants and weaker aromaticity of the larger nitrogen compounds. Therefore, if adsorption behaviour of the model compounds is dominated by the basic nitrogen centre heteroatomic ring, then a qualitative comparison of reactivity can be drawn from already published data on the reactivity of 5,6-benzoquinoline and alkyl substituted pyridines. Kinetic data from Cox and Berg (1962) shows that acridine is more reactive than many alkyl substituted pyridines. For example, the first order reaction rate constants for 3-ethyl-4-methyl-pyridine, 2,4-dimethyl-pyridine and 3,5-dimethyl-pyridine are  $0.114 \text{ h}^{-1}$ ,  $0.272 \text{ h}^{-1}$  and  $0.271 \text{ h}^{-1}$ , respectively; compared to  $0.399 \text{ h}^{-1}$  for acridine. Furthermore, results from Katti and Gates (1986) demonstrated that 5,6-benzoquinoline was more reactive than acridine at  $400 \text{ }^\circ\text{C}$  and  $13.3 \text{ MPa}$ . Therefore, the higher reactivity of the cholestane family as compared to the pyrene/pyridine family correlates well with the reactivity of the aromatic nitrogen containing centre of these compounds.

### **4.3 Implications**

This study is the first to investigate the behaviour of large multi-ring aromatic nitrogen compounds undergoing catalytic hydrogenation under industrial hydrotreating conditions. The data presented in Table 3-8 and the pathway schematics illustrated in Figure 4-1 to Figure 4-4, provide strong evidence that these molecules can crack or hydrogenate easily, but do not undergo HDN

readily, even under these conditions favourable for nitrogen removal. This observation applies despite significant differences in structure among the model compounds. Moreover, this behaviour is unlike the reaction networks and other data published for smaller polycyclic aromatic nitrogen compounds such as benzoquinoline, acridine, and quinoline. The asphaltene model compounds do not readily hydrogenate on the heteroatomic rings to form saturated amine intermediates, which is not the case for smaller nitrogen compounds as demonstrated in reaction networks for 5,6-benzoquinoline by Nagai et al. (1986) and Moreau et al. (1988) and quinoline by Satterfield and Yang (1984). As suggested by Jokuty and Gray (1992), larger nitrogen compounds such as the asphaltene model compounds studied do not undergo nitrogen removal without extensive hydrogenation and cracking of rest of the compound, in a complex, multi-step process. The implication of these results is that hydrotreatment of these large polycyclic aromatic nitrogen-containing asphaltene compounds will be dominated by reactions other than HDN, and that investigation into the behaviour of the small nitrogen species already studied give limited insight to the varied and complex reactions occurring for the larger asphaltene model compounds.

#### **4.4 Conclusions**

The pathways for the catalytic hydrogenation of the pyrene/pyridine model compounds included cracking, hydrogenation and hydrodenitrogenation, depending on the model compound observed. The pyrene/pyridine family of asphaltene model compounds exhibited a strong preference for the hydrogenation of the bridged pyrene groups over the hydrogenation of the centre pyridinic ring. Alkyl-substitution and bridging locations on the heteroatomic ring was a significant factor in reactivity and HDN selectivity.

There were no observed cracking or HDN reactions for the cholestane family of asphaltene model compounds. No cycloamine intermediates were detected in the product mixtures of the catalytic hydrogenation reactions of

cholestane model compounds, which confirmed that hydrogenation of the heteroatomic ring does not take place.

## 4.5 References

- Cox, K. E. and L. Berg. Destructive catalytic hydrogenation of heterocyclic nitrogen compounds. *Chemical Engineering Progress* **1962**, 15(12), 54-55.
- Freund, H., M. G. Matturro, W. N. Olmstead, R. P. Reynolds and T. H. Upton. Anomalous side chain cleavage in alkylaromatic thermolysis. *Energy & Fuels* **1991**, 5, 840-846.
- Jokuty, P. L. and M. R. Gray. Nitrogen Bases Resistant to Hydrodenitrogenation: Evidence against Using Quinoline as a Model Compound. *Ind. Eng. Chem. Res.* **1992**, 31, 1449-1457.
- Katti, S. S. and B. C. Gates. Catalytic Hydroprocessing of SRC-II Heavy Distillate Fractions. 6. Hydroprocessing of the Bases and Neutral Resins. *Ind. Eng. Chem. Process Des. Dev.* **1986**, 25, 618-626.
- Moreau, C., R. Durand, N. Zmimita and P. Geneste. Hydrodenitrogenation of Benzo(f)quinoline and Benzo(h)quinoline over a Sulfided NiO-MoO<sub>3</sub>/□-Al<sub>2</sub>O<sub>3</sub> Catalyst. *Journal of Catalysis* **1988**, 112, 411-417.
- Prins, R. Catalytic Hydrodenitrogenation. *Advances in Catalysis* **2001**, 46.
- Satterfield, C. N. and S. H. Yang. Catalytic Hydrodenitrogenation of Quinoline in A Trickle-Bed reactor. Comparison with Vapor Phase Reaction. . *Ind. Eng. Chem. Process Des. Dev.* **1984**, 23, 11-19.
- Savage, P. E., G. E. Jacobs and M. Javanmardian. Autocatalysis and aryl alkyl bond cleavage in 1-dodecylpyrene pyrolysis. *Ind. Eng. Chem. Res.* **1989**, 28, 645-653.
- Shabtai, J., G. J. C. Yeh, C. Russell and A. G. Oblad. Fundamental Hydrodenitrogenation Studies of Polycyclic N-Containing Compounds Found in Heavy Oils. 1. 5,6-Benzoquinoline. *Ind. Eng. Chem. Res.* **1989**, 28, 139-146.

# APPENDIX A

---

## HPLC Calculations and Chromatograms

This appendix details the calculations performed on HPLC chromatograms to obtain the feed model compound concentration remaining in the reaction product mixtures. Included are the chromatograms, calibrations curves and formulae needed to do so.

### **1 Calculations by Calibration Curve**

HPLC calibrations curves were constructed for model compound measurement for the following model compounds: P-3,5-pyridine-P, P-3-methyl-pyridine-P and cholestane-phenyl. Calibration curves were made by tabulating the measured signal response, i.e. peak area, of a known quantity of analyte at

differing concentration in replicate. Table A-3 is an example of the data obtained to construct a calibration curve, in this case, for model compound P-3-methyl-2,5-pyridine-P. The internal standard response factor,  $R_{IS}$ , is defined by the following:

$$R_{is} = \frac{A_{is}}{C_{is}} \quad (\text{A-1})$$

where  $A_{IS}$  is the internal standard peak area and  $C_{IS}$  is the internal standard concentration.

The calibration curves are the resulting plot of model compound concentration vs. the ratio of model compound peak area to the internal standard response factor. If the signal response (the aforementioned ratio) has a linear relationship with model compound concentration then a linear regression can be obtained from the calibration curve. Model compound concentrations can then be calculated from these linear regressions directly. The calibration curves used in this work are presented in Figure A-5 to Figure A-7, with the resulting linear regression equations listed in Table A-2.

**Table A-2** Calibration curve linear regression equations and error

Model Compound	Linear Regression Equation $y = mx + b$		$R^2$
	$x$	$b$	
P-3-methyl-2,5-pyridine-P	3.812	-0.0936	0.9917
P-3,5-pyridine-P	0.224	-0.0384	0.9923
cholestane-phenyl	0.383	-0.0495	0.9999

**Table A-3** Calibration curve data for P-3-methyl-2,5-pyridine-P

<b>Sample</b>	<b>Concentration of model compound (mg/mL)</b>	<b>Model compound peak height (mAU)</b>	<b>Internal Standard Concentration (mg / mL)</b>	<b>Internal Standard Peak Area (mAU·s)</b>	<b>Internal standard response factor (mAU/(mg/mL))</b>	<b>Ratio of model compound peak height to internal standard response factor</b>
<b>1</b>	2.40	1373	5.34	11116	2082	0.66
<b>2</b>	2.40	1351	5.34	11450	2144	0.63
<b>3</b>	2.40	1522	5.34	11889	2226	0.68
<b>4</b>	2.00	1183	4.45	9380	2108	0.56
<b>5</b>	2.00	1175	4.45	9607	2159	0.54
<b>6</b>	1.60	926	3.56	7745	2175	0.43
<b>7</b>	1.60	943	3.56	8197	2303	0.41
<b>8</b>	1.20	686	2.67	5457	2044	0.34
<b>9</b>	1.20	717	2.67	5421	2030	0.35
<b>10</b>	0.80	463	1.78	3355	1885	0.25
<b>11</b>	0.80	473	1.78	3445	1935	0.24
<b>12</b>	0.40	249	0.89	1616	1816	0.14
<b>14</b>	0.40	231	0.89	1635	1837	0.13

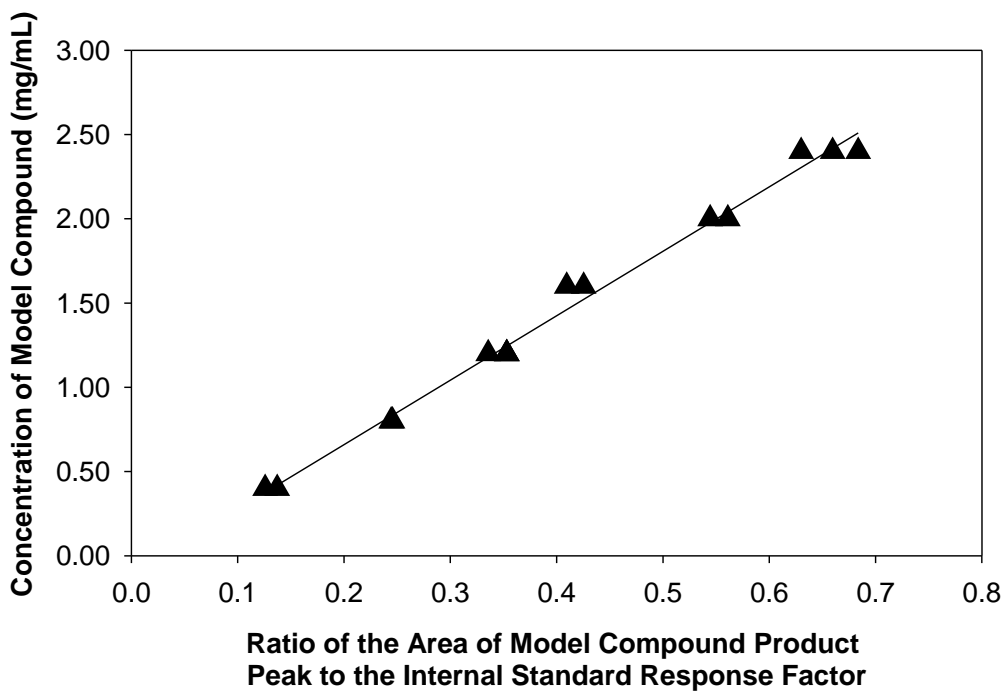


Figure A-1 HPLC calibration curve of P-3-methyl-2,5-pyridine-P

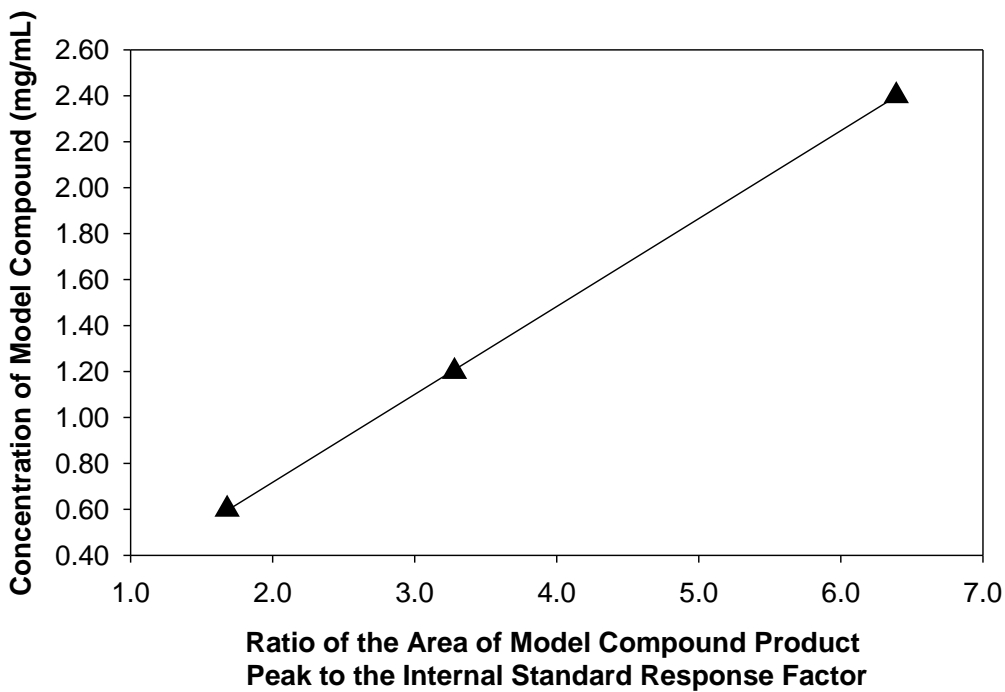


Figure A-2 HPLC calibration curve of cholestane-phenyl

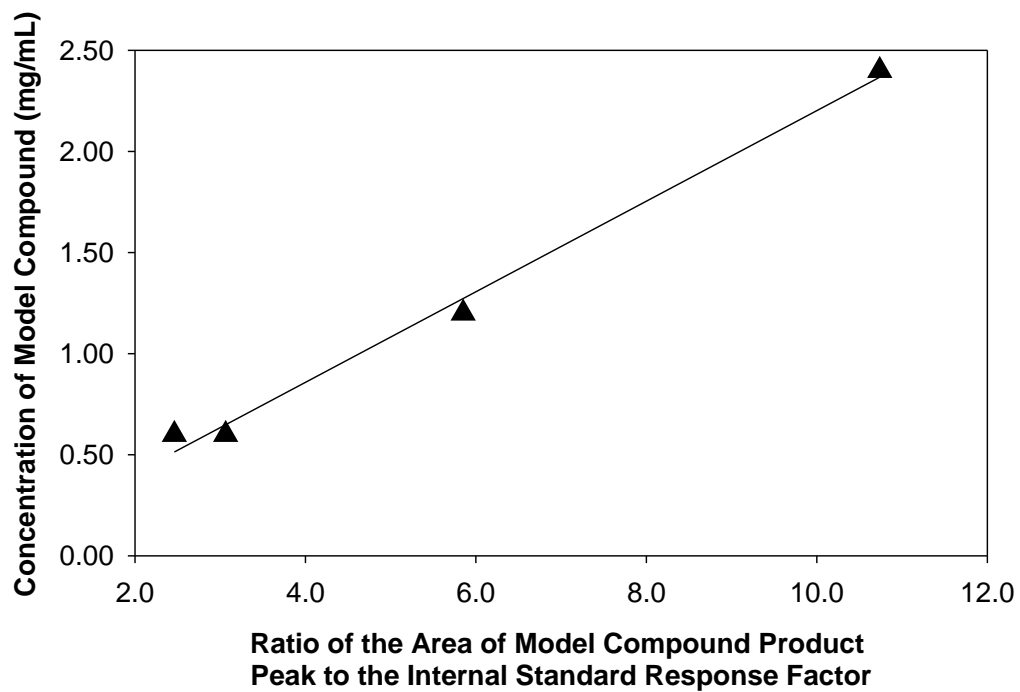


Figure A-3 HPLC calibration curve of P-3,5-pyridine-P

## 2 HPLC Chromatograms

The following are the chromatograms used in measurement of reaction product concentrations of model compounds:

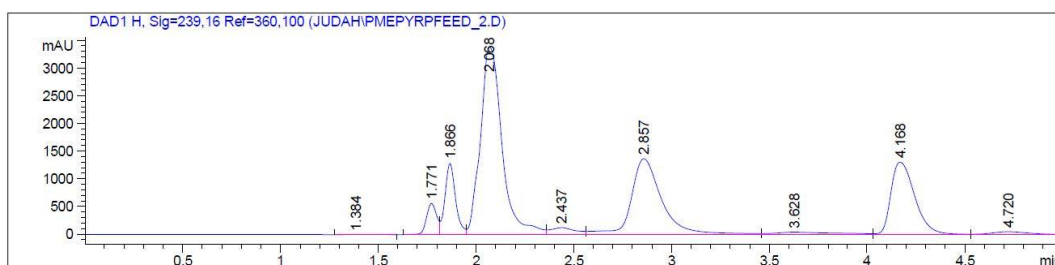
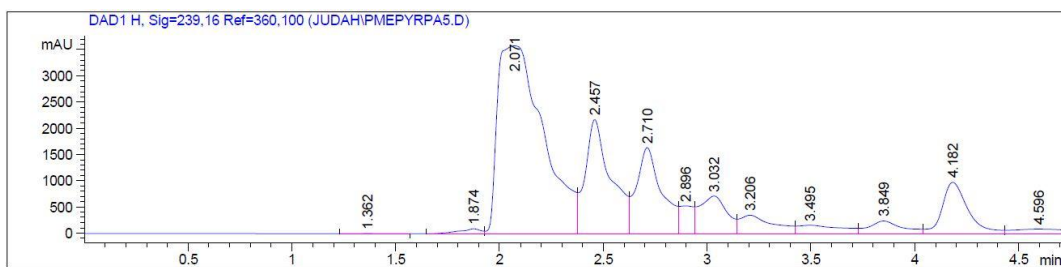
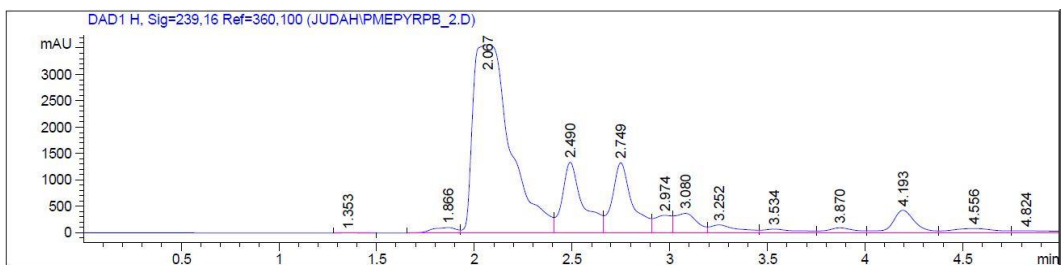


Figure A-4 Chromatogram of 2.40 mg/mL of P-3-methyl-2,5-pyridine-P in a feed mixture with 5.13 mg/mL of benzo[a]pyrene, undiluted



**Figure A-5** Chromatogram of P-3-methyl-2,5-pyridine-P 1<sup>st</sup> product mixture with 3.45 mg/mL of benzo[*a*]pyrene, undiluted



**Figure A-6** Chromatogram of P-3-methyl-2,5-pyridine-P 2<sup>nd</sup> product mixture with 1.40 mg/mL of benzo[*a*]pyrene, undiluted

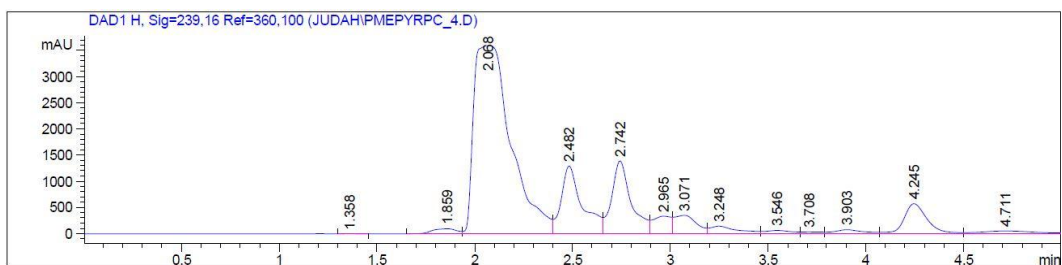


**Figure A-7** Chromatogram of P-3-methyl-2,5-pyridine-P 3<sup>rd</sup> product mixture with 2.23 mg/mL of benzo[*a*]pyrene, undiluted

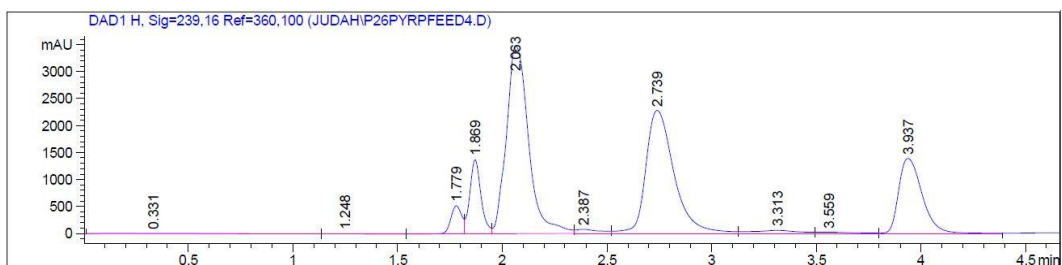


**Figure A-8** Chromatogram of 2.39 mg/mL of P-2,6-pyridine-P in a feed mixture with 4.60 mg/mL of benzo[*a*]pyrene, undiluted

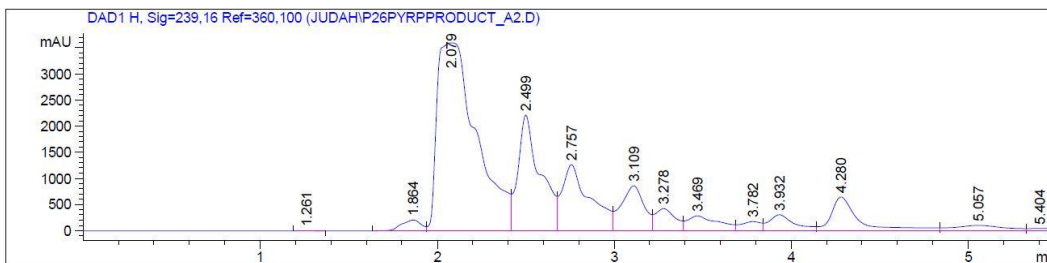


**Figure A-9** Chromatogram of P-2,6-pyridine-P 1<sup>st</sup> product mixture with 1.63 mg/mL of benzo[a]pyrene, undiluted

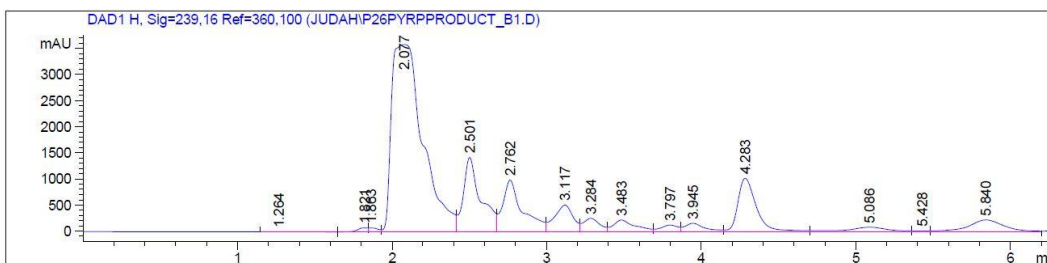


**Figure A-10** Chromatogram of P-2,6-pyridine-P 2<sup>nd</sup> product mixture with 4.31 mg/mL of benzo[a]pyrene, undiluted

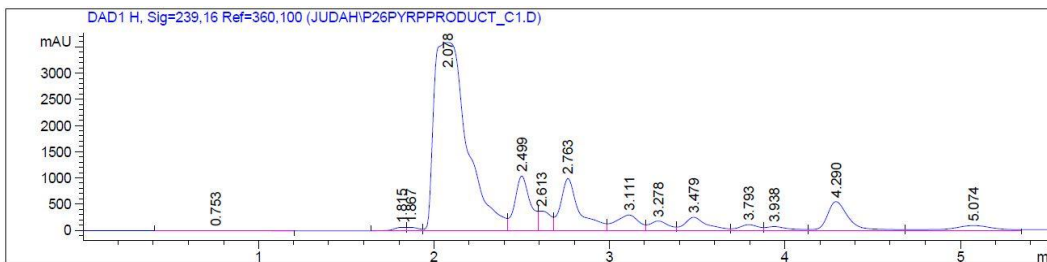


**Figure A-11** Chromatogram of P-2,6-pyridine-P 3<sup>rd</sup> product mixture with 2.66 mg/mL of benzo[a]pyrene, undiluted

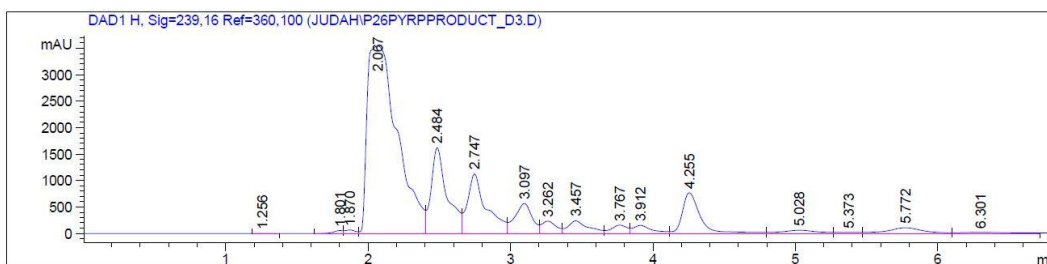


**Figure A-12** Chromatogram of P-2,6-pyridine-P 4<sup>th</sup> product mixture with 2.43 mg/mL of benzo[a]pyrene, undiluted

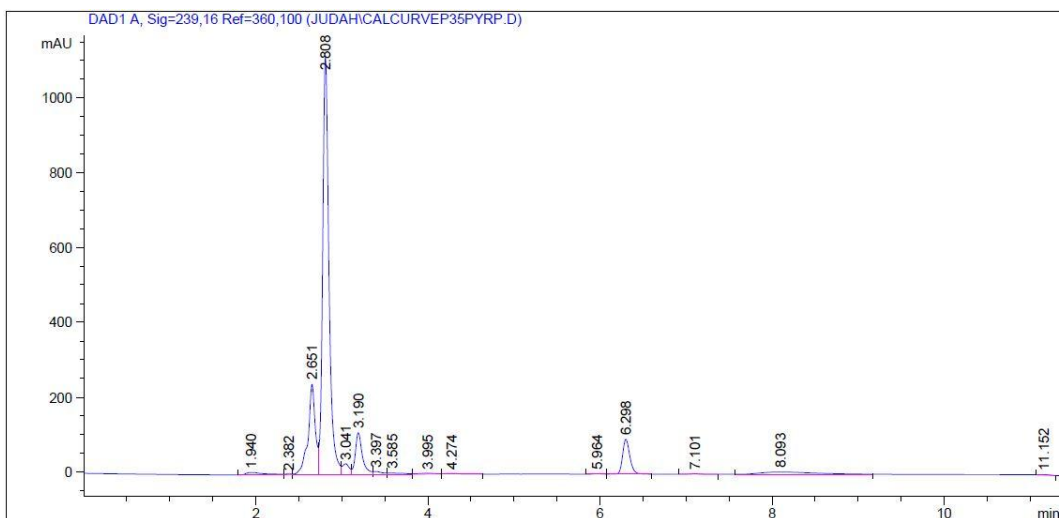


**Figure A-13** Chromatogram of 2.40 mg/mL of P-3,5-pyridine-P in a feed mixture with 1.10 mg/mL of benzo[a]pyrene, diluted 1:30 in methylene chloride

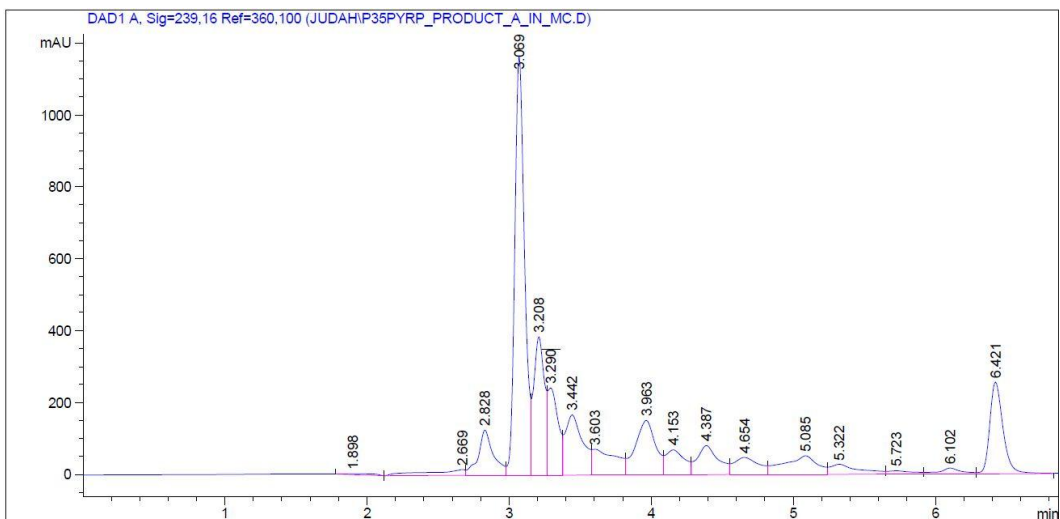


**Figure A-14** Chromatogram of P-3,5-pyridine-P 1<sup>st</sup> product mixture with 1.16 mg/mL of benzo[a]pyrene, diluted 1:30 in methylene chloride

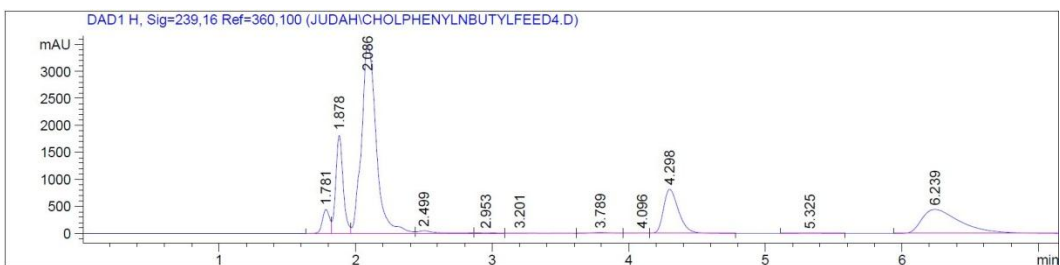


**Figure A-15** Chromatogram of 2.53 mg/mL of cholestane-phenyl-*n*-butyl in a feed mixture with 4.26 mg/mL of benzo[a]pyrene, undiluted

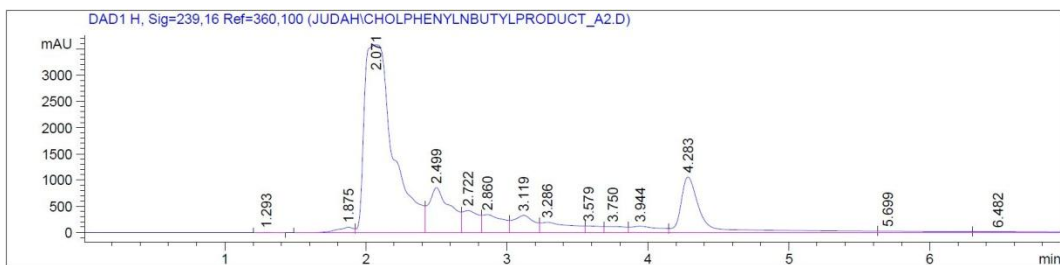


**Figure A-16** Chromatogram of cholestane-phenyl-*n*-butyl 1<sup>st</sup> product mixture with 1.80 mg/mL of benzo[*a*]pyrene, undiluted

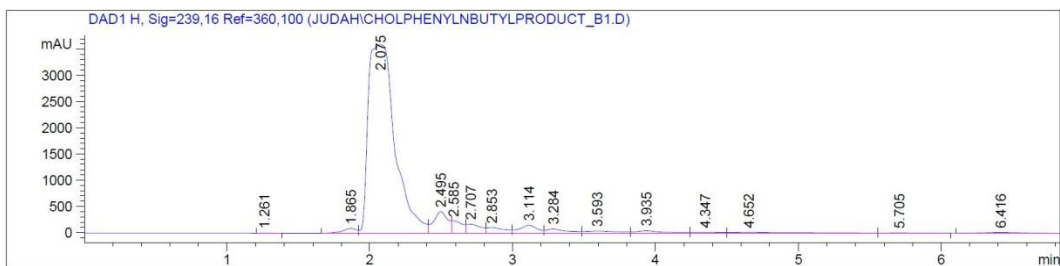


**Figure A-17** Chromatogram of cholestane-phenyl-*n*-butyl 2<sup>nd</sup> product mixture, undiluted

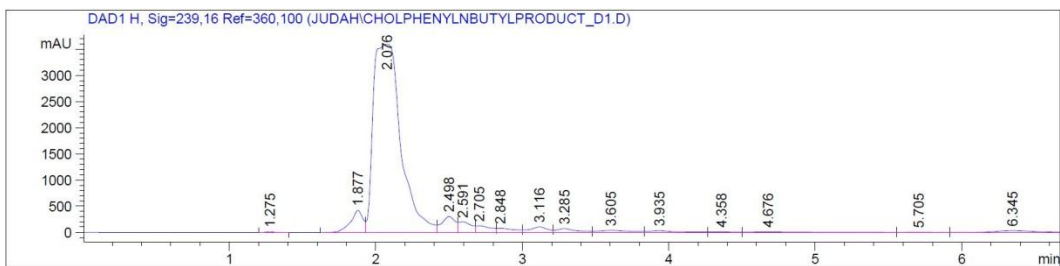


**Figure A-18** Chromatogram of cholestane-phenyl-*n*-butyl 3<sup>rd</sup> product mixture, undiluted

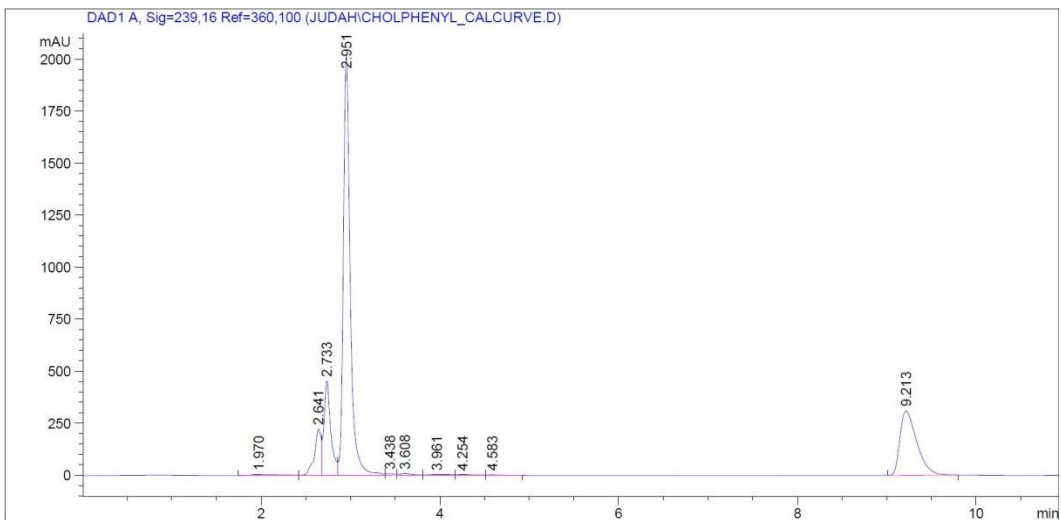


**Figure A-19** Chromatogram of 2.40 mg/mL of cholestane-phenyl in a feed mixture with 2.40 mg/mL of benzo[a]pyrene, diluted 1:30 in methylene chloride

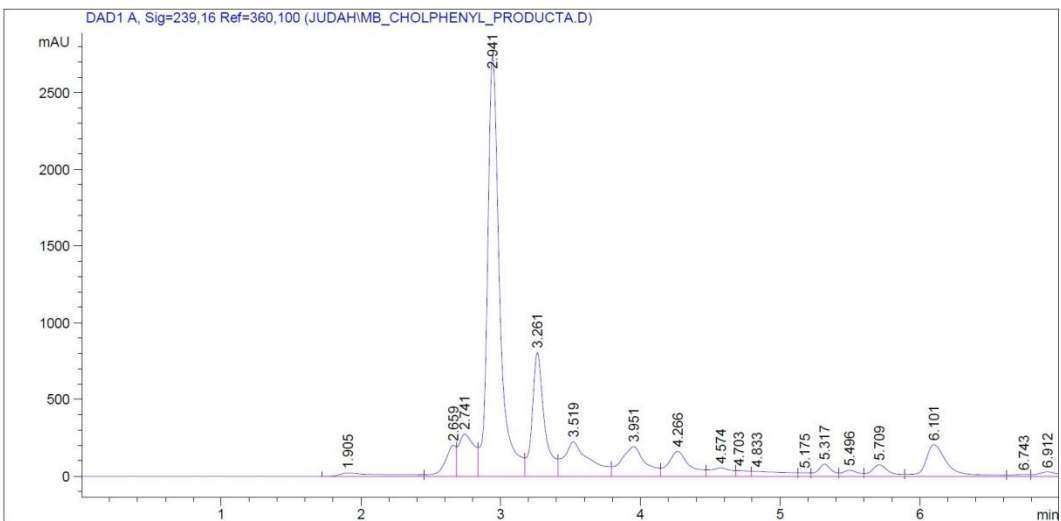


**Figure A-20** Chromatogram of cholestane-phenyl 1<sup>st</sup> reaction product with 0.80 mg/mL of benzo[a]pyrene (not shown), diluted 1:30 in methylene chloride

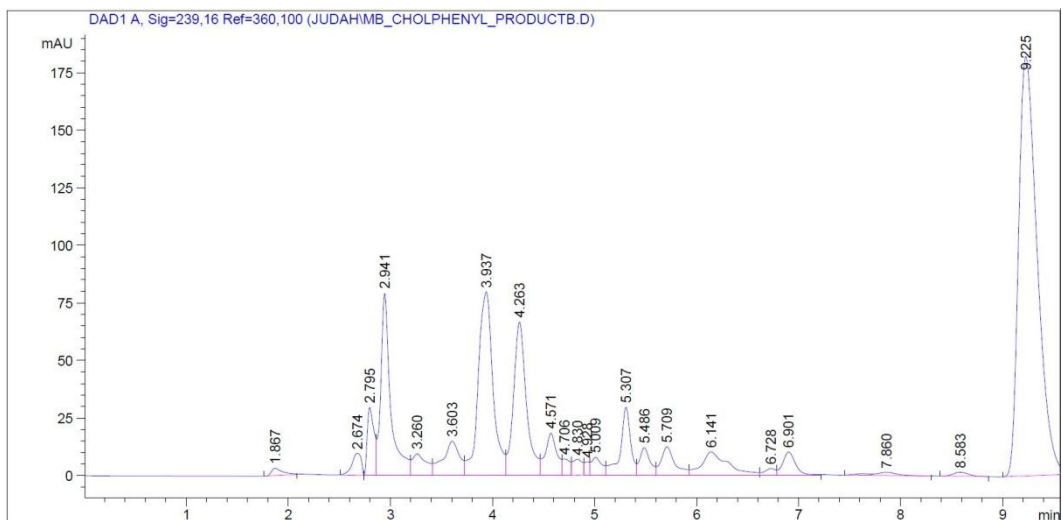


**Figure A-21** Chromatogram of cholestane-phenyl 2<sup>nd</sup> reaction product with 1.00 mg/mL of benzo[a]pyrene, diluted 1:30 in methylene chloride

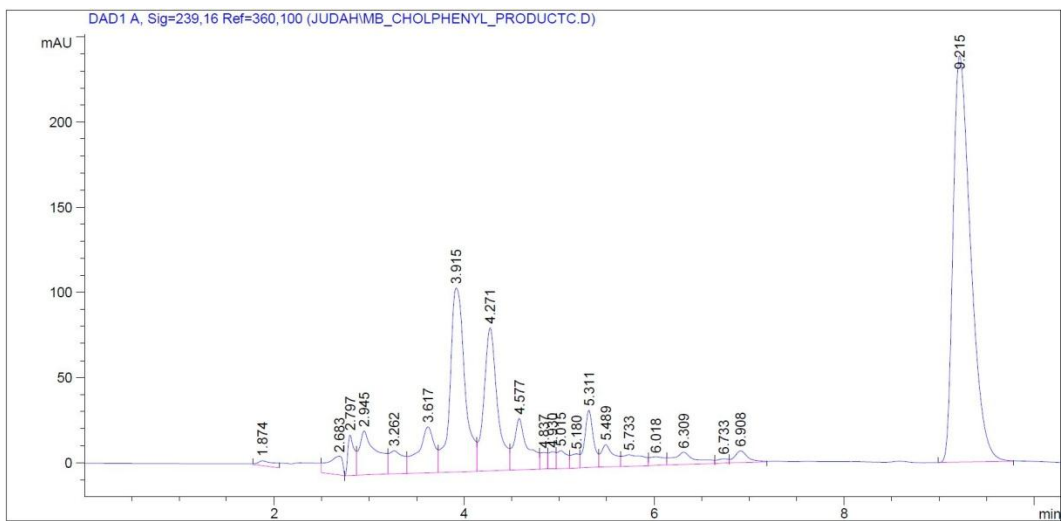


**Figure A-22** Chromatogram of cholestane-phenyl 3<sup>rd</sup> reaction product with 1.43 mg/mL of benzo[a]pyrene, diluted 1:30 in methylene chloride

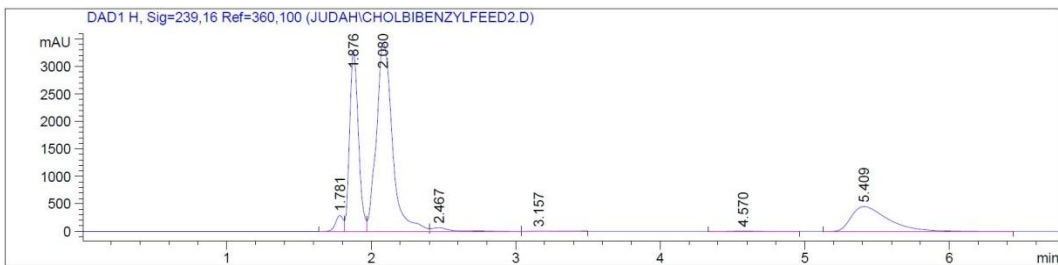


**Figure A-23** Chromatogram of 2.42 mg/mL of cholestane-bibenzyl in a feed mixture with 4.85 mg/mL of benzo[a]pyrene, undiluted

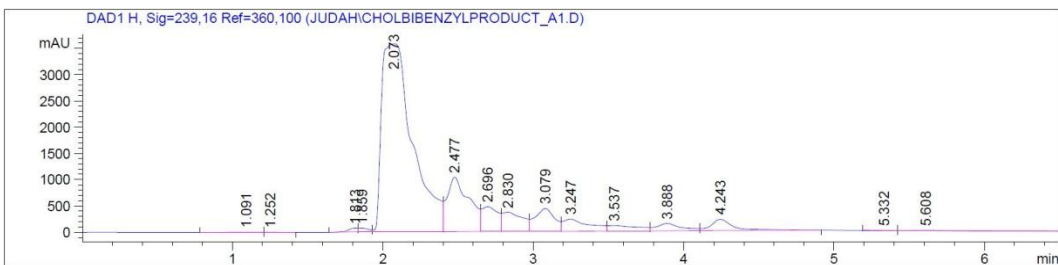


**Figure A-24** Chromatogram of cholestane-bibenzyl 1<sup>st</sup> reaction product with 0.58 mg/mL of benzo[a]pyrene, undiluted

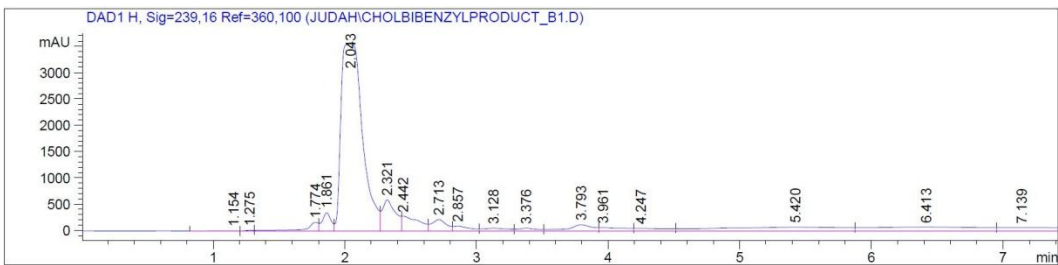


**Figure A-25** Chromatogram of cholestane-bibenzyl 2<sup>nd</sup> reaction product, undiluted

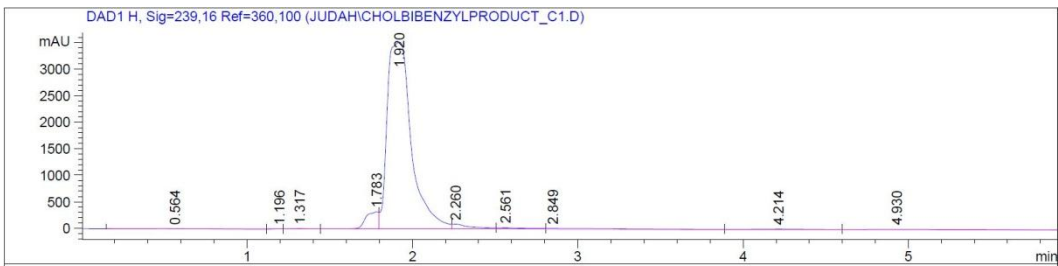


**Figure A-26** Chromatogram of cholestane-bibenzyl 3<sup>rd</sup> reaction product, undiluted

# APPENDIX B

---

## GC Calculations and Chromatograms

This appendix details the calculations performed on GC chromatograms to obtain the feed model compound concentration remaining in the reaction product mixtures. Included are the chromatograms and formulae needed to do so.

### **1 Single Point Internal Standard Method Calculations**

An unknown concentration of analyte can be evaluated by determining the relative response factor of a known quantity of the same analyte. The relative response factor can be calculated from the internal standard and analyte peak areas and concentrations from the following:

$$b = \frac{A_a c_{is}}{c_a A_{is}} \quad (\text{B-1})$$

where the  $a$  and  $is$  subscripts refer to the analyte and internal standard, respectively. Once the relative response factor is known, unknown analyte concentrations can be determined from a known peak area using the single point internal standard method as follows:

$$c_a = \frac{1}{b} \left( \frac{A_a c_{is}}{A_{is}} \right) \quad (\text{B-2})$$

Table B-1 shows the analyte peak areas ( $A_a$ ), internal standard concentrations ( $c_{is}$ ), internal standard peak areas ( $A_{is}$ ) and relative response factors for all the GC calculations used in this study. The relative response factors were determined by the signal response of calibration sample of a known quantity of analyte and internal standard, tetrachloro-*m*-xylene, injected into the GC instrument.

**Table B-1** List of data required for single point internal standard method calculations

<b>Experiment</b>	<b>Analyte peak area, <math>A_a</math> (arbitrary units)</b>	<b>Internal standard concentration, <math>c_{is}</math> (mg/mL)</b>	<b>Internal standard peak area, <math>A_{is}</math> (arbitrary units)</b>	<b>Relative response factor, <math>b</math></b>
<b>Catalytic Cracking</b>				
<i>P-3-methyl-2,5-pyridine-P</i>	9.90E+06	0.80	1.77E+08	2.31E+01
<i>P-3,5-pyridine-P</i>	5.60E+06	0.43	8.92E+07	2.31E+01
<i>P-2,6-pyridine-P</i>	5.40E+06	0.34	8.98E+07	2.31E+01
<i>Thermal cracking control</i>	8.60E+06	0.45	3.77E+08	2.31E+01
<b>Control Experiments</b>				
<i>phenanthrene – mild</i>	9.10E+07	0.79	3.31E+08	2.56E-02
<i>phenanthrene – normal</i>	5.10E+07	0.30	1.17E+08	2.56E-02
<i>quinoline – mild</i>	6.42E+07	0.27	2.13E+08	1.82E+01
<i>quinoline – normal</i>	<i>by inspection of chromatogram analyte almost completely converted</i>			
<i>w/o catalyst</i>	4.94E+08	0.70	1.70E+08	2.56E-02
<i>w/o hydrogen</i>	1.43E+08	1.06	1.15E+09	1.82E+01

## 2 GC Chromatograms

The following are the GC chromatograms used in measurement of cracked product concentrations from catalytic hydrogenation reactions and control experiment reaction product concentrations:

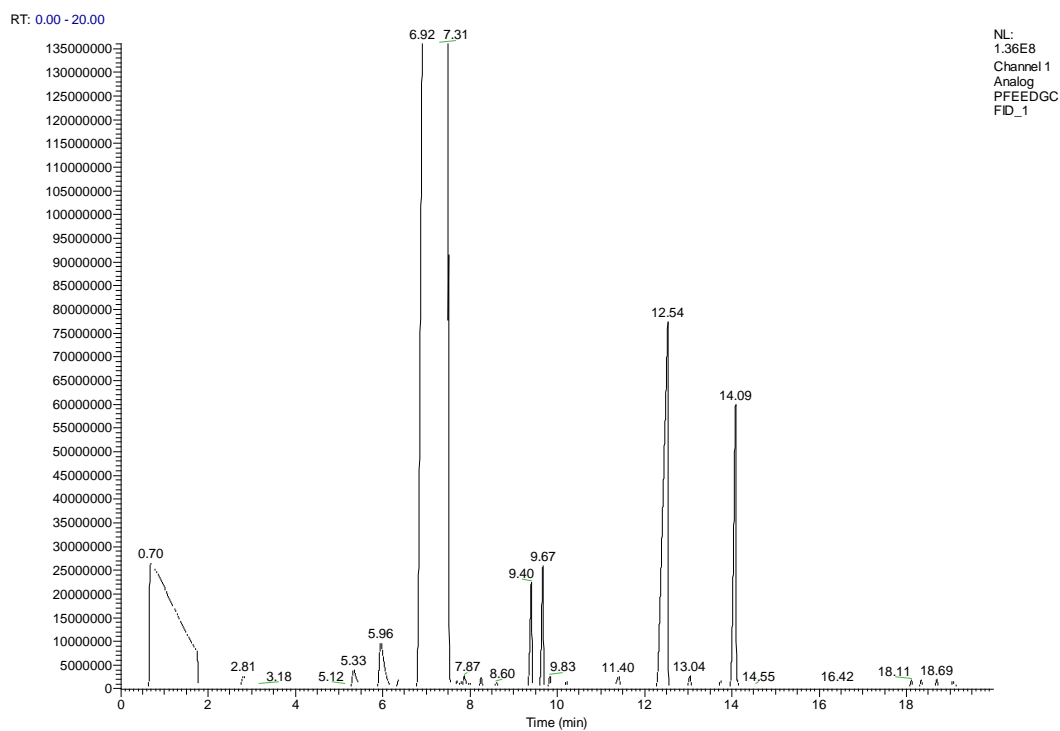


**Figure B-1** Chromatogram of 1 wt % phenanthrene feed (14.09 min) with 0.64 mg of 2,4,5,6-tetrachloro-*m*-xylene (12.54 min)

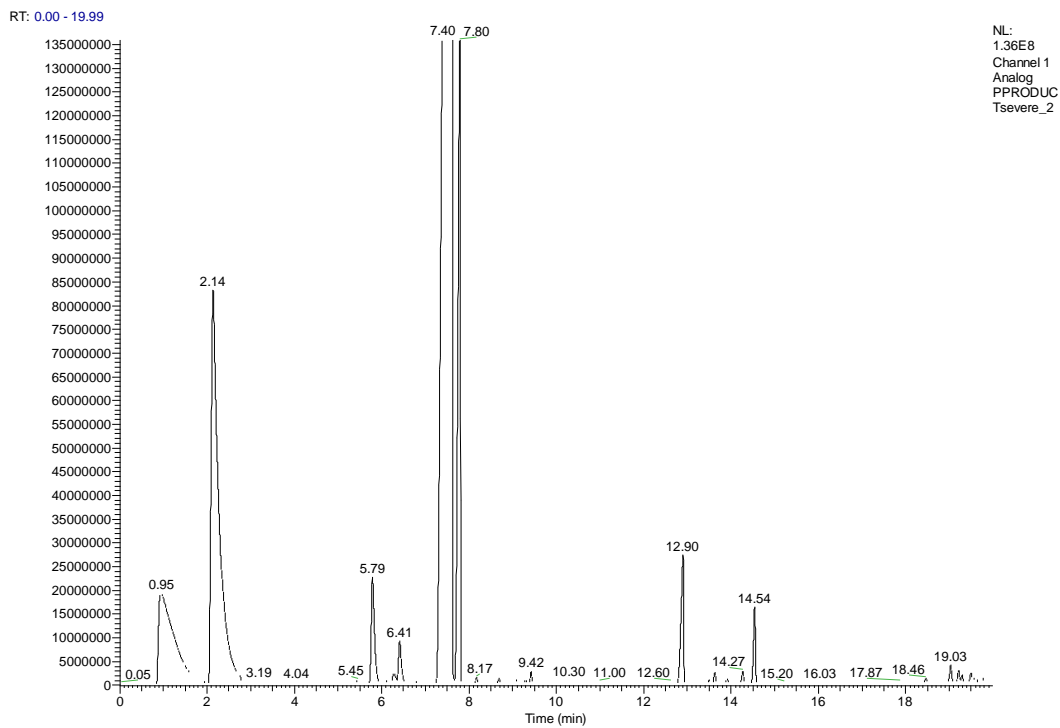


**Figure B-2** Chromatogram of 1 wt % phenanthrene reaction product at normal conditions with 0.30 mg of 2,4,5,6-tetrachloro-*m*-xylene

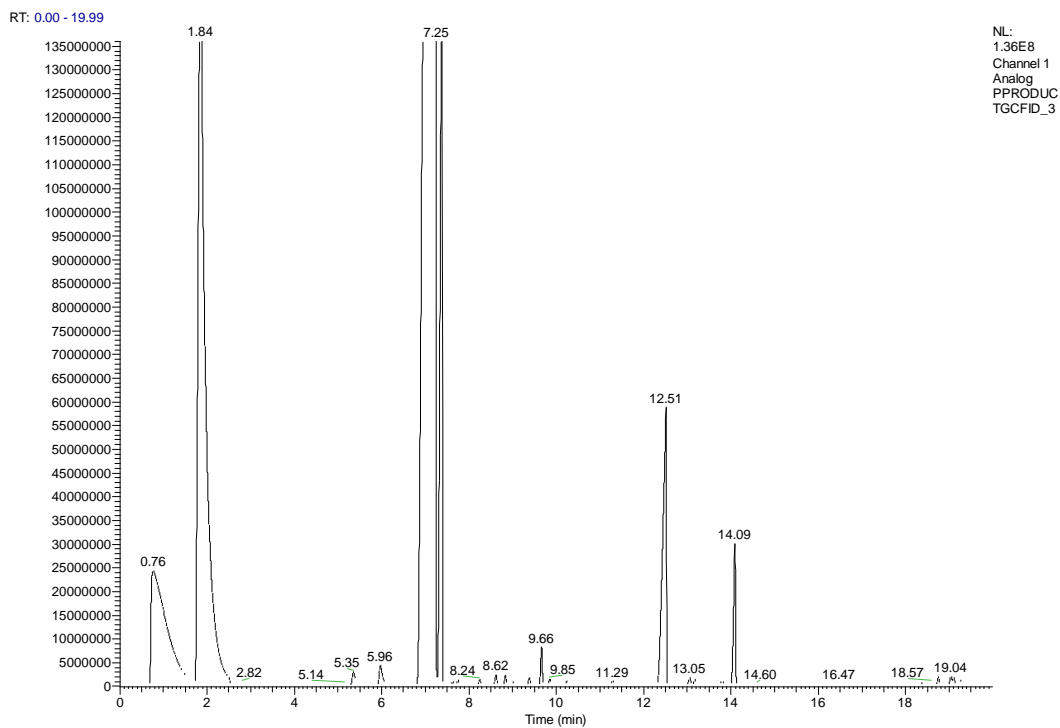


**Figure B-3** Chromatogram of 1 wt % phenanthrene reaction product at mild conditions with 0.79 mg of 2,4,5,6-tetrachloro-*m*-xylene

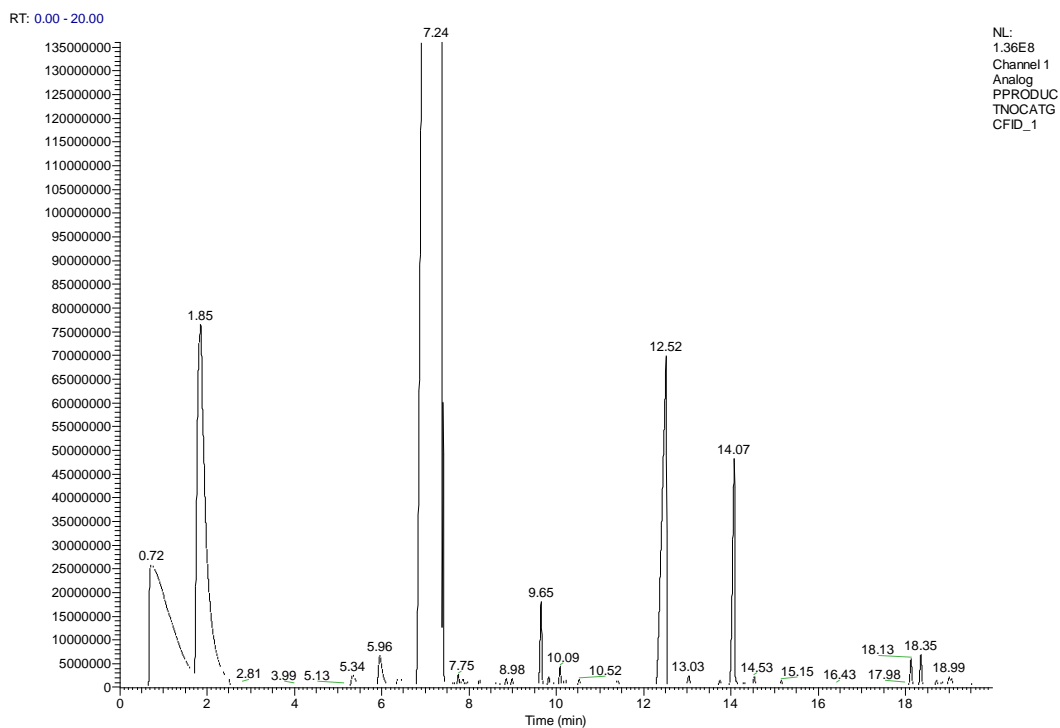


**Figure B-4** Chromatogram of w/o catalyst experiment reaction product at mild conditions with 0.70 mg of 2,4,5,6-tetrachloro-*m*-xylene, 1 wt % phenanthrene feed

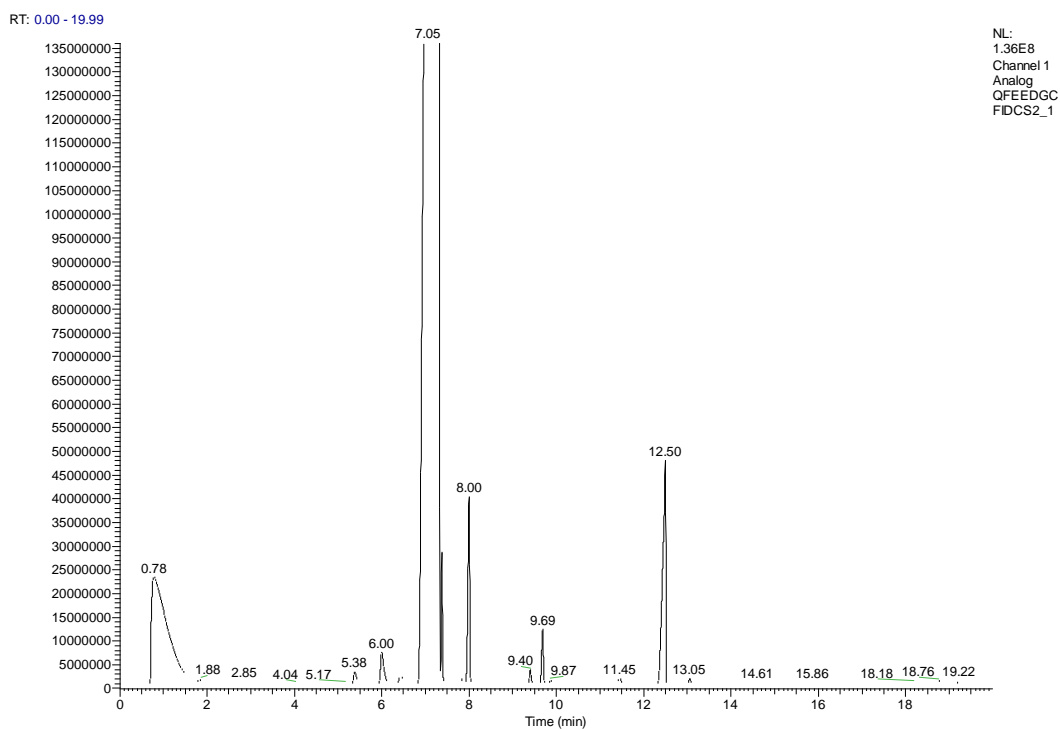


**Figure B-5** Chromatogram of 1 wt % quinoline feed (8.00 min) with 0.37 mg of 2,4,5,6-tetrachloro-*m*-xylene (12.50 min)

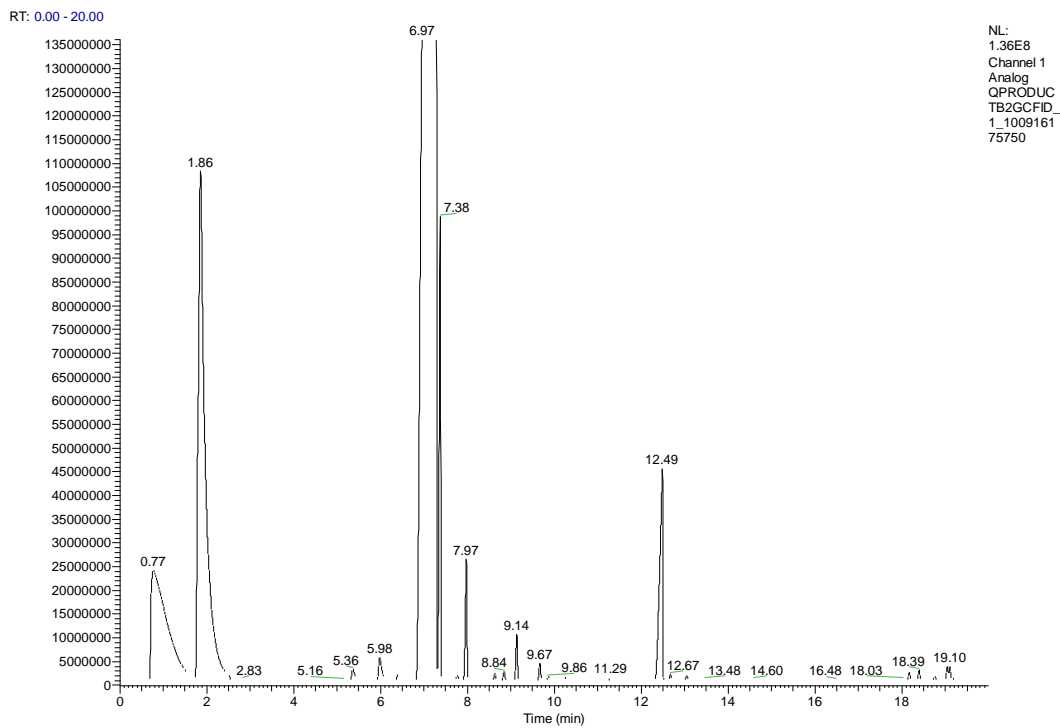


**Figure B-6** Chromatogram of 1 wt % quinoline reaction product at mild conditions with 0.27 mg of 2,4,5,6-tetrachloro-*m*-xylene

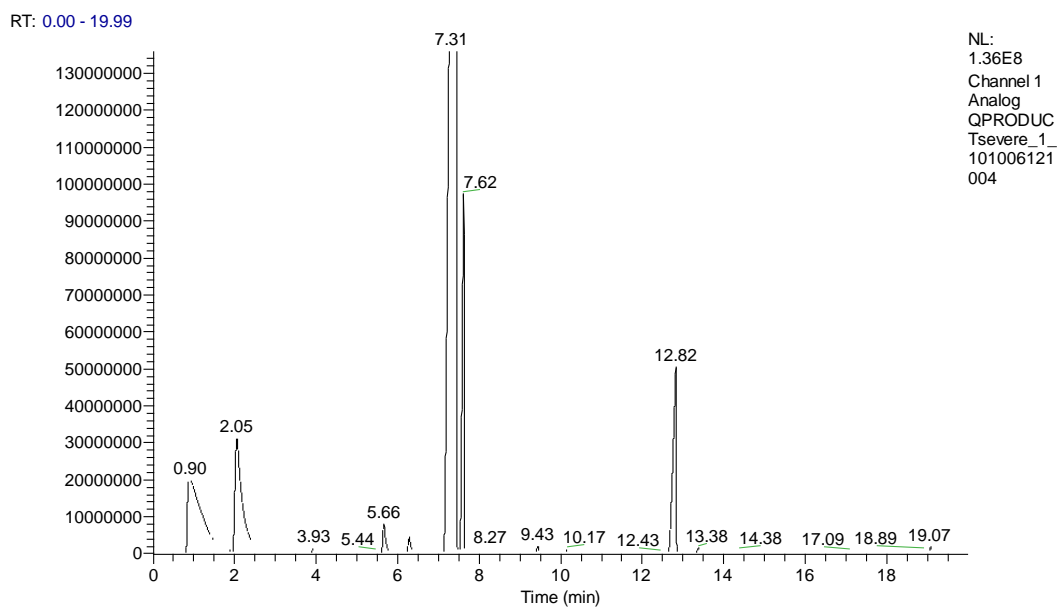


**Figure B-7** Chromatogram of 1 wt % quinoline reaction product at normal conditions with 0.87 mg of 2,4,5,6-tetrachloro-*m*-xylene

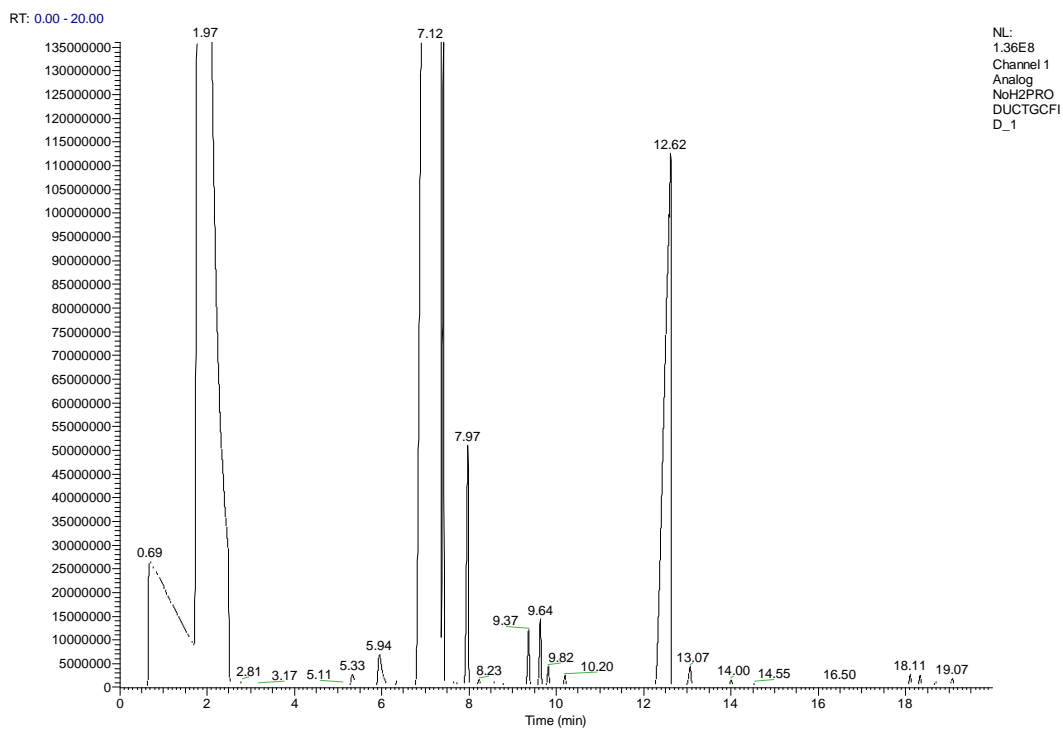


**Figure B-8** Chromatogram of w/o hydrogen experiment reaction product at mild conditions with 1.06 mg of 2,4,5,6-tetrachloro-*m*-xylene, 1 wt % quinoline feed

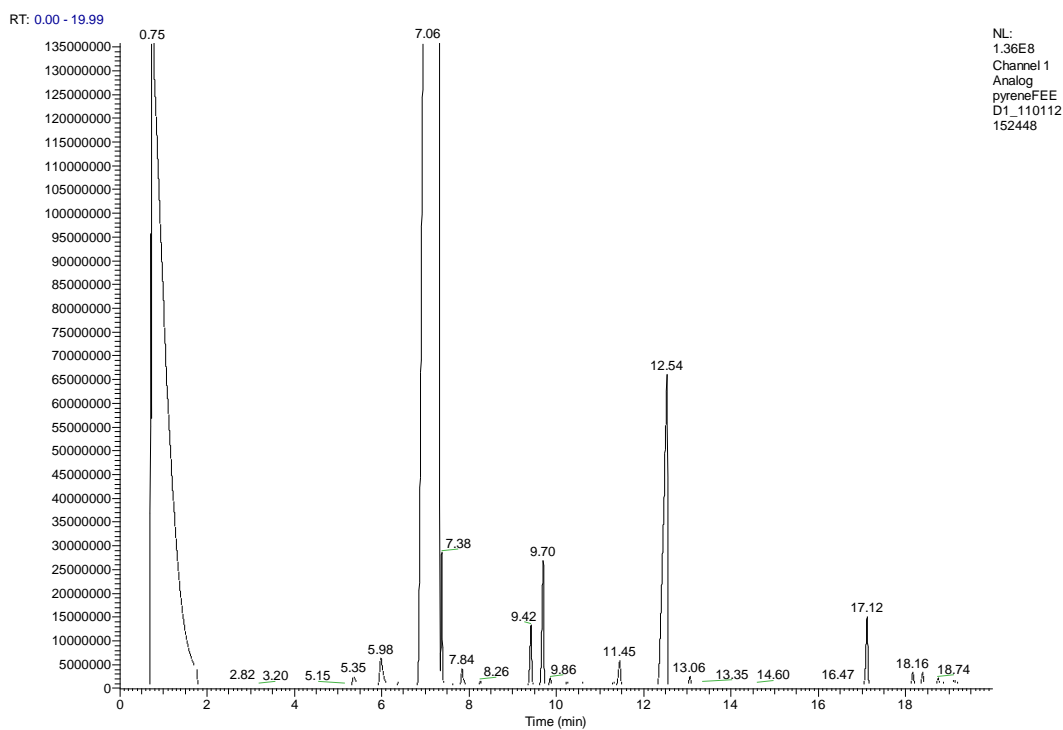


**Figure B-9** Chromatogram of 2.58 mg/mL of pyrene (17.12 min) feed with 0.74 mg of 2,4,5,6-tetrachloro-*m*-xylene (12.54 min)

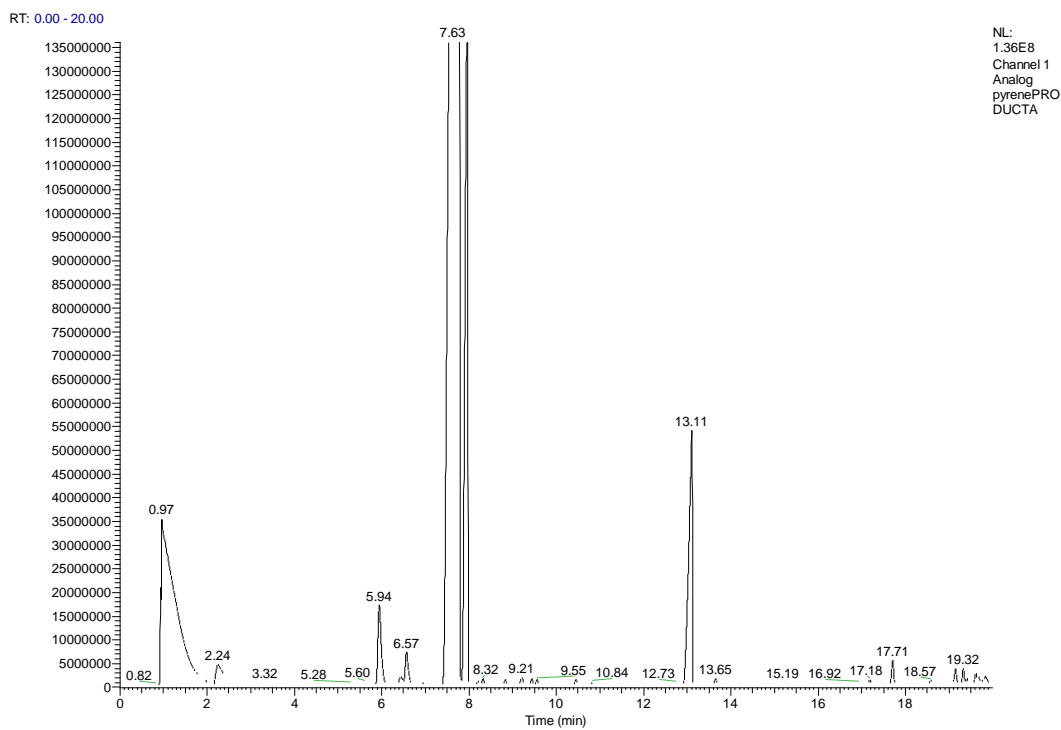


**Figure B-10** Chromatogram of 1<sup>st</sup> pyrene reaction product with 0.89 mg of 2,4,5,6-tetrachloro-*m*-xylene

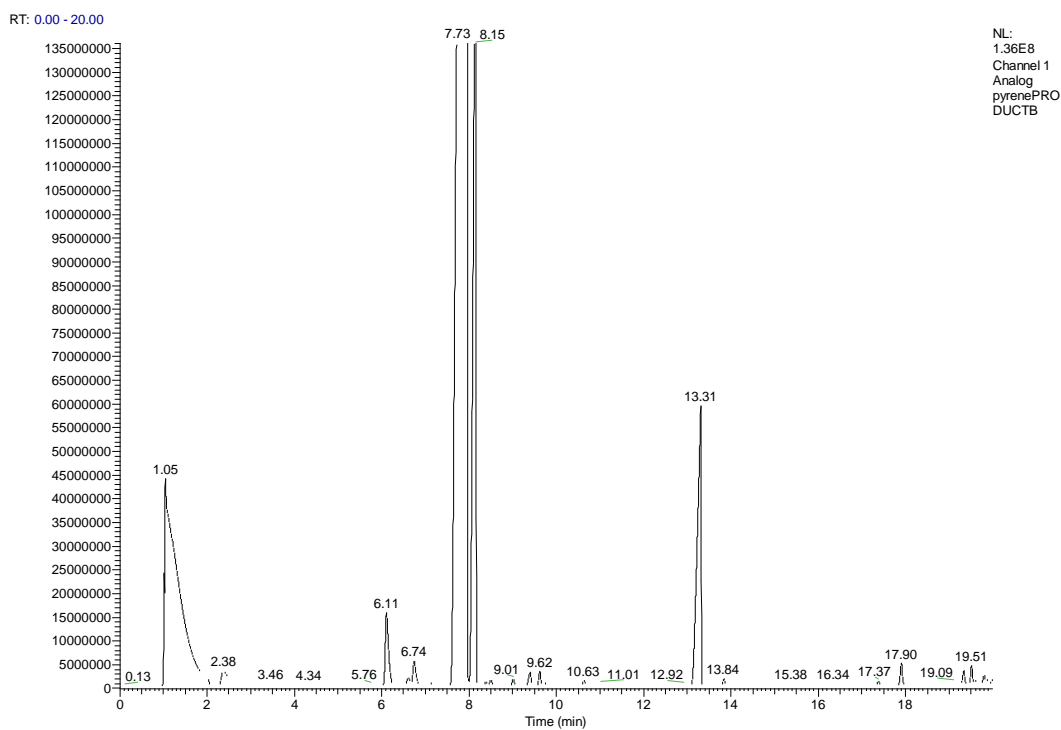


**Figure B-11** Chromatogram of 2<sup>nd</sup> pyrene reaction product with 1.22 mg of 2,4,5,6-tetrachloro-*m*-xylene

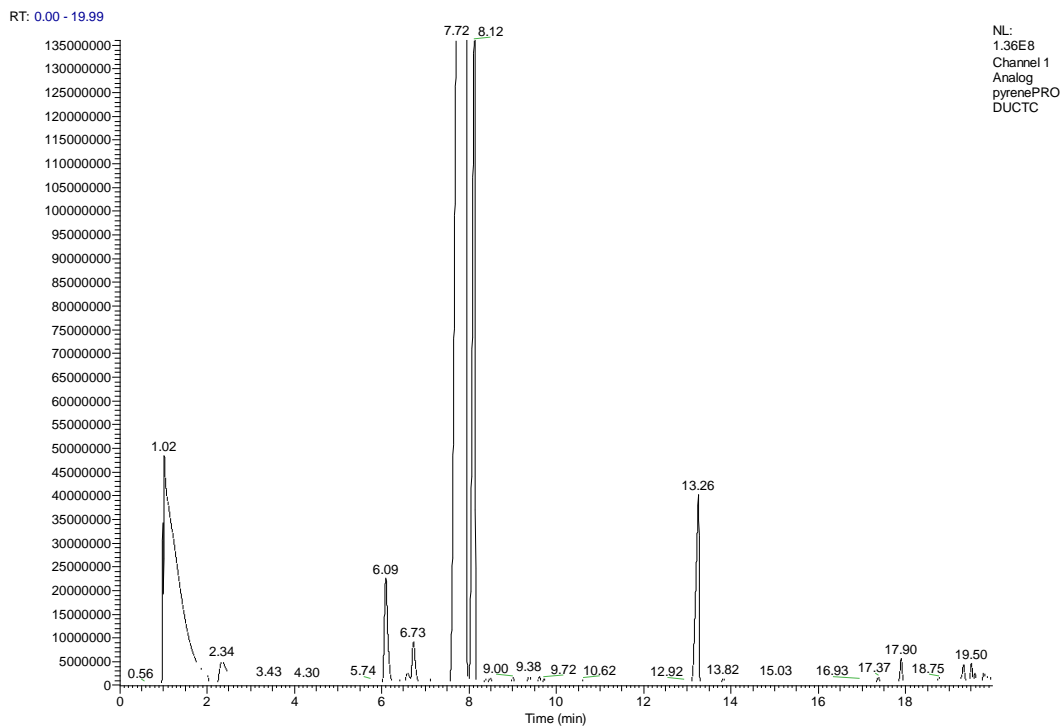


**Figure B-12** Chromatogram of 3<sup>rd</sup> pyrene reaction product with 0.58 mg of 2,4,5,6-tetrachloro-*m*-xylene

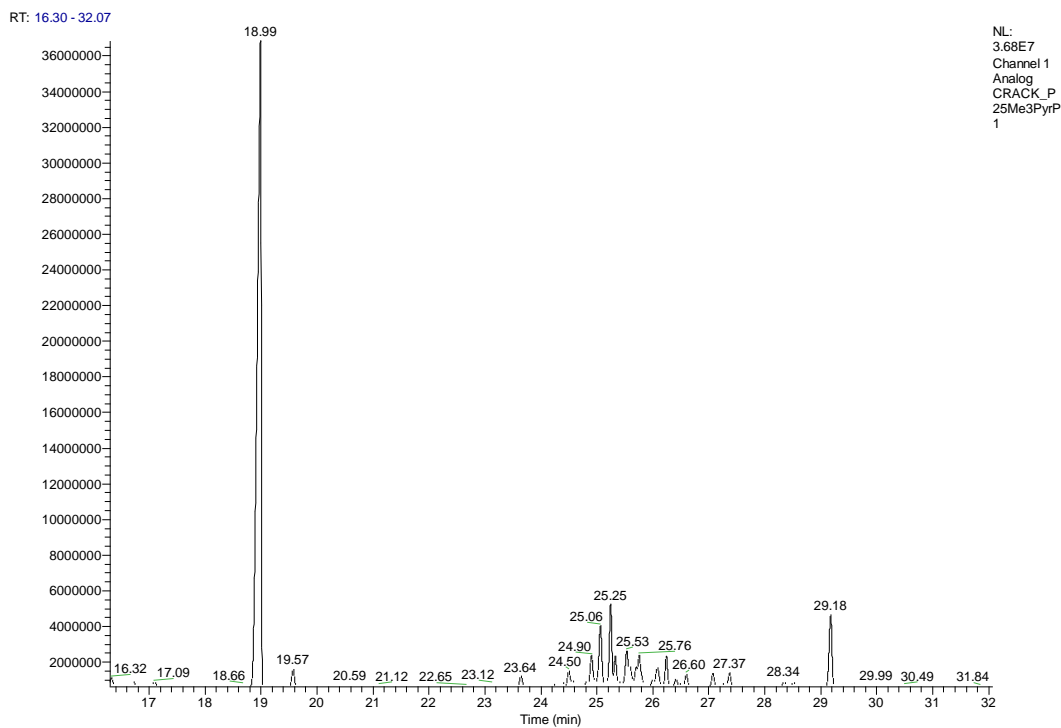


**Figure B-13** Chromatogram of P-3-methyl-2,5-pyridine-P reaction product with 0.80 mg of 2,4,5,6-tetrachloro-*m*-xylene

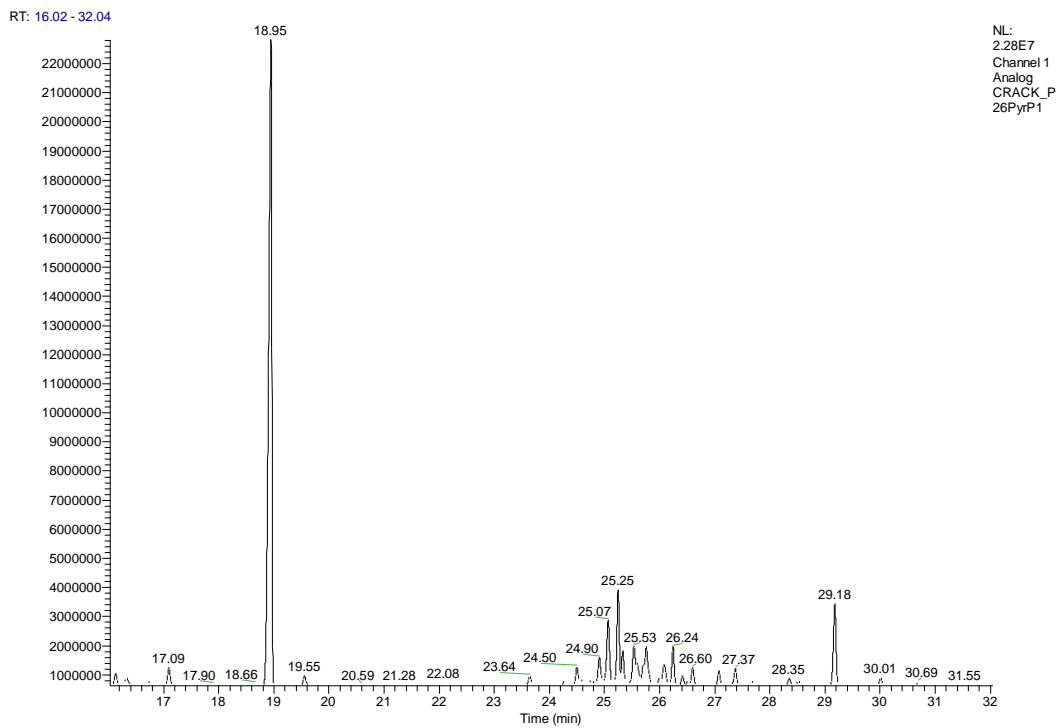


**Figure B-14** Chromatogram of P-2,6-pyridine-P reaction product with 0.34 mg of 2,4,5,6-tetrachloro-*m*-xylene

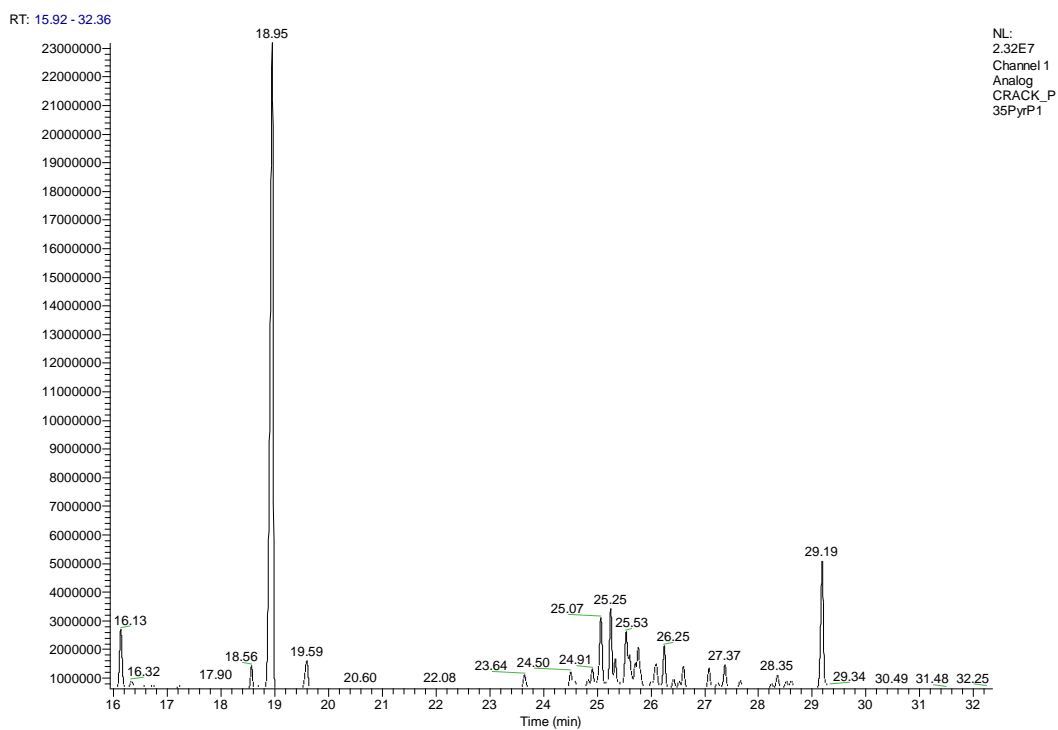


**Figure B-15** Chromatogram of P-3,5-pyridine-P reaction product with 0.43 mg of 2,4,5,6-tetrachloro-*m*-xylene

# APPENDIX C

---

## MALDI – MS Analysis Method and Spectra

This appendix details the calculations performed on MALDI –MS spectra to obtain a HDN to hydrogenation selectivity ratio and product identification and characterization. Included are spectra and a description of the analysis method needed to do so.

### **1. MALDI – MS Analysis Method**

Analysis of the MALDI – MS spectra with tandem MS/MS of the feed and product samples to produce modified integrated peak area spectra consisted of 4 steps which will be detailed here.

### Step 1 Possible Product Peak Identification

MALDI – MS spectra of the feed and product samples are compared on an amount detected basis to identify possible reaction product peaks. This can be achieved by overlaying the feed and product spectra on the same plot. Figure C-1 gives an example of this, plotting the feed and product spectra of P-3,5-pyridine-P. For example, in this case it is evident that the peak at  $m/z = 538.20$  is a potential product peak, likely a hydrogenation product.

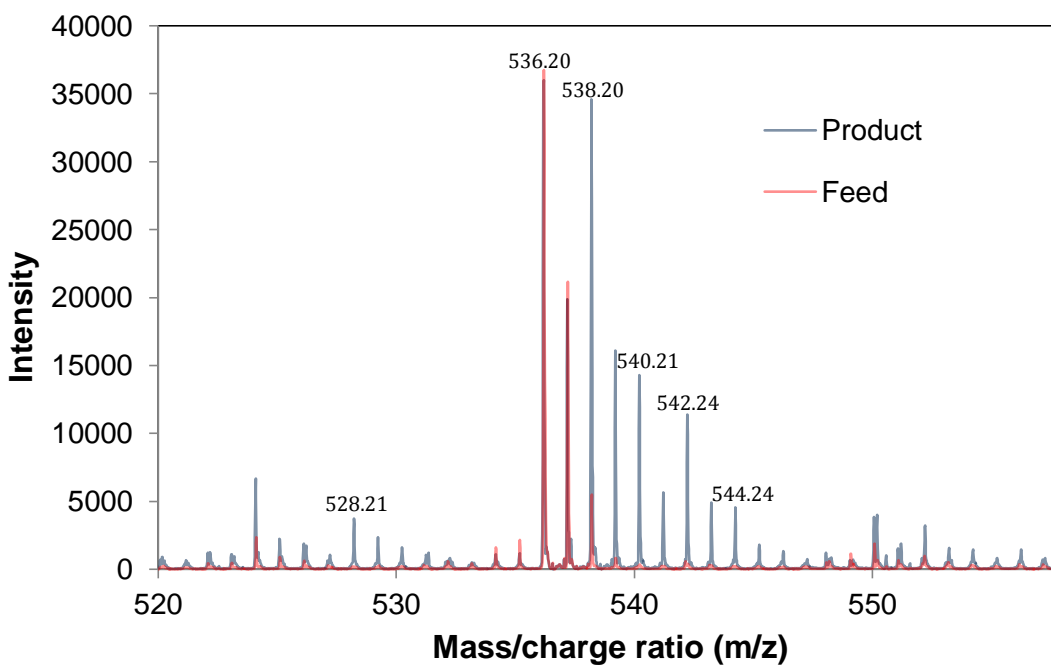


**Figure C-1** MALDI – MS feed spectrum overlaid the product spectra of P-3,5-pyridine-P

### Step 2 Product Peak Verification by MALDI – MS/MS

The MALDI – MS/MS technique is used to confirm suspected product peaks from Step 1 by identifying common fragment ions between the MALDI – MS/MS spectra of the parent compound and the selected product peak. Categorization into

hydrogenation and hydrodenitrogenation reaction products can then occur after consultation and interpretation of MALDI – MS/MS spectra of the product peaks. As an example, Figure C-2 and Figure C-3 show MALDI – MS/MS spectra of the P-2,6-pyridine-P parent compound and  $m/z = 540.22$  precursor ion, respectively. It is evident that these spectra share common fragment ions,  $m/z = 215.04$  for example. This confirms product peak at  $m/z = 540.22$  ion is a product of P-2,6-pyridine-P.

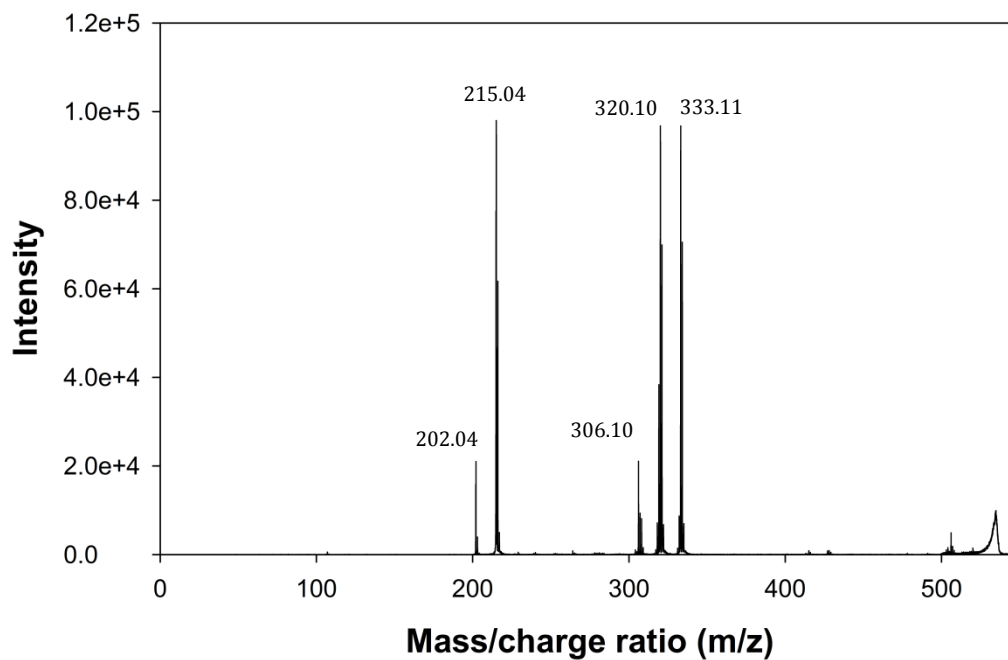


**Figure C-2** MALDI – MS/MS spectrum of parent compound P-2,6-pyridine-P

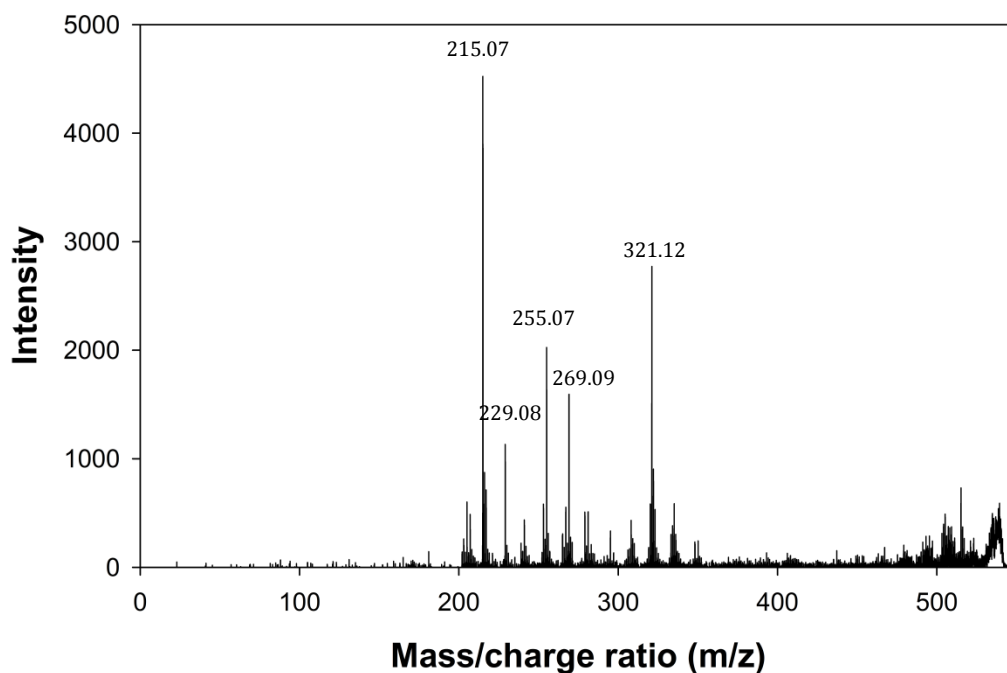


**Figure C-3** MALDI – MS/MS spectrum of precursor ion  $m/z = 540.22$ , P-2,6-pyridine-P hydrogenation product

### Step 3 Isotope Identification

Isotopes were identified using the Scientific Instrument Service Isotope Distribution Calculator at <http://www.sisweb.com/mstools/isotope.htm>. For example, the isotope distribution for the  $m/z = 538.20$  hydrogenation product peak gives an isotope distribution of 45.2%, 10%, 1.3% and 0.1% for each isotopes at  $m/z = 539, 540, 541$  and  $542$ , respectively. Referring back to Figure C-1, it is evident that the peaks at  $m/z = 539$  is wholly an isotope of a hydrogenation product at  $538.20$  and some of the intensity of peak  $m/z = 540.22$  is likely an isotope of that product as well.

#### **Step 4 Product Peak Area Integration and Summation**

Once isotopes had been identified in Step 3, product peaks and isotope peaks were integrated by Polymath 6.10 software from an exported Excel file. The integrated peak areas that corresponded to a single product were then summed in the following manner:

- the peak area of a product peak at a particular mass/charge ratio that was present in both feed and product MALDI – MS spectra that was considered to not be an isotope of the parent compound was modified by subtracting the peak area in the feed spectrum from the product spectrum;
- identified isotopic peaks had their peak area added to the peak area of the corresponding product peak. Where a peak at a specific  $m/z$  was considered to be both an isotope of one product and that of another, the peak area was divided between the products by attributing a peak area predicted from the isotopic distribution to the isotopic peak area with the remainder apportioned to the other product. For example, if  $m/z = 538.20$  hydrogenation product peak gives an isotope distribution of 45.2%, 10%, 1.3% at  $m/z = 539, 540, 541$  and  $542$ , respectively; the peak area at  $m/z = 542$  would be split by subtracting  $0.013 \times$  (peak area) from the peak area and attributing it to the isotopic peak area of the  $m/z = 538.20$  hydrogenation product, and the remainder would be considered representative of the  $542$   $m/z$  product peak area;
- Then all peak areas attributed to a product were added together, including isotopic peaks.

Table C-2 and Table C-3 list the integrated peak areas of identified products of both families of model compounds.

**Table C-2** List of integrated peak areas for identified reaction products for the pyrene/pyridine family

<b>Experiment</b>	<b>Identified Product Peaks and Integrated Peak Area</b>								
	<i>Parent</i>		<i>HDN</i>			<i>Hydrogenation</i>			
P-3-methyl-2,5-pyridine-P	550.21	543.28				552.26	554.27	556.28	558.30
Peak area	1528	469				1885	1601	2010	1271
P-3,5- pyridine-P	536.21	529.23				538.20	540.21	542.21	544.22
Peak area	3855	699				2608	1009	950	378
P-2,6- pyridine-P	536.19	524.19	526.22	528.24	530.25	538.19	540.22	542.23	
Peak area	642	364	1439	1600	310	444	403	420	

**Table C-3** List of integrated peak areas for identified reaction products for the cholestane family

<b>Experiment</b>	<b>Identified Product Peaks and Integrated Peak Area</b>							
	<i>Parent</i>	<i>DeHYD</i>		<i>Hydrogenation</i>				
cholestane-phenyl	598.44			600.42	602.44	604.45	606.49	608.49
Peak area	6355			16002	2977	718	3743	1908
cholestane-phenyl-n-butyl	654.46	650.42	652.42	656.42	658.47	660.47	662.50	664.51
Peak area	4551	514	474	3508	502	199	599	210
cholestane-bibenzyl	702.44			704.41	706.42	708.45	710.45	712.46
Peak area	4012			5417	221	324	786	136

## 2 MALDI – MS Spectra

The following are the MALDI – MS feed and product spectra used for calculations and interpretation in this study:

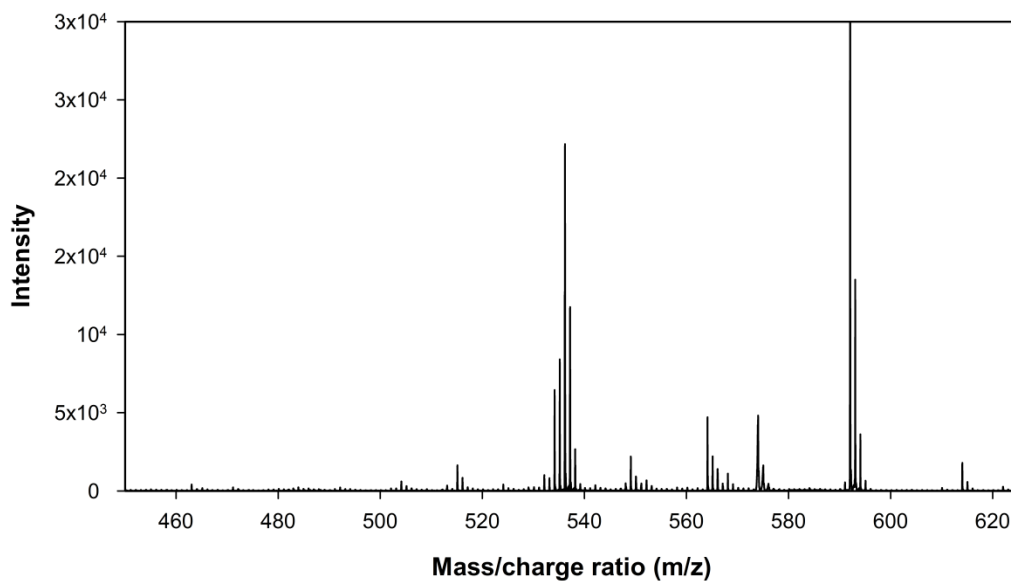


Figure C-4 MALDI – MS spectrum of P-2,6-pyridine-P feed

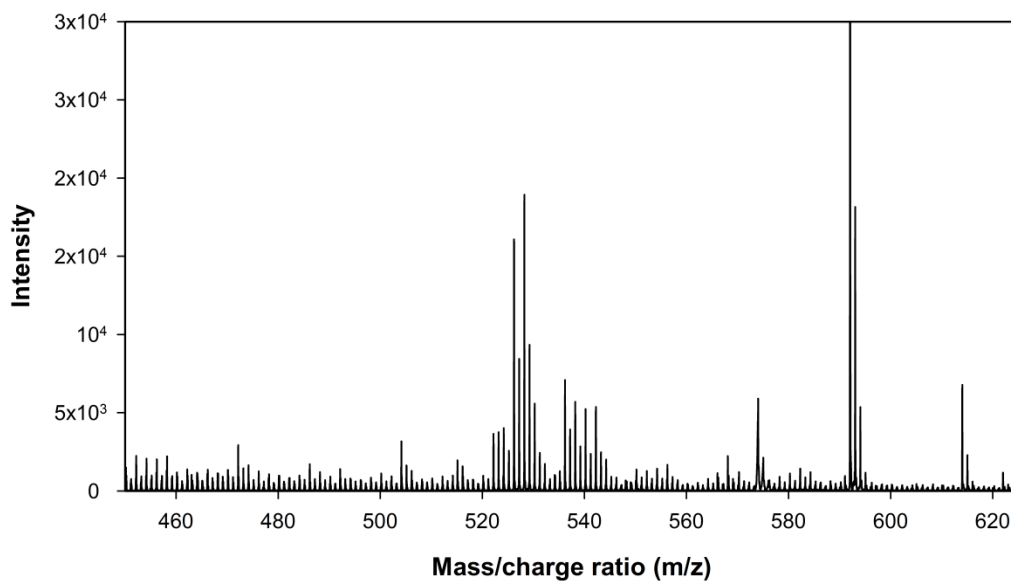
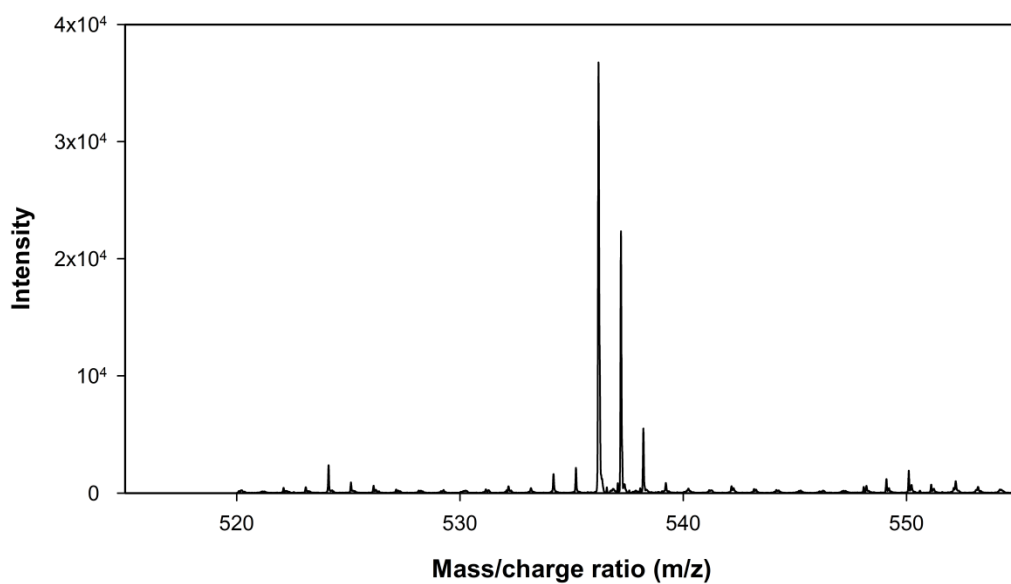
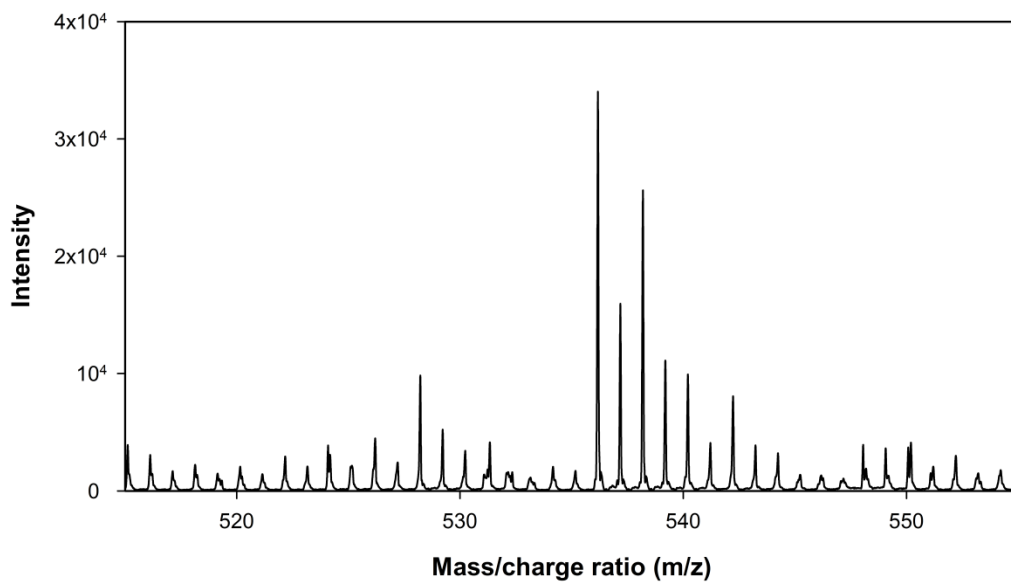


Figure C-5 MALDI – MS spectrum of P-2,6-pyridine-P reaction product



**Figure C-6** MALDI – MS spectrum of P-3,5-pyridine-P feed



**Figure C-7** MALDI – MS spectrum of P-3,5-pyridine-P reaction product

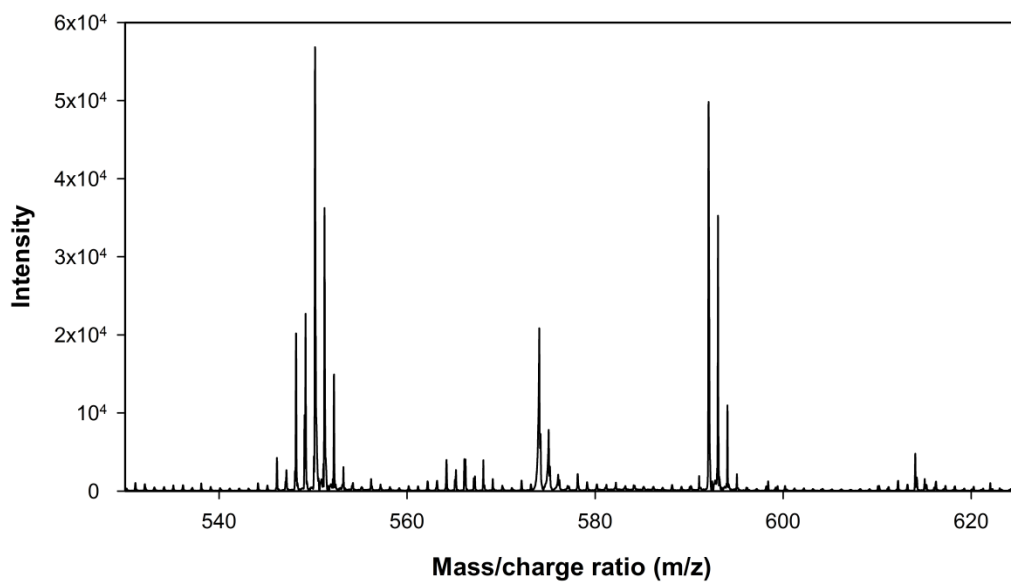


**Figure C-8** MALDI – MS spectrum of P-3-mehtyl-2,5-pyridine-P feed

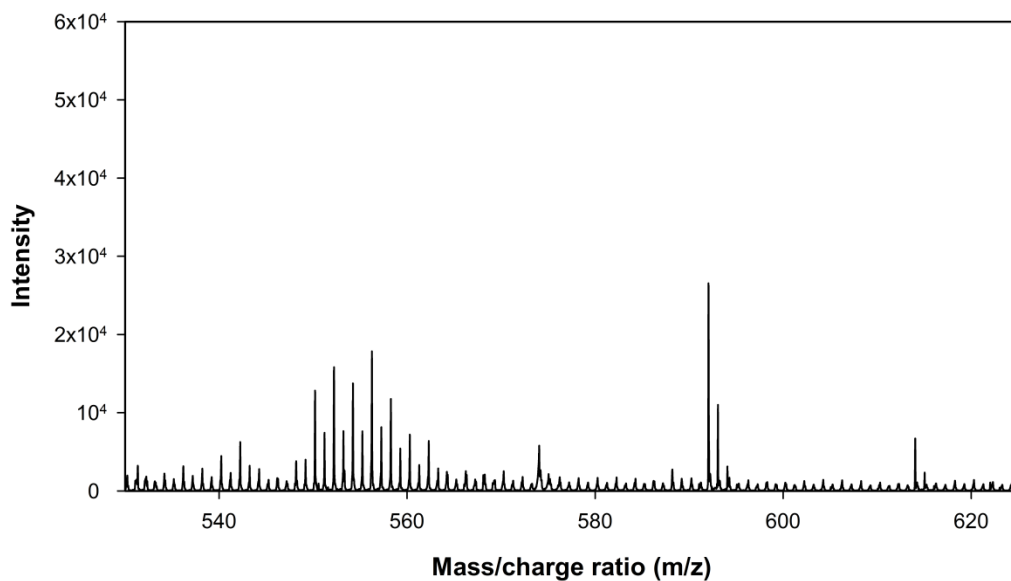


**Figure C-9** MALDI – MS spectrum of P-3-mehtyl-2,5-pyridine-P reaction product

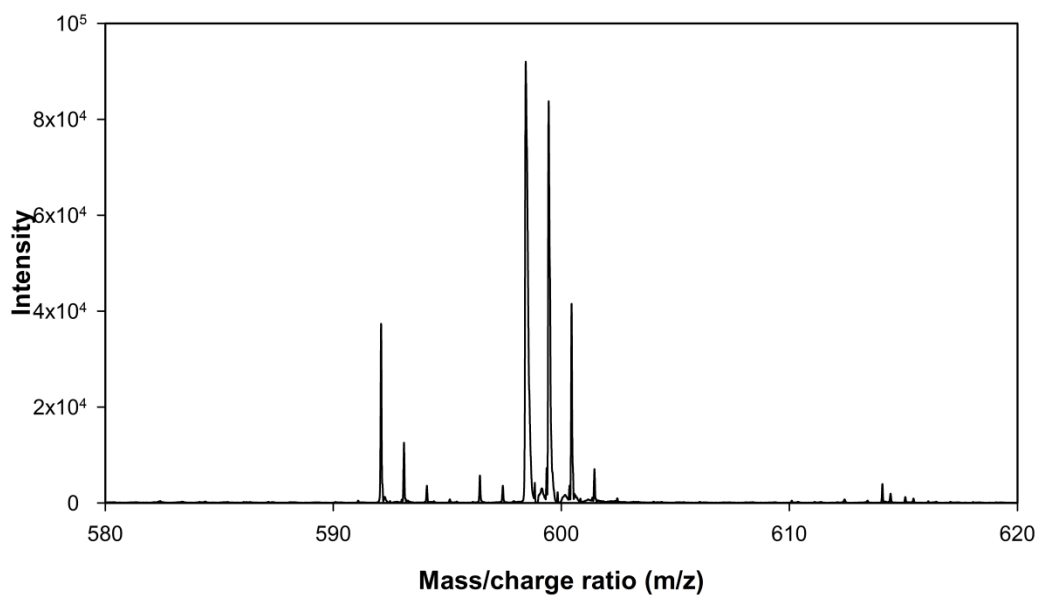


**Figure C-10** MALDI – MS spectrum of cholestane-phenyl feed

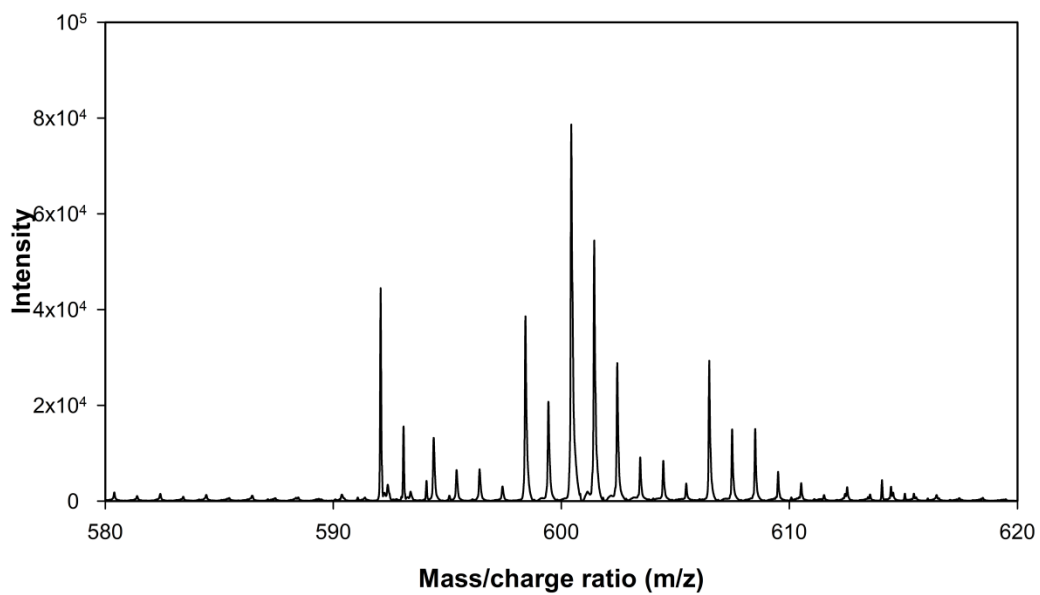


**Figure C-11** MALDI – MS spectrum of cholestane-phenyl reaction product

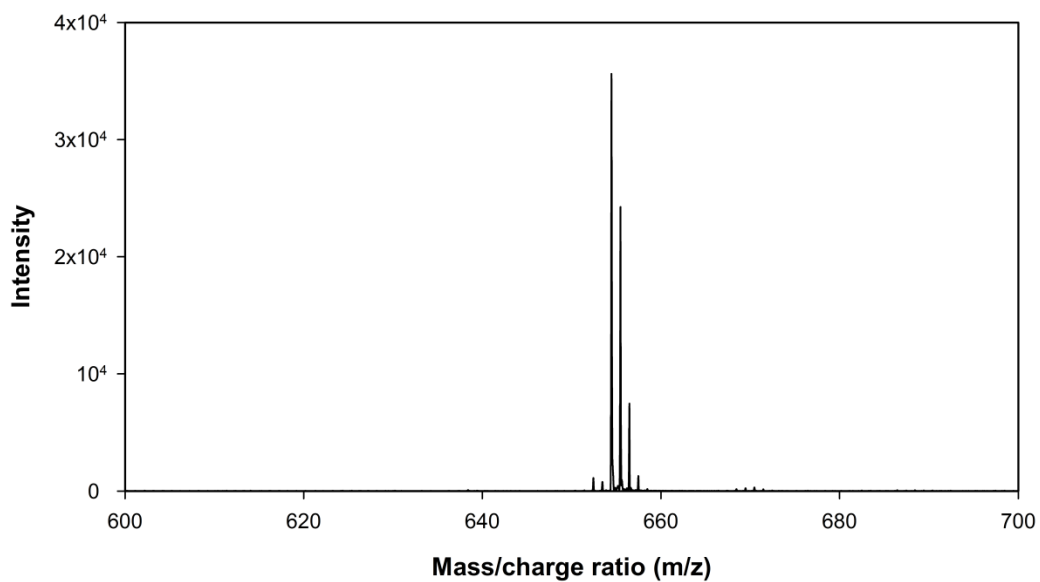


Figure C-12 MALDI – MS spectrum of cholestane-phenyl-*n*-butyl feed

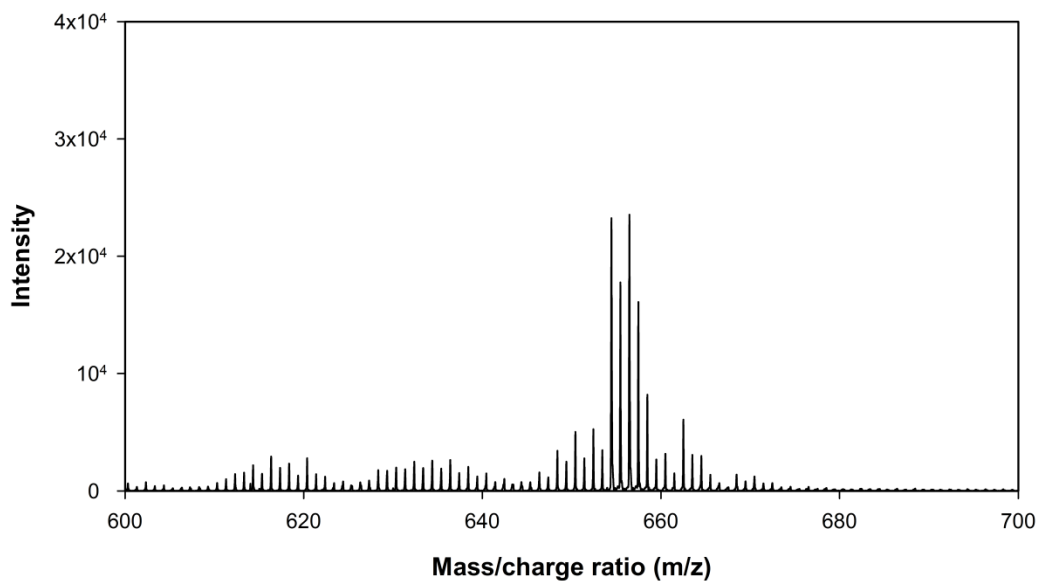
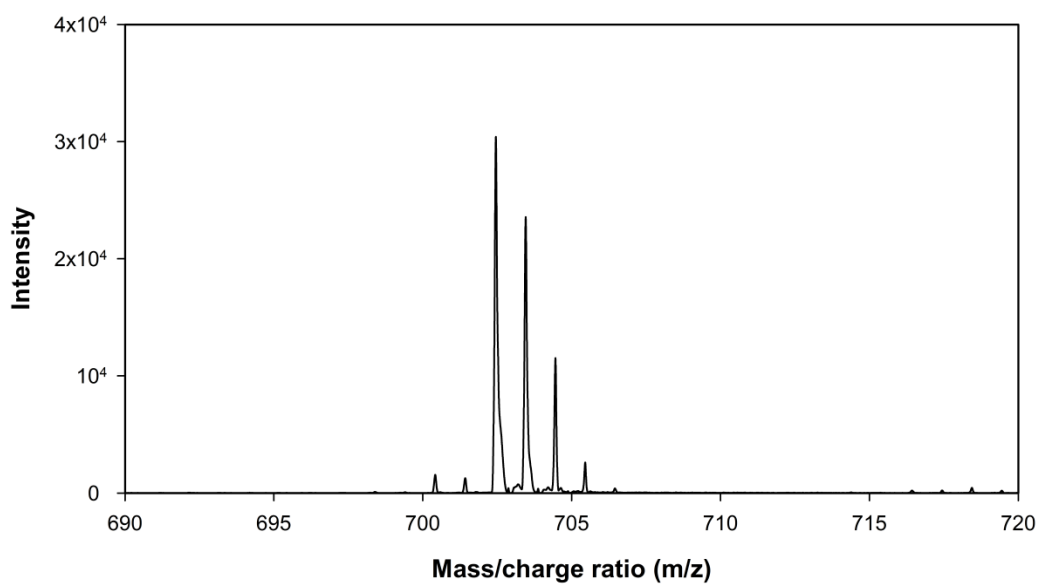
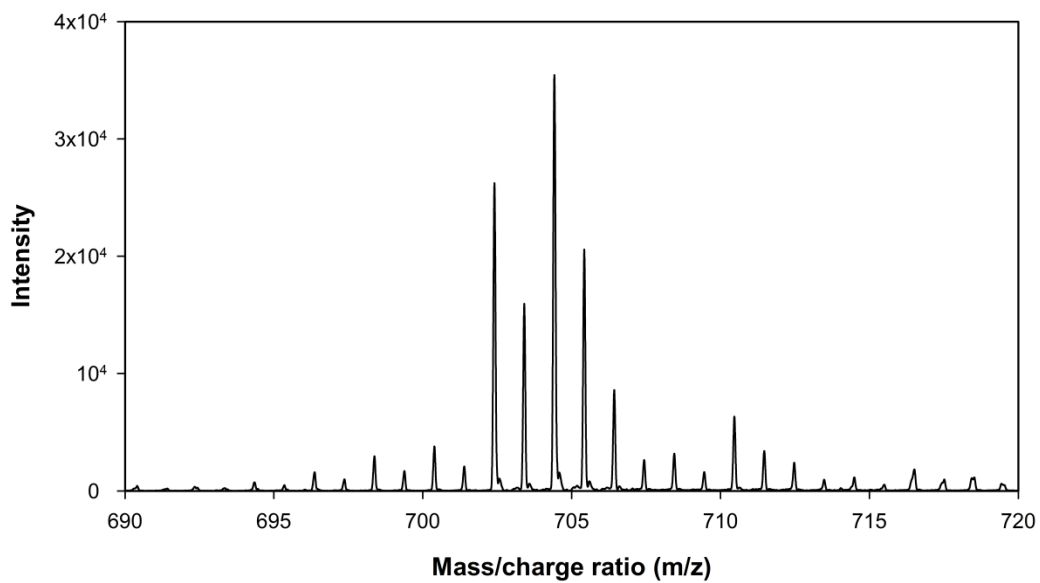


Figure C-13 MALDI – MS spectrum of cholestane-phenyl-*n*-butyl reaction product



**Figure C-14** MALDI – MS spectrum of cholestane-bibenzyl feed



**Figure C-15** MALDI – MS spectrum of cholestane-bibenzyl reaction product